INFORMATION TO USERS

This manuscript has been reproduced from the microfilm master. UMI films the text directly from the original or copy submitted. Thus, some thesis and dissertation copies are in typewriter face, while others may be from any type of computer printer.

The quality of this reproduction is dependent upon the quality of the copy submitted. Broken or indistinct print, colored or poor quality illustrations and photographs, print bleedthrough, substandard margins, and improper alignment can adversely affect reproduction.

In the unlikely event that the author did not send UMI a complete manuscript and there are missing pages, these will be noted. Also, if unauthorized copyright material had to be removed, a note will indicate the deletion.

Oversize materials (e.g., maps, drawings, charts) are reproduced by sectioning the original, beginning at the upper left-hand corner and continuing from left to right in equal sections with small overlaps. Each original is also photographed in one exposure and is included in reduced form at the back of the book.

Photographs included in the original manuscript have been reproduced xerographically in this copy. Higher quality 6" x 9" black and white photographic prints are available for any photographs or illustrations appearing in this copy for an additional charge. Contact UMI directly to order.

UMI

A Bell & Howell Information Company
300 North Zeeb Road, Ann Arbor MI 48106-1346 USA
313/761-4700 800/521-0600

UNIVERSITY OF OKLAHOMA

GRADUATE COLLEGE

MOLECULAR BEAM EPITAXY AND CHARACTERIZATION OF $InSb/Al_xIn_{1-x}Sb$ HETEROSTRUCTURES

A DISSERTATION

SUBMITTED TO THE GRADUATE FACULTY

in partial fulfillment of the requirements for the

degree of

DOCTOR OF PHILOSOPHY

By

KORY J. GOLDAMMER

Norman, Oklahoma

1998

MOLECULAR BEAM EPITAXY AND CHARACTERIZATION OF $InSb/Al_xIn_{1-x}Sb$ HETEROSTRUCTURES

A DISSERTATION APPROVED FOR THE
DEPARTMENT OF PHYSICS AND ASTRONOMY

BY

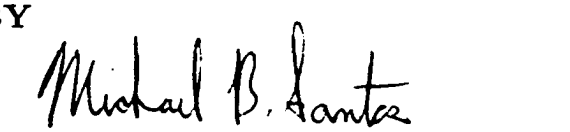

Michael Santos (Chair)

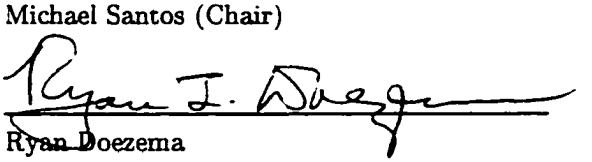

Ryan Doezema

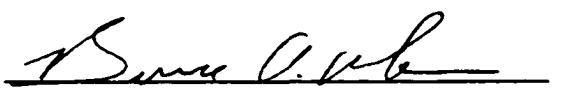

Bruce Mason

Patrick McCann

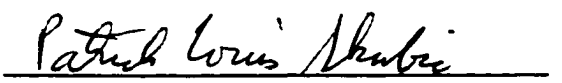

Patrick Skubic

Acknowledgments

There are many people to whom I owe a debt of gratitude. First and foremost, I would like to thank my parents, Donna and Gary Goldammer, for their love and support throughout my 28 years. They instilled in me the value of education, the desire to achieve, and the faith required to successfully accomplish this work. I would also like to thank my brother Kyle and his wife, Jenny, for their sense of humor and knack for never allowing my head to become too swollen. Finally, I would like to thank my extended family, in particular Grandma June, for their love and encouragement and for keeping me focused on what is really important in life.

I would like to acknowledge and thank the professors of the Solid State/Condensed Matter group (in alphabetical order): Doctors Doezema, Furneaux, Johnson, Mason, Mullen, and Murphy, and Dr. McCann (Electrical Engineering), for their help ranging from course-work and qualifiers to instructions for changing pump oil. I would also like to acknowledge post-docs Seokjae Chung and Ning Dai and fellow graduate students Weiluan Ma and Giti Khodaparast for their considerable assistance in all areas of the project. In addition, I am extremely grateful for the teaching provided by Dr. W.K. "Amy" Liu. She not only taught me virtually everything I know about crystal growth, but also how to manage a lab. Thanks also to my committee members, listed elsewhere, for their patience throughout this process.

I extend heartfelt thanks to my advisor, Dr. Michael Santos. He took me into the fold when I was something less than a bright and shining star and provided me with the resources and support to succeed. Thanks, Mike, for the Science, the teaching, the generosity, the patience, the trips, the many laughs, and above all, for being my friend.

Finally, I would like to thank Nicole Cunningham for her amazing ever-present support and encouragement. She never allowed me to get too distraught after a bad day, and always kept me in check after a good day. She was my partner and inspiration over the last three-plus years, and consistently did all the things that make me realize that I am a very lucky guy.

Contents

List of Tables

List of Figures

ABSTRACT

Two-dimensional electron systems were realized in InSb quantum wells with $Al_{0.09}In_{0.91}Sb$ barrier layers δ-doped with Si. Measured electron mobilities in multiple quantum well structures grown on GaAs(001) substrates were as high as 41,000cm^2/Vs at room temperature, which is the highest reported value for a semiconductor quantum well, and 380,000cm^2/Vs at 6.5K. Simple models can be used to explain the observed dependencies of the electron density on the quantum well to dopant distance and on the number of quantum wells. Dopant compensation was studied for Si δ-doped InSb samples grown on GaAs(001) substrates. Hall effect measurements indicate a sharp decline in electron density with increased substrate temperature, and, along with SIMS measurements, suggest that the temperature dependence of the carrier density results from compensation occurring primarily during growth of the cap layer. Similar behavior was observed in $Al_xIn_{1-x}Sb$ samples δ-doped with Si. The recent achievement of high quality quantum wells now allows for optical and low temperature experiments that can be used for the characterization of materials and the study of unique features in the InSb/$Al_xIn_{1-x}Sb$ system.

Chapter 0

Motivation

InSb has the narrowest bandgap, the smallest effective mass, and the highest intrinsic electron mobility of all binary III-V semiconductors. These extreme characteristics make InSb an attractive material for industrial applications, such as infrared devices [1, 2, 3], high-speed field-effect transistors [4], and, in particular, magnetoresistive sensors [5], which play a key role in position sensing applications. At present, Te-doped InSb epilayers are paired with rare-earth metal magnets in automotive position-sensing applications where accuracy and repeatability are critical [6, 7]. These devices exploit a geometrical magnetoresistance where sensitivity is proportional to mobility squared [8], hence, InSb is a natural candidate since its room temperature mobility in thin films is $\mu \approx 60,000 \text{cm}^2/\text{Vs}$. However, InSb also has a very small bandgap, which makes the carrier density ($\approx 2 \times 10^{16} \text{cm}^{-3}$ at 300K), and therefore the sensitivity of the device, largely dependent on temperature. To minimize this dependence, the layers must be doped. The Te-doped sensors consist of a 1.5μm-thick InSb layer grown on a GaAs substrate and have an electron concentration of $8 \times 10^{16} \text{cm}^{-3}$ and a room temperature mobility of μ=40,000cm^2/Vs. Unfortunately, the accompanying increase in ionized impurity scattering reduces the electron mobility and, consequently, the device sensitivity.

Remotely-doped InSb quantum well structures are potentially better suited for magnetoresistance applications than uniformly-doped InSb epilayers. Increased sensitivity is possible since a high mobility can be maintained (since the carriers are spatially separated from the dopant) while achieving a high extrinsic electron concentration. Also, the temperature dependence of the electron concentration can be reduced since only very thin layers of InSb are required, resulting in a low ratio of intrinsic to extrinsic carriers in the well.

Remotely-doped quantum well structures are also used for the study of electrons confined to two dimensions at low temperature and high magnetic field. Many studies have been carried out using such semiconductor quantum well structures as GaAs/AlGaAs and Si/SiGe, and has resulted in the observation of both the integer and fractional quantum Hall effects. However, the unique properties of InSb, including the high intrinsic mobility, large g-factor, and large dielectric constant, makes InSb quantum well structures an attractive alternative platform for conducting basic research of quantum transport.

Both the potential (room-temperature) industrial and (low temperature) basic research applications require the realization of a remotely-doped InSb quantum well. However, the achievement of such a structure was historically difficult due to the lack of a suitable barrier material. An initial attempt was made in the late 1980's using CdTe as a barrier [9]. CdTe has a nearly identical lattice constant to that of InSb, but CdTe is a II-VI material, and cross-doping with the III-V InSb at the interfaces limited the electron mobility in the well to less than 30,000cm^2/Vs [10] at 4.2K. Experiments in the early 1990's demonstrated that quantum confinement in InSb wells could be achieved using $Al_xIn_{1-x}Sb$ barrier layers [11]. In 1994, The University of Oklahoma acquired an Intevac Gen II Molecular Beam Epitaxy (MBE) system,

and hired Assistant Professor Dr. Michael Santos and Research Equipment Specialist Dr. Wing Kwan "Amy" Liu as the chief operators of the III-V system. Following preliminary studies, the first attempt at an InSb quantum well with $Al_xIn_{1-x}Sb$ barrier layers was made in early 1995. In August 1995, the author joined the MBE group.

This work addresses the many growth and materials issues encountered in the realization of high mobility $InSb/Al_xIn_{1-x}Sb$ quantum well structures, as well as the development of simple quantum well models. It also illustrates the structural and electrical characterization methods used to evaluate sample quality.

Chapter 1

Semiconductor Fundamentals

This introductory chapter covers some fundamentals of semiconductor theory. A large portion of this work concerns transport measurements of carrier mobility and density, so the Hall coefficient and the means of experimental determination of carrier density and mobility are derived starting from the Drude Model. The van der Pauw technique is also discussed, and, since this work focuses predominantly on quantum wells, the chapter ends with a discussion of two-dimensional systems.

1.1 Drude Model

The Drude Model [12] is a powerful yet simple classical approximation of electron behavior in a solid. The crystal lattice as a whole is ignored, and overall electrical properties are deduced by considering the collisions of an average electron with immobile positive centers in the crystal.

In the presence of an electric field, **E**, an electron current density, j, will be induced in a conducting wire according to Ohm's Law:

$$\mathbf{E} = \rho \mathbf{j}. \tag{1.1}$$

The proportionality constant ρ is the resistivity of the wire and is related to resistance by $R = L\rho/A$, where L is the length and A is the cross-sectional area of the wire. j

has units of I/A and can be expressed in terms of the concentration of electrons, N, the electron charge, e, and the average electron velocity, $\mathbf{v}$, as:

$$\mathbf{j} = -Ne\mathbf{v}, \tag{1.2}$$

or,

$$\mathbf{j} = -\frac{Ne\mathbf{p}(t)}{m}, \tag{1.3}$$

where $\mathbf{p} = m\mathbf{v}$ is the average electron momentum, and m is the electron mass. Between collisions, the force on a particular electron due to an electric field is given by:

$$\mathbf{F} = m\mathbf{a} = -e\mathbf{E}. \tag{1.4}$$

Integrating this equation with respect to time gives the final velocity, $\mathbf{v_f}$, of the electron: $\mathbf{v_f} = -et\mathbf{E}/m + \mathbf{v_o}$, where $\mathbf{v_o}$ is the initial velocity of the electron immediately after a collision. Since the direction of motion out of a collision is assumed to be random, $\mathbf{v_o}$ averages to zero over the entire electron ensemble. The average time between collisions is the "relaxation time" τ, so the average electron velocity becomes:

$$\mathbf{v} = -\frac{e\tau\mathbf{E}}{m}, \tag{1.5}$$

which we substitute into Equation 1.2 to obtain:

$$\mathbf{j} = \left(\frac{Ne^2\tau}{m}\right)\mathbf{E} = \sigma\mathbf{E}, \tag{1.6}$$

where

$$\sigma \equiv \frac{Ne^2\tau}{m} = \frac{1}{\rho}, \tag{1.7}$$

or,

$$\sigma = ne\mu, \tag{1.8}$$

where, in general,

$$\mu \equiv \frac{e\tau}{m^*}, \tag{1.9}$$

where m^* is the effective mass[1] of the carrier, as defined in Equation 1.34: this generalized value for mass will be used throughout this work. Substituting this value into Equation 1.5, we get:

$$\mathbf{v} = -\mu\mathbf{E}. \tag{1.10}$$

This result indicates that μ is the proportionality constant that relates average electron (hole) velocity to applied electric field. This is an extremely important parameter for the design of semiconductor devices as well as for the study of electrons (holes) at low temperature. Since mobility is also proportional to τ, it is a direct measure of the amount of scattering occurring in a sample and is therefore an indicator of sample quality.

To arrive at the equation of motion for electrons in the wire, we once again focus on a distinct electron. In the time interval t to $t+dt$, the electron will have a collision with a probability of dt/τ, and therefore a probability of no collision of $1 - dt/\tau$. If the electron does not have a collision in this interval, it will evolve under the influence of the force, $\mathbf{F}$, due to the electric field. Considering only the fraction, $1 - dt/\tau$, of electrons that do not have a collision in this time interval[2], the momentum at time $t + dt$ is given by:

$$\mathbf{p}(t + dt) = \left(1 - \frac{dt}{\tau}\right)(\mathbf{p}(t) + \mathbf{F}(t)dt), \tag{1.11}$$

or, neglecting terms of order $(dt)^2$ and taking the limit as $dt \to 0$,

$$\frac{d\mathbf{p}}{dt} = \mathbf{F}(t) - \frac{\mathbf{p}(t)}{\tau}, \tag{1.12}$$

[1] For a free electron, $m^* = m$.

[2] Electrons that do have a collision in the time interval $dt \ll \tau$ will not have gained sufficient momentum to contribute to the total momentum to first order in dt.

which is Newton's 2nd law with a frictional damping term, $-\mathbf{p}(t)/\tau$.

1.2 Hall Effect

1.2.1 Single Carrier System

Figure 1.1 shows the configuration E.H. Hall used for his 1879 experiment. When an electric field E_x is applied in the $+x$ direction of a long, thin, conducting wire, a current density, j_x, is induced in the $+x$ direction[3], with the electrons traveling in the $-x$ direction. If at some later time a magnetic field, $\mathbf{B}$, is introduced in the positive z direction, the electrons experience the Lorentz force:

$$\mathbf{F} = -e(\mathbf{v} \times \mathbf{B}), \tag{1.13}$$

where e is the charge of an electron, and $\mathbf{v}$ is the average electron velocity. If $\mathbf{B}$ is in the $+z$ direction (as shown in Figure 1.1), the Lorentz force deflects electrons moving in the $-x$ direction along the $-y$ direction. In time, this results in a net negative charge on one side of the wire and therefore an electric field, E_y, in the $-y$ direction, which results in a force on the electrons in the $+y$ direction. Equation 1.13 then becomes (in general):

$$\mathbf{F} = -e(\mathbf{E} + \mathbf{v} \times \mathbf{B}). \tag{1.14}$$

Steady-state is reached when enough charge accumulates so that the force in the $-y$ direction due to the magnetic field equals the force in the $+y$ direction due to the electric field.

The accurate solution of the steady-state condition of Equation 1.14 requires that the x and y components of the current and relevant voltages be decoupled. To achieve this, the "Hall bar geometry" [13] is often employed. With the x and y components

[3]The condition that the wire be long and thin eliminates components of the applied electric field in the y and z directions.

decoupled, two quantities can be deduced which lead to the determination of carrier density and mobility in the sample. First, a measurement of E_x and j_x gives the (transverse) magnetoresistance, which Hall found to be independent of B.[4] This quantity is given by:

$$\rho(B) = \frac{E_x}{j_x}. \tag{1.15}$$

The second quantity arises from the condition that the y-components of Equation 1.14 equal zero at steady-state, which implies that E_y is proportional to both v_x (i.e. j_x) and B. This proportionality constant is known as the Hall coefficient and is given by:

$$R_H = \frac{E_y}{j_x B}. \tag{1.16}$$

For the case discussed above, where electrons are the only carriers, E_y points in the $-y$ direction, resulting in a negative R_H. If, however, the carriers in the wire were positive (i.e. holes), E_y would point in the $+y$ direction. Since the measured[5] j_x and B are the same regardless of carrier sign, R_H would, in this case, be positive. Thus, it is possible to determine the sign of the carriers in the system by knowing the sign of R_H.

The carrier density can then be obtained from R_H and Equation 1.12, which for the case of electron current becomes:

$$\frac{d\mathbf{p}}{dt} = -e\left(\mathbf{E} + \frac{\mathbf{p}}{m^*} \times \mathbf{B}\right) - \frac{\mathbf{p}}{\tau}. \tag{1.17}$$

Under steady-state conditions, the current is time-independent, so:

$$-eE_x - \omega_c p_y - \frac{p_x}{\tau} = -eE_y + \omega_c p_x - \frac{p_y}{\tau} = 0 \tag{1.18}$$

[4]This is generally true for most classical systems, but breaks down in the realm of Quantum Physics (See Section 6.2).

[5]An ammeter cannot tell the difference between negative carriers traveling in the $-x$ direction and positive carriers traveling in the $+x$ direction, both of which correspond to a current in the $+x$ direction.

where ω_c is the cyclotron frequency and is given by:

$$\omega_c \equiv \frac{eB}{m^*}. \tag{1.19}$$

Using Equation 1.6 we can rewrite Equation 1.18 as:

$$-\sigma E_x + \omega_c \tau j_y + j_x = -\sigma E_y - \omega_c \tau j_x + j_y = 0. \tag{1.20}$$

At steady-state, $j_y = 0$, so:

$$j_x = \sigma E_x, \tag{1.21}$$

which was the condition before the B-field was applied. and

$$E_y = -\left(\frac{\omega_c \tau}{\sigma}\right) j_x = -\left(\frac{B}{Ne}\right) j_x, \tag{1.22}$$

and the Hall coefficient (Eq. 1.16) is, in general:

$$R_H = -\frac{1}{Ne}, \tag{1.23}$$

and therefore the carrier concentration can be discerned by the experimentally known values of j_x, B, and E_y.

1.2.2 Van der Pauw Technique

The calculations performed in Section 1.2.1 were based upon the assumption that the sample is long and thin, and that the x and y components of the current and voltages were decoupled, which are both good approximations when the Hall bar geometry is implemented. In practice, the realization of the Hall bar geometry is often impractical for routine measurements. Instead, the simpler van der Pauw [14] geometry is employed, which uses only four contacts compared to the required five contacts for the Hall bar geometry. This geometry was used in all the transport measurements discussed in this work, unless otherwise noted. Figure 1.2 shows a representative

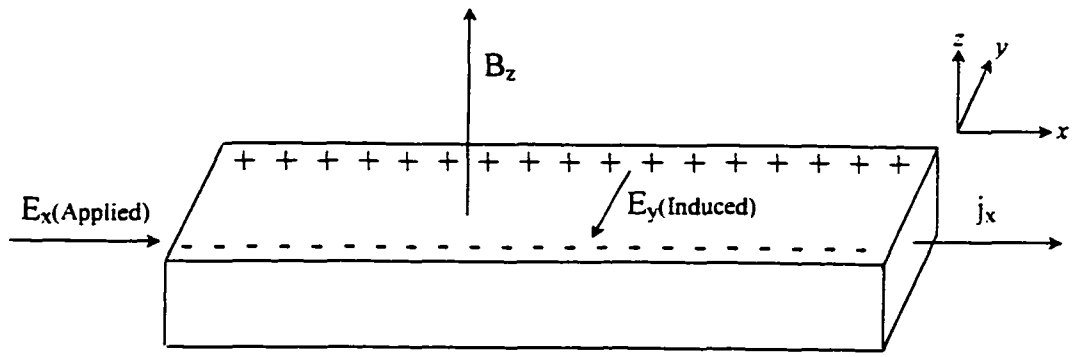

Figure 1.1: Hall's setup. n-type current density in the x direction, j_x, will be deflected by the B field in the z direction, B_z. The accumulation of charge creates an electric field in the y direction, E_y. Steady-state is reached when the repulsive force of E_y equals the deflection force due to B_z.

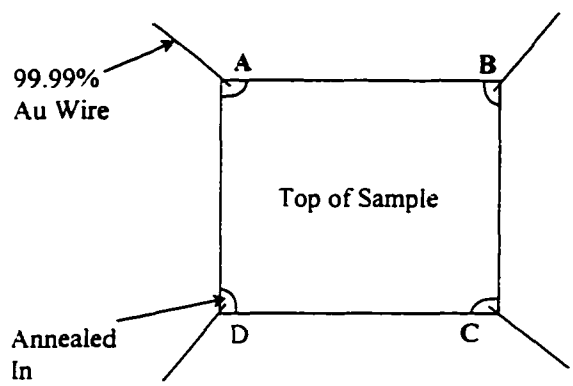

Figure 1.2: Predominant sample (van der Pauw) geometry for electronic transport measurements discussed throughout this work.

square sample along with schematic contacts and associated 99.99% Au leads. See Appendix A for the complete procedure for making contacts.

Through conformal mapping, van der Pauw [14, 15] demonstrated a technique for determining carrier mobility and density for a sample of nearly arbitrary shape, assuming four point contacts arbitrarily spaced on the edge of the sample. The normalized resistivity of the material is then given by:

$$\rho/d = \frac{\pi}{\ln 2}\left(\frac{R_{AB,CD} + R_{BC,DA}}{2}\right) f\left(\frac{R_{AB,CD}}{R_{BC,DA}}\right), \tag{1.24}$$

where d is the thickness of the conducting region of the sample, and $R_{AB,CD}$ is the potential difference, $V_D - V_C$, divided by the current passed from contact A to contact B with no magnetic field, where contacts A-D are defined in Figure 1.2; $R_{BC,DA}$ is analogously defined. The function f is a factor that, for a homogeneous sample, is a function of only the relative position of the contacts, and is given by the implicit relation:

$$\frac{R_{AB,CD} - R_{BC,DA}}{R_{AB,CD} + R_{BC,DA}} = \frac{f}{\ln 2}\cosh^{-1}\left(\frac{\exp(\ln 2/f)}{2}\right). \tag{1.25}$$

If $R_{AB,CD}$ and $R_{BC,DA}$ are nearly equal, f can be expanded:

$$f \approx 1 - \left(\frac{R_{AB,CD} - R_{BC,DA}}{R_{AB,CD} + R_{BC,DA}}\right)^2 \frac{\ln 2}{2} - \left(\frac{R_{AB,CD} - R_{BC,DA}}{R_{AB,CD} + R_{BC,DA}}\right)^4 \frac{(\ln 2)^2}{4} \ldots \tag{1.26}$$

For a homogeneous square sample with point contacts equally spaced (i.e. $R_{AB,CD} = R_{BC,DA}$), $f = 1$, and therefore no correction is applied to Equation 1.24.

In the presence of a magnetic field, B, perpendicular to the sample, $R_{BD,AC}$ becomes a linear function of B (classically), and is analogous to E_y in Figure 1.1. The Hall mobility, μ_H, is then obtained from Equation 1.24 and the slope of $R_{BD,AC}(B)$:

$$\mu_H = \frac{\Delta R_{BD,AC}}{\Delta B}\frac{d}{\rho}, \tag{1.27}$$

and the 2-D density is arrived at from Equations 1.8 and the experimentally determined values from Equations 1.27, and 1.24[6]:

$$n = \frac{N}{d} = \frac{1}{\rho} \frac{1}{e\mu_H}. \tag{1.28}$$

1.2.3 Multiple Carrier System

The preceding discussion has assumed a system comprised of only one type of carrier with constant mobility. This is an idealized case since all actual systems contain carriers with different properties (i.e. (a) electrons and holes, (b) electrons (or holes) with different mobilities in different layers of the sample, or (c), a combination of (a) and (b)). In these cases, the Hall coefficient is no longer given by Equation 1.23. For the case where both electrons and holes are present, and all of the electrons and holes have identical mobilities of μ_e and μ_h, respectively, the Hall coefficient becomes [16]:

$$R_{H,2carriers} = \frac{p\mu_H^2 - n\mu_e^2}{e(p\mu_H + n\mu_e)^2}, \tag{1.29}$$

where n and p are the electron and hole 2-D densities, respectively. For most III-V semiconductors, and particularly for InSb, $\mu_e \gg \mu_h$. Therefore, Equation 1.29 reduces to (approximately) Equation 1.23 for n-doped structures for all temperatures. For p-doped structures at room temperature, sufficient numbers of intrinsic electrons are present such that Equation 1.23 remains valid. However, at low temperatures, a significant number of intrinsic electrons are frozen out and the two terms in the numerator of Equation 1.29 become comparable. For a sufficiently high acceptor concentration, Equation 1.29 eventually passes through zero as the temperature is decreased, causing the apparent density (Eq. 1.28) to pass through a singularity.

[6]Since almost all of the samples are n-type, electron concentrations are taken to be positive, and hole concentrations are taken to be negative, in this work.

This is shown in Figure 1.3 which is a plot of apparent carrier density as a function of temperature for Si-doped InSb on a GaAs(311A) substrate[7] (S483). In this case, the extraction of the relevant parameters in Equation 1.29 requires at least a four-parameter fit to the data.

The approximation made above that μ_e and μ_h are each constant is in fact not the case for actual samples [16, 5, 19], but is a good estimate for the case where the sample is thick and the large number of electrons in the bulk (i.e. isolated from both the surface and substrate-epilayer interface) dominate the conduction. For the simplest case of a single thin epilayer, carriers nearest the substrate will in general have a lower mobility than electrons in the "bulk" due to imperfections at the substrate-epilayer interface; this decrease in mobility is more pronounced if there is a large lattice-mismatch between the substrate and epilayer. Actual systems will also have either an inversion or depletion layer located near the surface, which will cause carriers in this region to have a different mobility than that of their counterparts in the bulk, and depending on the pinning of the Fermi Energy, inversion layers may even behave as 2-D carrier gases at low temperature [19]. An electron surface accumulation layer can be modeled using Petritz's formula [20], and Equation 1.29 can be modified to now include three carrier types [16]:

$$R_{H,3carriers} = \frac{d_{tot}}{e} \frac{d_{tot}\left(P - N\left[\frac{\mu_e}{\mu_h}\right]^2\right) - \left[\frac{\mu_s}{\mu_h}\right]^2 N_s}{\left[d_{tot}\left(P + N\left[\frac{\mu_e}{\mu_h}\right]\right) + \left[\frac{\mu_s}{\mu_h}\right] N_s\right]^2}. \tag{1.30}$$

where d_{tot} is the total thickness of the epilayer[8], μ_s is the mobility of the electrons in the accumulation layer, P is the hole concentration, and N_s is the product of the

[7] Wang, *et al.* demonstrated that Si behaves as an acceptor in GaAs when grown on GaAs(311)A substrates [17] and is a suitable dopant for achieving a high mobility 2D hole gas in the AlGaAs/GaAs system [18].

[8] d_{tot} is used as an approximation since the thickness of the accumulation layer is presumably much smaller than the epilayer thickness.

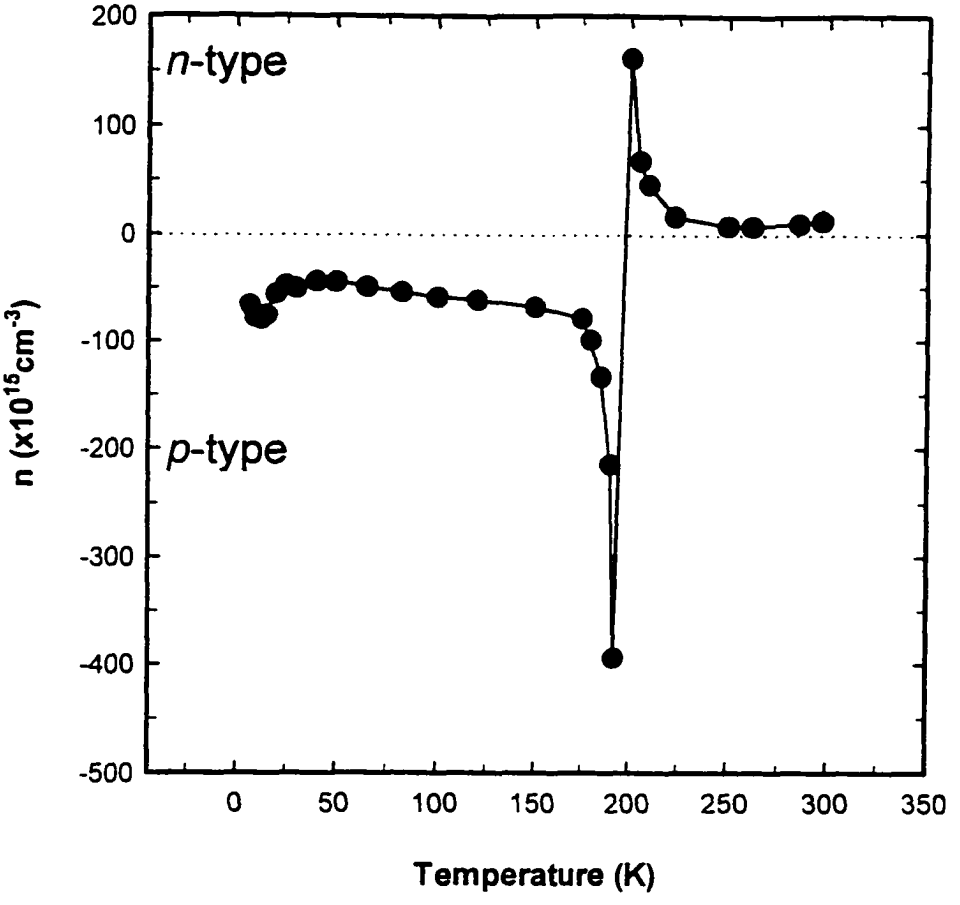

Figure 1.3: Si-doped InSb grown on a GaAs(311A) substrate. The singularity occurring at about T=190K signifies a change in carrier type.

accumulation layer thickness and concentration. We see that by adding one extra layer, we increase the number of fitting parameters from four to six. The situation grows even more complex if, instead of a single epilayer, the sample consists of many different types of semiconductor, as shown in Figure 5.1. Here, not only have we increased the number of interfaces, but we now have a situation where the intrinsic bulk mobilities vary from layer to layer. Since the actual solution is so prohibitive, simplifying assumptions are made, as discussed in Section 5.4.1.

1.3 Dispersion Relation and Effective Mass

1.3.1 Bloch's Theorem

The Drude Model (Sec. 1.1) uses simple assumptions to arrive at the properties of an overall electron ensemble based on the collisions of an "average" electron. While powerful in many respects, the theory does not take into account the quantum mechanical nature of electrons or the overall periodicity of the underlying crystal and is therefore fundamentally limited. These properties are accounted for in Bloch's Theorem [12, 21, 22].

Bloch assumed the electrons are confined to a perfect crystal, and therefore the potential "felt" by the electron is periodic in 3 dimensions and given by:

$$U(\mathbf{r}+\mathbf{R}) = U(\mathbf{r}), \tag{1.31}$$

where $\mathbf{R}$ is the periodicity of the Bravais lattice. To aid in the ease of solution, Bloch made the (free electron) approximation that the potential felt by each electron is dominated by the nuclei in the lattice, and that electron-electron interactions were negligible. As such, the wave function of a particular electron arises from the time-

independent solution of the Schrödinger equation:

$$H\psi = \left(-\frac{\hbar^2}{2m}\nabla^2 + U(\mathbf{r})\right)\psi = E\psi, \tag{1.32}$$

where ψ is the electron eigenstate, H is the Hamiltonian, and E is the electron energy. Bloch's Theorem states that the eigenstates are given by a plane wave times a function with the same periodicity as the reciprocal lattice:

$$\psi_{n\mathbf{k}}(\mathbf{r}) = e^{i\mathbf{k}\cdot\mathbf{r}}u_{n\mathbf{k}}(\mathbf{r}), \tag{1.33}$$

where $\mathbf{k}$ is analogous, but not equal, to the free electron wavevector, $\mathbf{p}/\hbar$.[9] Instead, the components of $\mathbf{k}$ are the quantum numbers arising from the periodicity of the crystal potential, and knowledge of the dependence of the electron energy on $\mathbf{k}$ leads to a determination of the band-structure and, therefore, many of the electrical properties of the material.

It can be shown [22, 21] that electrons in a periodic potential will evolve under the influence of a force according to Newton's second law only if the electron mass is normalized as:

$$m^* = \left(\frac{1}{\hbar^2}\frac{d^2E}{dk^2}\right)^{-1}, \tag{1.34}$$

where the dispersion relation is given by:

$$E = \frac{\hbar^2k^2}{2m^*}. \tag{1.35}$$

If E is a quadratic function of k in Equation 1.34, the electron effective mass will be independent of electron energy. Table 1.1 lists the band edge effective mass at 300K for some widely used semiconductors.

Table 1.1 also lists some other parameters for various semiconductors, and Figure 1.4 shows a plot of energy gap as a function of lattice constant.

[9] $\hbar\mathbf{k}$ is not a momentum since the Hamiltonian does not have spatial translation invariance for a periodic potential, and, therefore, the eigenstates will not be simultaneous eigenstates of the momentum operator.

	InSb	GaAs	InAs	Si
Electron Effective Mass (m_Γ)	0.0145	0.067	0.023	1.1
Intrinsic Electron Mobility ($cm^2V^{-1}s^{-1}$) (300K)	80,000	8,500	33,000	1,500
Hole Effective Mass ($cm^2V^{-1}s^{-1}$)	0.4	0.5	0.4	0.5
Intrinsic Hole Mobility ($cm^2V^{-1}s^{-1}$) (300K)	1,250	400	460	480
Bandgap (eV) (300K)	0.18	1.42	0.36	1.11

Table 1.1: Electrical properties of various semiconductors.

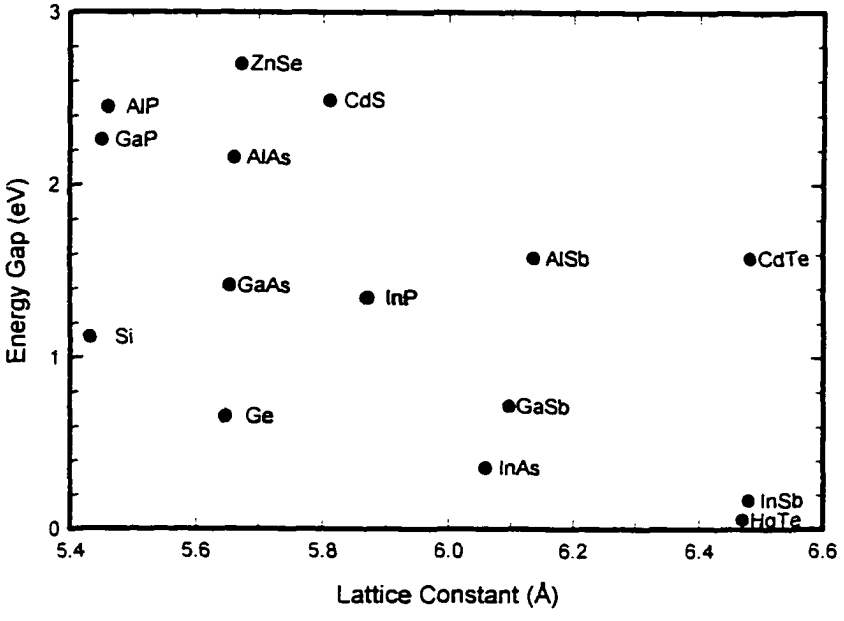

Figure 1.4: Energy gap as a function of lattice constant for several semiconductors. InSb has the smallest energy gap and the largest lattice constant of all III-V semiconductors.

1.3.2 3-D Density of States

For a Bloch electron (Sec. 1.3.1) that is unconfined in the x, y and z directions, the density of states, $D_{c,v}(E)$, for a constant effective mass in either the conduction or the valance band is given by [23]:

$$D_{c,v}(E) = \left(\frac{1}{2\pi^2}\right)\left(\frac{2m^*}{\hbar^2}\right)^{3/2} E^{1/2}, \tag{1.36}$$

which depends explicitly on the electron energy, and, due to the dependence on effective mass, the density of states in the valance band is typically larger than in the conduction band. The concentration of electrons at $T = 0$K is then obtained by integrating Equation 1.36 through all energies up to the Fermi Energy, E_F, for a constant effective mass:

$$N_e = \int_0^{E_F} D(E)dE = \left(\frac{1}{3\pi^2}\right)\left[\frac{2m_e^* E_F}{\hbar^2}\right]^{3/2}. \tag{1.37}$$

1.3.3 Kane's Model

The case of a parabolic dispersion relation is a good approximation near the bottom of all III-V semiconductor conduction bands, and for semiconductors with bandgaps, E_g, that are large. However, for semiconductors with small E_g, such as InSb, interactions between the conduction, light hole, heavy hole, and spin-orbit split-off bands cause the dispersion relation for the conduction band to become increasingly non-parabolic as E_g is reduced. These interactions were first modeled by Kane, and the model is known as the $\mathbf{k} \cdot \mathbf{p}$ or 4-Band Model [24]. A simplified version, the 2-Band Model, ignores spin-orbit splitting and takes into account only the conduction band and one of the hole bands. This approximation is valid in the region between the bottom of the conduction band and the inflection point which occurs between the conduction band minimum and the Brillouin zone boundary [25]. The 2-Band

effective mass is given by [26]:

$$m^*(E) \approx m^*_\Gamma \left(1 + \frac{E}{E_g}\right), \tag{1.38}$$

where m^*_Γ is the electron effective mass at the Γ-point of the conduction band.

1.4 The Square Quantum Well

1.4.1 Solution of Energy Levels

If the electron remains unconfined in the x and y directions, but is now confined in the z direction by an infinite potential barrier at $\pm a/2$, where the potential is zero for $\mid z \mid \leq a/2$, an exact solution to the Schrödinger equation exists for a constant effective mass, giving the allowed quantized electron energies [23]:

$$E_i = \frac{i^2 \pi^2 \hbar^2}{2m^* a^2}, \tag{1.39}$$

where $i = 1, 2, 3...$ denotes the energy level. The total electron energy then becomes:

$$E_{tot} = E_i + \frac{\hbar^2}{2m^*}\left(k_x^2 + k_y^2\right), \tag{1.40}$$

where k_x and k_y denote the wavevectors in the unconfined x and y directions. If a is sufficiently small, the electrons are "trapped" in an approximate plane, creating a two-dimensional electron gas (2DEG).

An approximation to the square well can be physically realized by sandwiching a low bandgap material between a higher bandgap material. However, in this case, the potential felt by the electron at the edge of the well is no longer infinite, and the Schrödinger equation requires the solution of a transcendental equation to arrive at the allowed electron energy levels [27]. However, if the barrier height is sufficiently high, Equation 1.40 is a good approximation.

For the case where there is more than one electron in the quantum well, electron-electron interactions alter the potential felt by each electron from that of the original square well. The resulting potential can then be solved self-consistently [28], in which Poisson's equation and the Schrödinger equation are solved iteratively until the change in the calculated potential per iteration drops below some prescribed value.

1.4.2 2-D Density of States

For the situation described in Section 1.4, the density of states becomes:

$$D^{2D}_{parabolic} = \frac{m^*}{\pi\hbar^2}. \tag{1.41}$$

Hence, in a 2DEG, the density of states is energy independent for semiconductors with a parabolic dispersion relation (i.e. m^* is independent of energy). However, m^* has energy dependence in semiconductors with small E_g (Sec. 1.3.3), and therefore the density of states for a non-parabolic dispersion relation becomes:

$$D^{2D}_{non-parabolic} \approx \frac{m^*_\Gamma}{\pi\hbar^2}\left(1 + 2\frac{E}{E_g}\right), \tag{1.42}$$

and the carrier density at $T = 0$K is obtained from:

$$n = \int_0^{E_F} D^{2D}(E)dE. \tag{1.43}$$

Chapter 2

Molecular Beam Epitaxy (MBE)

The 1950s and 1960s saw remarkable advances in the study and realization of semiconductor devices. As device performance and speed became affected by structural quality and size and more complicated and precise design parameters were desired, thin-film deposition technologies were developed. What we would recognize today as Molecular Beam Epitaxy (MBE) was first used in the 1970's, and differed from previous thin film techniques, such as liquid phase epitaxy, chemical vapor deposition, and sputtering, by the relatively high control of growth conditions. MBE occurs via the reaction between one or more thermal molecular/atomic beams and a crystalline substrate surface. Growth under Ultra-High Vacuum (UHV) conditions ($\leq 10^{-9}$Torr) allows for a low unintentional impurity density ($\leq 10^{15}$ cm^{-3}), and the *in situ* monitoring of crystalline quality through techniques such as Reflection High-Energy Electron Diffraction (RHEED), Auger Electron Spectroscopy (AES), and X-ray Photoelectron Spectroscopy (XPS). MBE is therefore employed where precise control of layer thickness, sample purity, and alloy concentration is critical [29, 30, 31].

The experimental set-up for MBE is shown schematically in Figure 2.1. Source material is evaporated from effusion cells, and the material is "directed" at the sample

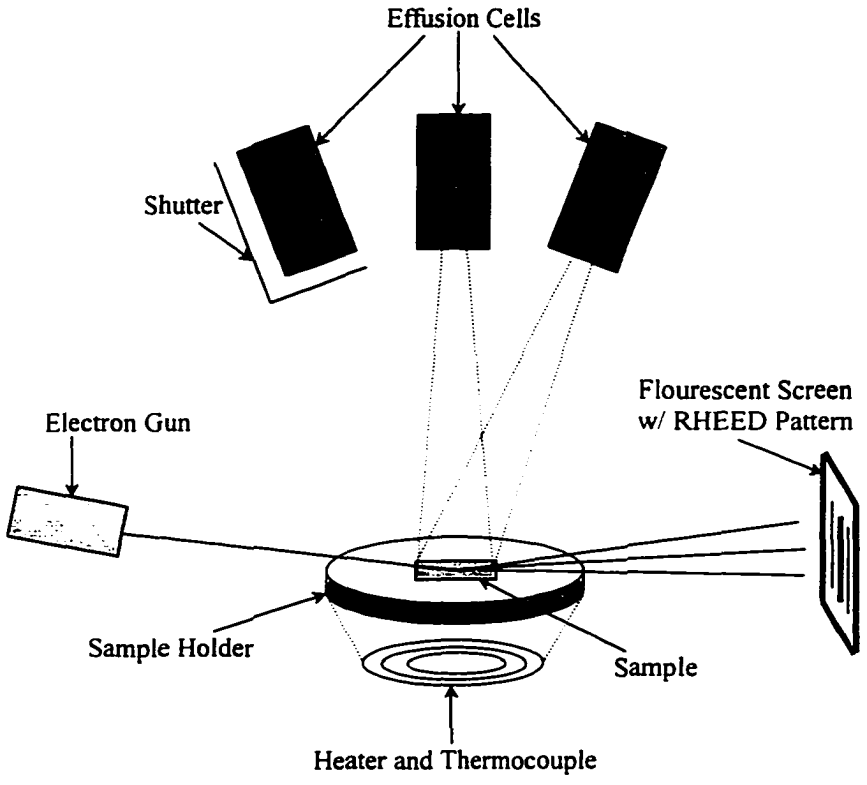

Figure 2.1: Schematic set-up for MBE. The molecular beam emerging from an effusion cell is turned "on" and "off" by the shutter. The electron gun and fluorescent screen comprise the RHEED equipment (Sec. 2.2). The sample is heated from behind and can be rotated to minimize any inhomogeneities in the molecular beams.

surface by opening one or more effusion cell shutters. The sample is radiatively heated from behind, and a thermocouple is placed near the back of the sample block. Also shown in Figure 2.1 is an electron gun and fluorescent screen, which is used for RHEED experiments as discussed in Section 2.2. The sample is rotated (3-4RPM in this work) to minimize inhomogeneities in the flux of the impinging molecular beams.

Two different types of sample holders are typically used in MBE. The first is known as an In bonding block, in which the substrate is held in place by the surface tension of molten In. The second, or non-In bonding block, holds the sample firmly in place after it is inserted between two plates. In the latter type of block, a sapphire plate is placed behind the sample to disperse the heat and provide for homogeneous heating of the sample, which is a key advantage over the In bonding block. Both types of blocks were used in this work, with better growth occurring on the non-In bonding blocks. Since residual In remains on the back of the sample after growth using an In bonding block, the non-In bonding block is desirable for optical experiments involving transmission.

2.1 MBE Growth Modes

There are three basic growth modes for MBE [29]. The first is "layer-by-layer", or Frank-van der Merwe, growth. In this mode, the impinging atoms/molecules are more tightly bound to the substrate than to each other, causing the first layer of atoms to cover the substrate before the next layer is significantly started. If the second and ensuing layers are somewhat less tightly bound than the preceding layer, but still stronger than the binding energy in the bulk of the deposited material, then layer by layer growth is maintained. Frank-van der Merwe growth is often seen for

semiconductor growth on semiconductors.

If the opposite case is true, in which the impinging atoms are more tightly bound to each other than the substrate, then "island", or Volmer-Weber, growth is observed. Here, small clusters of atoms nucleate on the substrate and expand into islands as more material is deposited, until eventually the bases of the islands spread to completely cover the substrate.

The final mode, "layer plus island", or Stranski-Krastinov, growth, is a combination of the first two modes. Here, the first layer(s) is (are) deposited, after which layer-by-layer growth is energetically unfavorable, and islands are formed on top of the initial layer(s). This mode is observed when some mechanism, such as lattice dislocations, exists to alter the monotonic decrease in binding energy with each successive layer from that of the substrate to that of the deposited bulk [29].

2.2 Reflection High Energy Electron Diffraction (RHEED)

The condition of the crystal surface is of utmost importance prior to and during epitaxy. One way of evaluating surface quality is through a technique known as Reflection High Energy Electron Diffraction (RHEED), which is schematically shown in Figure 2.1. High energy electrons (5-40keV) are directed at the substrate at a low angle of incidence ($1^o - 3^o$); the low angle of incidence ensures that penetration into the bulk of the sample is minimal [32]. The ensuing diffraction pattern is then interpreted from a phosphorus screen. The diffraction pattern gives information relating to the crystalline quality and temperature (Sec. 2.2.1 and 2.2.2), and oscillations in the diffraction intensity provide the growth rate (Sec. 2.3.2) if near layer-by-layer growth conditions are realized.

2.2.1 Origin of the RHEED Pattern

If we consider only the topmost array of atoms on a "flat" surface, we have a two-dimensional system in which the third dimension is missing in real space. Therefore, the third dimension is undefined in reciprocal space, and the surface is represented in reciprocal space by a set of rods. These rods have a non-zero width due to thermal vibrations and lattice imperfections, and the Ewald sphere (Sec. 3.1) has a non-zero thickness due to the dispersion in both incident electron energy and direction of the electron beam. In RHEED experiments, an electron energy is used such that the Ewald sphere radius is much larger than the spacing of the rods (Sec. 2.3.2). The combination of the non-zero widths of the rods and Ewald sphere combined with the small curvature at the boundary of the Ewald sphere results in a broad range of overlap in reciprocal space where the Bragg (Laue) condition is satisfied (Sec. 3.1). Therefore, a streaky RHEED pattern is exhibited for a "good" 2-D-like surface. The pattern becomes increasingly spotty as the surface becomes more 3-D-like (i.e. less "rod"-like and more "point"-like in reciprocal space), thus RHEED provides important information about the quality of the sample surface.

2.2.2 Surface Reconstruction

Atoms on the surface of a covalently bonded semiconductor, such as InSb, will have incomplete, or "dangling", bonds compared to the atoms in the bulk of the semiconductor. Hence, surface atoms of a crystalline solid will rearrange themselves in a periodic fashion, or "surface reconstruction", and form bonds with neighboring atoms to reduce the number of dangling bonds and therefore the overall energy[1]: it has been postulated [33] that the only intrinsic surface reconstructions for InSb are

[1] The same phenomenon also occurs in amorphous or polycrystalline materials, but the surface atoms will in this case lack a long range periodicity.

the (2×4)/c(2×8) Sb-dimer-terminated and the (4×2)/c(2×8) In-dimer-terminated structures. Since the periodicity of the surface reconstruction is correlated to the periodicity in the bulk [29], a clear picture of the relative orientation of surface atoms provides information about the crystallinity, and therefore quality, of the underlying crystal.

Substrate surface temperature is of critical importance during MBE. The substrate surface needs to be sufficiently hot to allow for the hopping diffusion of atoms into low energy sites, but the substrate needs to be sufficiently cool to prevent excessive desorption of surface atoms and to prevent the bulk diffusion of dopants and other atoms across heterojunctions. Since surface reconstructions are an energy minimization mechanism, different reconstructions (phases) will occur in different temperature regimes. As a result, the temperature at the surface of a semiconductor can be deduced independently of thermocouple reading by monitoring changes in surface reconstruction (phase). This is particularly important for the growth of a narrow-bandgap material on a wide-bandgap material (e.g. InSb on GaAs). As shown in Figure 2.1, the substrate is radiatively heated from behind, and the thermocouple is located behind the sample. Before growth, photons of energy greater than the substrate bandgap will be absorbed which results in the heating of the substrate. Upon subsequent growth of a narrow-bandgap semiconductor, the epilayer will absorb radiation across a wider spectrum range, resulting in a temperature disparity between the surface (where epitaxy occurs) and the back of the substrate (where temperature is measured). Shanabrook *et al.* [34] demonstrated that for InAs or GaSb grown on GaAs, the surface temperature increases by nearly 150°C for a thermocouple temperature increase of only 10°C for a layer thickness of 1μm. Since InSb has a smaller bandgap than both InAs and GaSb, we expect an even

greater deviation in epilayer vs. thermocouple temperature. The monitoring of surface reconstruction through RHEED is therefore extremely important for accurate temperature measurement in our material system.

Atoms impinging on the surface during epitaxy will fill the sites that are the most readily available, where available sites are determined by the surface reconstruction. It is therefore important to reproducibly prepare the sample surface to that which provides for the best growth conditions. We have found that the surface resulting in the best growth of InSb is the pseudo-1 x 3, hereafter denoted as '1 x 3'.[2] In addition, knowledge of the available sites is important since the incorporation of (group IV) dopants is sensitive to the available sites on the surface. Knowledge of the reconstruction is therefore important to avoid unwanted autocompensation effects. This topic will be addressed in Chapter 4.

The group-V/group-III flux ratio is of critical importance. Excess group-V atoms (i.e. atoms that have not yet bonded with a group-III counterpart) on the surface will desorb, while excess group-III atoms will remain on the surface [36]. For the case of InSb growth, excess In on the surface will be incorporated into the sample, resulting in one or more of the following: In droplets, complexes involving both In and Sb, Sb vacancies, and In incorporation in Sb sites. As a result, the group-V/group-III flux needs to be larger than unity for the stoichiometric growth of III-V coumpounds, but small enough for the group-III atoms to reach equilibrium sites, such as step edges, before bonding with group-V atoms. In short, the group-III flux determines the growth rate, and the group-V flux determines the degree of stoichiometry.

Figure 2.2 shows a phase diagram of the InSb surface in a plot of the ratio of

[2]RHEED studies suggest that the '1 x 3' diffraction pattern arises from the combination of different 2 x 4 phases [33]. Recent STM experiments suggest that the '1x3' is actually a disordered, "worm-like" (1x3)[35].

incident beam fluxes as a function of OU III-V chamber thermocouple temperature [37]. The surface reconstruction depends only weakly on flux ratio when it is much greater than unity, but has a stronger dependence for a small ratio. The flux ratio and growth rate leading to optimal growth are determined experimentally. We have used a nominal flux ratio of 1.2 and a nominal growth rate of .8 ML/s throughout this work.

Finally, using the Ewald sphere construction and the Bragg equation (Eq. 3.1), one can deduce the surface atom periodicity, d, by measuring the position of the diffraction streaks:

$$d = \left(\frac{\lambda L}{D}\right), \tag{2.1}$$

where L is the distance between the sample and the fluorescent screen, and D is the distance between streaks in the observed diffraction pattern.

2.3 MBE at OU

The University of Oklahoma utilizes an Intevac Modular Gen II with two-growth chambers and a shared central analysis chamber. The analysis chamber contains XPS and AES equipment and isolates the III-V (Physics) and IV-VI (Electrical Engineering) growth chambers from each other to reduce the effects of cross-contamination.

2.3.1 Pumps

Pressure in the growth chamber is maintained below 1×10^{-10}Torr when idle (and below 5×10^{-10}Torr during growth) through the use of a number of pumping mechanisms [36, 38]. The first is the encapsulation of the growth chamber in a shroud cooled by a liquid nitrogen bath. Molecules of low energy collide with the sides of the shroud and adhere to the walls, resulting in a lower pressure. The second (cryogenic)

pumping mechanism operates on the same principle as the first: a refrigerator which uses compressed He gas as a refrigerant is maintained at $\leq$10K, causing most gases (e.g. N_2, O_2, CO_2) to condense and remain trapped. The pump can reach pressures as low as 1×10^{-11}Torr and is regenerated by warming the cold stage and pumping away the evaporated material.

Next, we use an ion pump, in which constituent atoms are ionized by collisions with electrons generated from a dc discharge. The ions are then accelerated across a potential difference of about 5kV and collide at high energy with a strip of Ta foil where the ions are absorbed. For pressures above about 10^{-2}Torr, the electrons cannot generate enough kinetic energy for an ionizing collision, so the system is first roughed by a molecular drag pump, which consists of a turbine rotating at high speed; this type of pump can reach pressures below 1×10^{-4}Torr. However, the mean free path of the discharged electrons in the ion pump below 1×10^{-4}Torr is long, resulting in a low probability of an ionizing collision between an electron and constituent molecule before the electron leaves the pumping area. To pump below 10^{-4}Torr with an ion pump, a magnetic field of about 0.1T is applied perpendicular to the electron trajectory to lengthen the electron path, which increases the probability of an electron/molecule collision that would ionize the molecule. Ion pumps with this type of configuration are capable of reaching below 1×10^{-10}Torr.

Finally, we have a titanium sublimation pump (TSP) in the buffer and growth chambers, in which titanium is thermally evaporated onto the chamber walls. Titanium getters large quantities of reactive gasses either through the formation of surface compounds, such as TiO, or through the absorption of active gases. After the titanium becomes saturated, another thermally evaporated coat can be applied on top of the previous coat.

Mechanical and diffusion pumps are not used in the system to eliminate the potential for contamination through the backflow of pump oil.

2.3.2 Determination of Growth Rate

One of the primary advantages of MBE over other deposition techniques is the precise control of layer thickness, so the determination of growth rate is of fundamental importance. Growth rates for MBE are typically about 1ML/s (or about 3Å/s) which can be calibrated through RHEED by observing oscillations in the specular beam intensity. We use an electron beam energy of 9.5keV which corresponds to a de Broglie wavelength of about 0.13Å, which is small compared to the bulk lattice constant for InSb of 6.4794Å. This results in an Ewald sphere (Sec. 3.1) that is much larger than the inter-rod spacing in reciprocal space (Sec. 2.2.1).

In the idealized case of Frank-van der Merwe growth (Sec. 2.1), a completed monolayer will result in the most intense diffraction pattern since the observed intensity is directly related to the smoothness of the sample surface. As material is deposited on the surface, the sample becomes increasingly "rough", and the intensity decreases, reaching a minimum intensity at 0.5ML. The intensity then increases back to the maximum value as the layer is completed. Thus, by measuring the period between intensity maxima, the growth rate is determined [30, 39].

The sample is first annealed to obtain a flat surface. Atoms impinging on the surface combine to form stable clusters at random locations on the surface; a completed surface is formed by the merging of the clusters. Most adatoms are desorbed when they are deposited far from a cluster since they are unable to reach an equilibrium position at a step edge[3]. Because of this, one would expect that the first layer grown

[3] As a result, one expects that the growth rate is slow at the start of a layer, reaches a maximum at some point through the completion of the layer as the number and size of the clusters increases, and returns to the minimum rate as there become fewer voids and the layer is completed [39, 30].

after annealing would be completed before the second layer is significantly started. However, as growth proceeds, the probability of simultaneous growth of multiple layers increases, which amounts to the roughening of the surface. As a result, the surface prior to growth exhibits the most intense reflection, and as growth begins, the specular beam intensity oscillates and the amplitude of oscillation decays as the surface becomes rougher due to the existence of multiple partial layers. Eventually, the specular beam reaches an approximately constant intensity. When growth is stopped, the intensity quickly increases as the surface is annealed [30, 39].

The number of monolayers grown before the oscillations decay to zero varies for different binary systems. After about 1μm of GaSb[4] is grown directly on GaAs, we typically measure between 12 and 15 oscillations. If we then grow a subsequent 1μm AlSb layer, we typically can measure about 20 periods. Finishing with a 1μm InSb layer, we nominally measure 7 periods.

The reason for the deviation in the number of measured oscillations amongst these materials is currently under investigation, but likely has a direct link to the relaxation due to the large difference in lattice constant between these materials. GaSb differs in lattice constant by about 7% from that of GaAs (Fig. 1.4), so a large number of defects are likely to be present. AlSb has an almost identical lattice constant to GaSb. Since fewer defects propagate as a layer is grown more thick, a higher crystalline surface is likely available. And since we always grow AlSb on GaSb, it is expected that the AlSb layer will be of higher quality than the GaSb layer, resulting in more Frank-van der Merwe-like growth (Sec. 2.1). Finally, InSb differs in lattice constant by about 15% to that of GaAs. It therefore has defects propagating

[4]For AlSb, GaSb, or InSb grown on a layer of largely differing lattice constant, the RHEED pattern is spotty for the first several minutes, indicating island growth predominates. Eventually, the islands coalesce to form a relatively smooth surface. A buffer layer of 1μm has proven sufficient to achieve a smooth surface.

through the GaSb and AlSb layers as well as defects due to the relaxation occurring at the AlSb-InSb interface.

The growth rate is obtained through the procedure outlined above by capturing the RHEED image with a Panasonic Model WV-BP104 CCD camera and KSA RHEED 300, version 3.0, software. The growth rate as a function of beam flux, or Beam Equivalent Pressure (BEP), is then obtained by rotating an ion gauge into the path of the individual molecular/atomic beams after the growth rate is determined. The ion gauge ionizes the constituent atoms/molecules in the beam, and the ions are then collected on a cathode plate, which results in a current that can be correlated to a partial pressure [30]. Since the growth rate measurement procedure outlined in the preceding paragraph often takes days[5], the monitoring of BEP for each cell provides an estimate of the growth rate on a daily basis.

2.3.3 Source Material/Effusion Cells

All of the samples in this work were grown in the III-V chamber, which allows for a maximum of 8 source effusion cells. For each growth run, we currently have the option of In, Si, Al, Ga, Be, uncracked Sb, an EPI Sb cracker, a GaSb source Sb cracker, and As cells; the As cell has as of yet not been installed due to concern over As contamination of InSb and $Al_xIn_{1-x}Sb$ layers. Since sample purity depends directly on the purity of the source material, we buy high purity source material from various vendors: In (7N RASA), Al (6N Ulvac), Sb (6.5N Dowa), Ga (7N Eagle-Picher) and Si (Silicon Sense).

It is desirable to use less than the maximum number of cells in order to allow for viewports to be installed. This allows us to view, through the reflection off a

[5] It is difficult, particularly for InSb, to prepare the substrate surface through growth and annealing, isolate the correct substrate temperature, and determine the proper group V/group III flux ratio that will best approximate Frank-van der Merwe growth.

substrate, the existing effusion cells and shutters to check for blockages, shutter malfunctions, and the amount of remaining source material. It is particularly important to see inside the Al cell. Al wets to the Pyrolytic Boron Nitride (PBN) crucible and tends to flow uphill as it is melted and spill over the edge of cell. As a result, the Al temperature is ramped slowly ($\approx .02^{o}$C/s) until the Al is melted, and thereafter ramped at a nominal rate of $.1^{o}$C/s; other cells are nominally ramped at 1^{o}C/s.

In addition, the density of Al changes significantly as it passes through the liquid-solid transition, which increases the stress on the PBN cell during solidification which could lead to the cracking of the crucible; the greatest risk of this occurs during a power outage. Once cracked, a subsequent melt of the Al would result in a leak. To accommodate this risk, we use a double walled crucible, so any leakage through a crack in the inner wall will be confined by the outer wall. Evidence for a leak can then be obtained by visually inspecting the crucible once the chamber is opened.

The Sb cracker cell consists of a tantalum effusion cell leading to a long ($\approx$ 6in) "cracking" tube which is heated to a high temperature (nominally 900^{o}C) which disassociates Sb_4 into $2\times Sb_2$ and $4\times Sb$. Cracked Sb has been shown to result in better stoichiometric growth for the growth of GaSb than Sb_4 [40] and improved optical efficiency in GaInSb/InAs superlattices [41]; the uncracked Sb cell was not used for any of the samples discussed in this work. All of the other effusion cells are standard PBN Knudsen cells [29, 36].

Effusion cell temperature set-points corresponding to the same growth rate vary between growth runs due to a number of factors, including the amount of source material in the crucible and partial blockage of a cell by a shutter. Effusion cell temperatures for a given growth rate are typically: In=840°C (0.8ML/s), Al=1040°C (0.09ML/s), Sb=455°C(bulk)/900°C(cracker) (1ML/s), Si=1305°C (doping density

of $8\times10^{10}cm^{-2}s^{-1}$), and Ga=950°C (0.8ML/s).

2.3.4 Preparation of GaAs Substrates

Substrate quality is obviously also of great importance in the realization of high quality samples. Epi-ready (etch pit density < $5000cm^{-2}$) and mechanical grade (possible micro-twin or lineage on up to 20% of wafer surface) Semi-Insulating (SI) GaAs substrates are purchased from American Xtal Technology (AXT). The nominal orientation is (001) with a $\pm0.1^o$ offcut, but we have also carried out experiments with a 2^o offcut and also with (311)A oriented substrates (see, for example, Sec. 1.2.3). SI GaAs substrates are required to eliminate a parallel conduction path at all temperatures during routine Hall measurements (Sec. 1.2.3), to minimize our daily growth cost, and for potential industrial applications (Chap. 5).

Epi-ready substrates require no chemical preparation prior to loading if they are loaded within 3 months of their creation. Mechanical grade substrates are of somewhat lower quality, and the manufacturer recommends a wet chemical etch (see Appendix B) prior to loading to remove the native oxide and carbon contaminants. In general, we have found that this etch is not necessary and that small processing errors result in large etch pits on the surface. However, "old" wafers are etched to remove excess surface oxide and contaminants to increase sample quality and reduce residual chamber contamination.

The native oxide of GaAs is typically desorbed at an OU thermocouple range of 600-650°C, well below the 1238°C melting point of GaAs, after a temperature ramping period of about one hour. The temperature is ramped slowly to avoid excessive outgassing of the substrate and substrate block. Evidence of an acceptable substrate surface arises from a RHEED pattern demonstrating a (2×4) surface reconstruction.

Since we have not installed an As cell to provide an As overpressure, the best starting surface we can obtain has facets on the streaks on the [1 $\bar{1}$ 0] azimuth.

2.3.5 Preparation of InSb Substrates

Both *p*-type (Cd doped) and *n*-type (undoped) InSb wafers are purchased from Johnson Matthey with etch pit densities $< 40\text{cm}^{-2}$. InSb substrates are not useful for room temperature electrical measurements since high-mobility intrinsic electrons in the substrate dominate the conduction due to the small bandgap (Table 1.1), even for *p*-type substrates (Sec. 1.2.3). However, InSb substrates are useful for comparative structural studies (Chapter 3) and potentially for low-temperature electrical measurements, where kT can be made significantly smaller than the bandgap of the substrate.

Difficulties arise in the thermal desorption of the InSb native oxide due to the low melting point of InSb (525°C) and the low vapor pressure of one of the oxide species, In_2O_3 [42]. We typically observe a '1×3' RHEED pattern without arrowheads on the streaks, indicating the oxide desorption is complete [43], at an OU thermocouple reading of 450-500°C after a temperature ramping time of about four hours. The temperature is ramped slowly in this case to avoid temperature overshoot, which would result in the melting of the substrate.

All of the InSb substrates are etched using a modified CP4A [44, 45] bath (see Appendix C), which produces a passivating oxide that is least difficult, of those tested, to thermally desorb. This is also required since thermal desorption alone is ineffective in eliminating high concentrations of carbon contaminants[6] [46, 47].

There are two other common *in situ* oxide removal techniques. The first is the cyclic process of ion bombardment of the substrate followed by annealing. This

[6] Carbon is a group-IV element and would act as a dopant in our III-V layers.

method is highly effective in removing the oxide and carbon contaminants, but is known to form In droplets on the surface due to preferential sputtering and can result in crystallographic damage [48] and modify the electrical properties of the surface layer [46]. The second, and highly successful, *in situ* technique is that of using a hydrogen plasma for the removal of the oxide [49]. Neither of these methods are currently used at OU.

2.3.6 Outgassing

Substrates are initially loaded into the entry/exit chamber and outgassed at 200°C for at least two hours at a pressure of about 10^{-7}Torr. The substrates are then transferred into the buffer chamber where each substrate is outgassed at 350°C for at least 24 hours at a pressure of about 10^{-10}Torr before being transferred into the growth chamber. Once in the growth chamber, the substrate is outgassed at 375°C at a pressure less than 10^{-10}Torr for at least 12 hours.

After each of the growth chamber openings, all three chambers are baked for at least three days at a nominal temperature of 200°C. Following this, each of the effusion cells are outgassed for at least two hours at a temperature at least 10°C above their maximum intended operating temperature. Before each growth, each cell is again outgassed at 10°C above their intended temperature for the day for at least ten minutes.

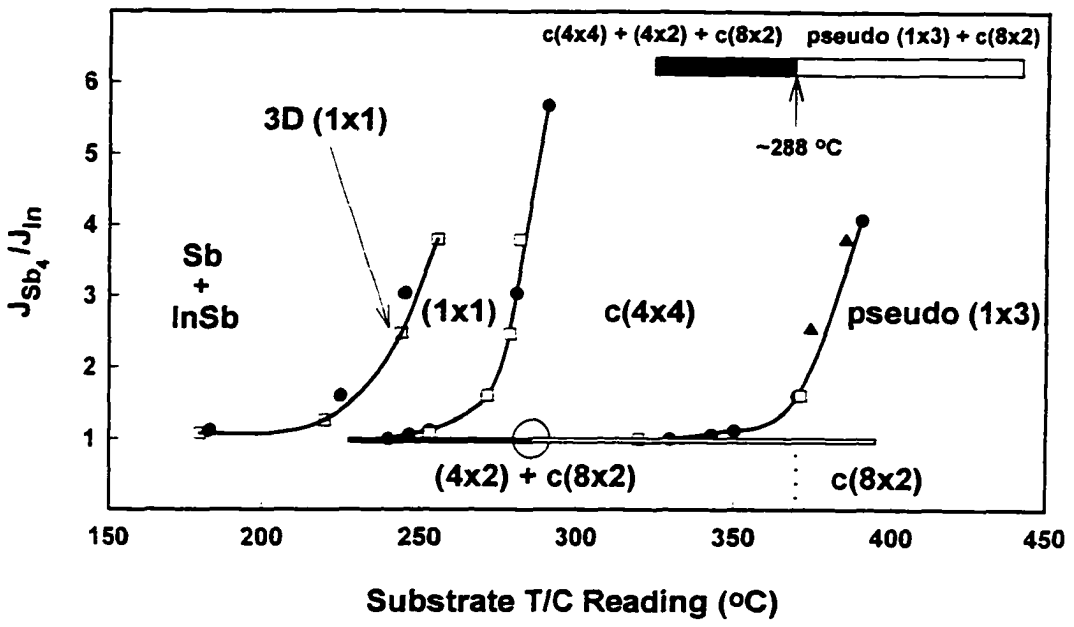

Figure 2.2: Incident flux ratio as a function of OU Thermocouple reading. We obtain the best stoichiometry on the pseudo-(1 × 3) surface with a flux ratio of about 1.2.

Chapter 3

High Resolution X-Ray Diffraction (HRXRD)

HRXRD differs from X-Ray Diffraction (XRD) in the precision of the angular positions of the sample and detector, as well as the mono-energetic and mono-directional incident x-ray beam. It is a powerful, non-destructive, *ex situ* method that reveals information such as layer thickness (i.e. growth rate), alloy composition, crystalline and interface quality, and strain [50, 51, 52, 53, 54].

Fig. 3.1 shows the experimental arrangement for a diffraction experiment. The angle ω defines the incident angle of the x-ray beam with respect to the sample surface, and 2θ is the angular position of the detector with respect to the incident beam: $2\theta = 0$ corresponds to a detector position directly across from the x-ray source. To align the sample and to allow for a wide variety of diffraction planes, the sample can also be adjusted by the angles (not shown) φ (rotation of the sample about the y-axis in Figure 3.1) and ψ (rotation of the sample about the x-axis in Figure 3.1).

All the HRXRD work discussed herein utilized a Philips HR-2 High Resolution Diffractometer with a four reflection Ge(220) incident beam monochrometer and an incident beam power of 1200W, corresponding to an unobstructed beam-to-detector ($\omega = 2\theta = 0$) count rate of about 600,000counts/second (cps), and a minimum

FWHM resolution of 14 arcsec. All the scans and sample alignment were controlled using Philips PC-MRD Software, version 1.2. The minimum step size for ω and 2θ are 0.00025° and 0.001°, respectively. The incident x-ray wavelength is $\lambda = 1.54059\text{Å}$ corresponding to the Cu$K\alpha_1$ transition [55]. The detector without a slit will allow all radiation within a window width of $\Delta 2\theta = 2°$ to pass. Since this results in the unwanted blurring of closely spaced peaks during some scans (Sec. 3.2), slits are available to lower the angular detector width down to a minimum of $\Delta 2\theta = 0.14°$.

Dynamic simulations [51, 56, 57, 58] of the measured structures were carried out using Philips PC-HRS Simulation Software, version 1.30. Dynamic simulations take into account such factors as the extinction of the beam as a function of depth in the sample[1], absorption, and multiple reflections. The simulation accounts for only strained structures, so alternate means of interpreting relaxed structures are discussed below.

Since I have yet to find a satisfactory reference on HRXRD, this chapter will discuss representative data obtained with our system, but will focus on the theory of diffraction, procedure for obtaining specific information, and the analysis of data.

3.1 Condition for Constructive Interference

For the case of elastic scattering, in which light or particles of wavelength λ are incident upon a set of planes of spacing d_{hkl}, the angle of incidence[2], θ, for maximum constructive interference is given by the solution of Bragg's Law [21, 60, 51]:

$$2d_{hkl}\sin\theta = n\lambda, \tag{3.1}$$

[1] The extinction length for most semiconductors is on the order of about 10μm. For the case of no absorption, a penetration into the crystal equal to twice the extinction length results in reflection of 93% of the radiation [59].

[2] Since ω defines the angle of the incident x-ray beam with respect to the sample surface, $\theta = \omega$ only for diffraction using planes parallel to the sample surface.

where n is an integer and denotes the diffraction order. An equivalent representation for Bragg's law can be developed for reciprocal space [21]. If a, b, and c are the fundamental lattice vectors in real space, then the fundamental lattice vectors in reciprocal space are given by:

$$\mathbf{A} = 2\pi \frac{\mathbf{b} \times \mathbf{c}}{\mathbf{a} \cdot (\mathbf{b} \times \mathbf{c})}, \tag{3.2}$$

$$\mathbf{B} = 2\pi \frac{\mathbf{c} \times \mathbf{a}}{\mathbf{a} \cdot (\mathbf{b} \times \mathbf{c})}, \tag{3.3}$$

$$\mathbf{C} = 2\pi \frac{\mathbf{a} \times \mathbf{b}}{\mathbf{a} \cdot (\mathbf{b} \times \mathbf{c})}, \tag{3.4}$$

and constructive interference occurs when the Laue condition is satisfied:

$$\mathbf{k_s} - \mathbf{k_i} = h\mathbf{A} + k\mathbf{B} + l\mathbf{C} \equiv \mathbf{G_{hkl}}, \tag{3.5}$$

where $\mathbf{k_i}$ and $\mathbf{k_s}$ are the incident and scattered vectors defined in Figure 3.1, where $|\mathbf{k}| \equiv 2\pi/\lambda$, and $\mathbf{G_{hkl}}$ is a reciprocal lattice vector. For elastic scattering, $|\mathbf{k_i}| = |\mathbf{k_s}|$, and:

$$\mathbf{k_i} \cdot \mathbf{G_{hkl}} = -\frac{1}{2} |\mathbf{G_{hkl}}|^2 . \tag{3.6}$$

The radius of the "Ewald sphere" is then given by $|\mathbf{k_i}|$ $(=|\mathbf{k_s}|)$. Hence, Equation 3.5 indicates that if the Ewald sphere intersects two points in reciprocal space separated by $\mathbf{G_{hkl}}$, diffraction is possible from the (hkl) set of planes and the corresponding angle of incidence is given by the solution of Equation 3.6. Alternatively, in the geometry of Figure 3.2, constructive interference will occur whenever the tip of the $\mathbf{k_s}$ vector overlaps a reciprocal lattice point.

Figure 3.2 shows a representation of reciprocal space along with the Ewald sphere. For clarity, the points representing only one layer are included. For each additional layer, an additional lattice is added, as in Figure 3.4. For a given x-ray experiment, $\mathbf{k_i}$, which determines the radius of both the Ewald sphere and therefore the large

semi-circle, and beam power are kept constant, and the Laue condition is met by altering ω (incident angle) and/or 2θ (detector angle), which are defined in Fig. 3.1. In our system, a detector position of $2\theta = 180°$ is not possible since this would require an overlap between the detector and x-ray generator. As a result, the maximum angular position for our detector is $2\theta = 160°$.

3.2 Types of HRXRD Scans

For an actual crystal, the reciprocal lattice points have a non-zero size due to thermal vibrations, lattice imperfections, and the finite thickness of the layer. Therefore, the Laue condition (Eq. 3.5) can be satisfied over a relatively large area surrounding each of the reciprocal lattice points. In order to probe these points, a number of different types of scans are available.

As seen from Fig. 3.2, a scan in which 2θ is fixed and ω is swept (ω scan), or "rocked", through a prescribed range amounts to "rolling" the Ewald sphere about the origin, and therefore sweeps the tip of the $\mathbf{k_s}$ vector through an arc of constant radius in reciprocal space. Conversely, if ω is swept through a prescribed angle and 2θ is rotated twice as fast in the same direction ($\omega - 2\theta$ scan), this amounts to a scan that sweeps the tip of the $\mathbf{k_s}$ vector radially from the origin in reciprocal space. The two scan directions are perpendicular to each other, and therefore ω and $\omega - 2\theta$ scans play the roles in polar coordinates of ϕ and ρ, respectively.

3.2.1 ω Scan (Rocking Curve)

An ω scan is predominantly performed for calibration of the apparatus, to determine alloy composition, and to evaluate sample quality by observing the shape and measuring the full width at half maximum (FWHM) of the resultant peak [51]. However,

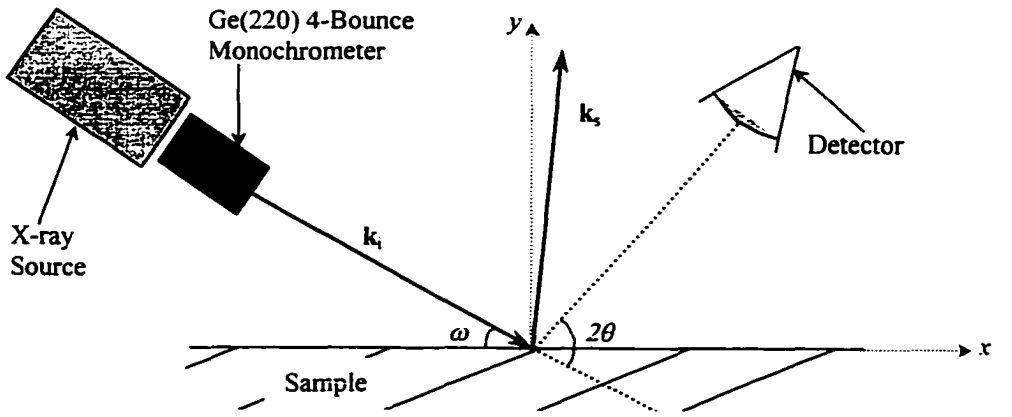

Figure 3.1: Experimental set-up for x-ray diffraction. The x-rays are sent through a monochrometer before impinging on the sample. $\mathbf{k_i}$ is a constant for a given experiment, but ω and 2θ can be varied. The sample can also by rotated about the x-axis (ψ) and y-axis (ϕ).

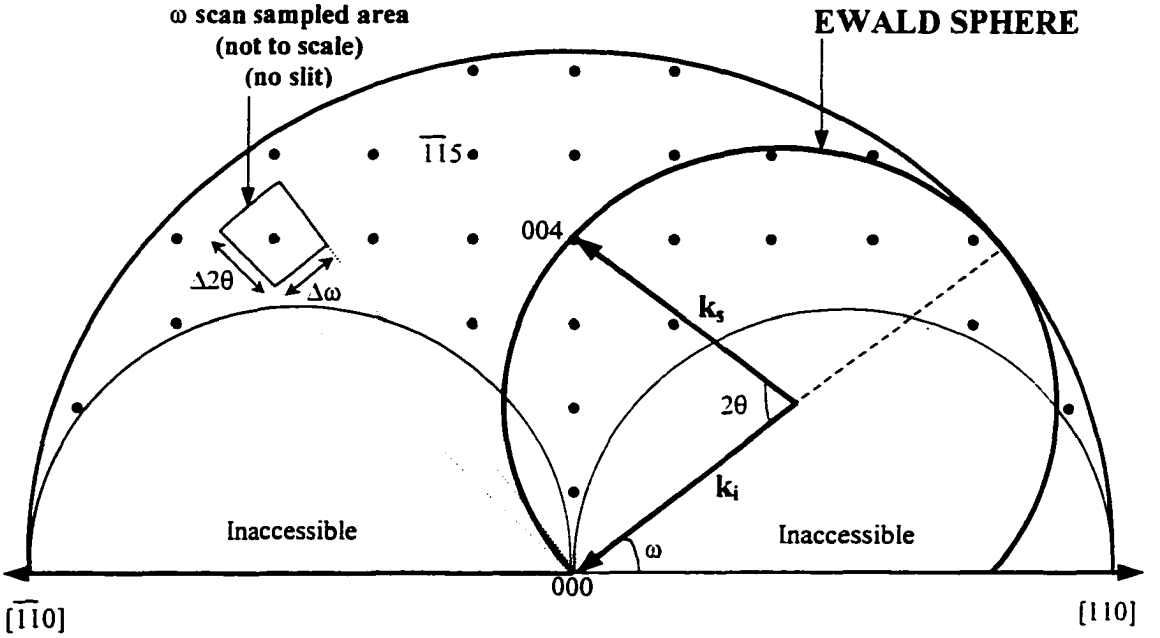

Figure 3.2: Reciprocal space map, using the Ewald construction, of the accessible points in the reciprocal lattice. The incident and scattered beams are denoted as $\mathbf{k_i}$ and $\mathbf{k_s}$, respectively. The large semi-circle is limited by the energy of the incident x-ray beam, and the inaccessible regions correspond to an incident angle of $-180 < \omega < 0°$ and a scattered angle of $-180 < 2\theta < 0°$. Constructive interference will occur when the tip of the $\mathbf{k_s}$ vector overlaps a reciprocal lattice point.

caution is required in the interpretation of the FWHM. First, since the peak becomes more δ−function like as more layers contribute to the diffraction, the FWHM value should be quoted only in conjunction with the layer thickness [60]. Second, an ω scan represents only a pseudo one-dimensional cross section of the actual profile (i.e. along an arc of constant radius) of the reciprocal lattice point being scanned. A more complete evaluation of a diffraction peak can be obtained by performing an area scan (Sec. 3.2.4).

Due to the non-zero reciprocal lattice point size, an ω scan with a detector window allowing only a small angular range, which would probe only a small "stripe" in reciprocal space, would likely miss the region of the "point" corresponding to the maximum signal. As a result, a false FWHM would be detected and a false angular peak position, ω, would be measured, leading to a false determination of, say, alloy concentration. To avoid this, rocking curves are performed without a detector slit in order to collect all of the radiation scattered by the sample for a given value of ω.[3] This is tantamount to the sweeping through a "stripe" in reciprocal space of radial width $\Delta 2\theta \approx 2^o$, as shown in Fig. 3.2.

As discussed in Chapters 5 and 6, accurate determination of x in an $Al_xIn_{1-x}Sb$ layer is of utmost importance for our material system since the amount of Al in the barrier affects the barrier height and the strain and therefore the number and energy of the quantized levels in the well (Sec. 1.4). Aluminum concentration can be initially calibrated using the technique of RHEED oscillations (Sec. 2.3.2). However, conditions may change between calibrations, and HRXRD offers an *ex situ* means of determining the actual Al concentration in a sample.

[3]This will occur if the system is at least nearly relaxed (Sec. 3.2.4), the system is calibrated, and the radial spread in the reciprocal lattice point(s) is (are) less than 2^o, since the $\mathbf{k_s}$ vector in Fig. 3.2 spans $\Delta 2\theta = 2^o$ in the absence of an entry slit on the detector.

Figures 3.3a and 3.3b are typical ω scans showing reflected intensity as a function of (arbitrary) angle of incidence of the (004) and ($\bar{1}$ $\bar{1}$ 5) planes, respectively. The left and right peaks correspond to the InSb and $Al_xIn_{1-x}Sb$ layers, respectively, shown schematically in Figure 3.3c; the peaks corresponding to the AlSb layer and the GaAs substrate are not shown. A reciprocal space map of the ($\bar{1}$ $\bar{1}$ 5) planes indicates that each layer in the structure is completely relaxed (Sec. 3.2.4), and therefore a simulation of the structure cannot be performed with our simulation software. Instead, the alloy concentration can be obtained by an ω scan since the separation of the peaks is $\ll 2^o$.

To determine x, both peaks are first shifted by an amount:

$$\Delta\omega = \omega_{InSb,known} - \omega_{InSb,meas}, \tag{3.7}$$

where $\omega_{InSb,known}$ is the calculated value obtained by the solution of Equation 3.1 using the known lattice constant of InSb, and $\omega_{InSb,meas}$ is the measured angular position of the InSb peak. The spacing of the planes, d, is then given by:

$$d = \frac{\lambda}{2\sin(\omega_{AlInSb,meas} + \Delta\omega)}, \tag{3.8}$$

where $\omega_{AlInSb,meas}$ is the measured peak position corresponding to the alloy. For diffraction using the (00l) planes (i.e. planes parallel to the surface), the lattice constant of the alloy, a_{alloy}, is given by:

$$a_{alloy} = l \times d. \tag{3.9}$$

The alloy concentration can also be obtained by the solution of Vegard's Law:

$$a_{alloy} = a_{InSb} \times (1 - x) + a_{AlSb} \times (x), \tag{3.10}$$

where a_{InSb} and a_{AlSb} are the known lattice constants of InSb and AlSb, respectively.

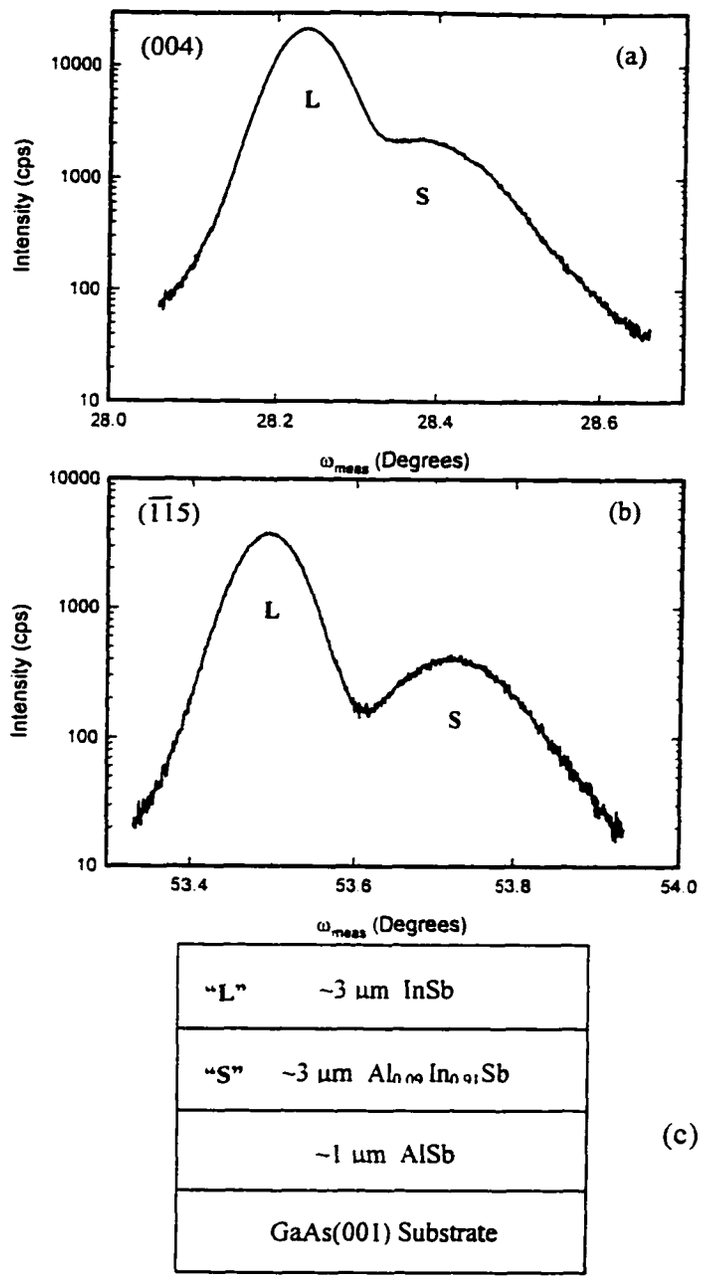

Figure 3.3: Examples of HRXRD ω scans using (a) (004) and (b) $(\bar{1}\ \bar{1}\ 5)$ reflections of the structure shown in (c) (S516). The left and right peaks correspond to InSb and $Al_xIn_{1-x}Sb$ layers, respectively.

Since ω denotes the angle between the incident beam and the sample surface, diffraction using planes that are not parallel to the substrate surface (asymmetric planes) requires that Equations 3.9 and 3.10 be modified. Assuming no tilt exists between the layers (which was verified using an area scan of the (004) planes (Sec. 3.2.4)), and since we have a completely relaxed structure, we can calculate the angle between the (115) planes and the substrate surface, $\Delta\omega_{asym}$, using vector notation:

$$\Delta\omega_{asym} = \arccos\left(\frac{[-1,-1,5]\cdot[0,0,4]}{|\,[-1,-1,5]\,||\,[0,0,4]\,|}\right) = 15.79317^{o}. \qquad (3.11)$$

which is added in the sine term in Equation 3.8.

Three additional asymmetric scans corresponding to the $(\bar{1}\,\bar{1}\,5)$, $(1\,\bar{1}\,5)$, and $(\bar{1}\,1\,5)$ planes were obtained (not shown), giving the lattice constants listed in Table 3.1, along with the calculated Al concentration, x. Since tilt has been ruled out, a large disparity in lattice constant between these four scans would indicate an asymmetric distortion of the unit cell [60].

Also listed in Table 3.1 are the parameters calculated for the scan shown in Fig. 3.3 and three additional (004) scans (not shown) corresponding to sample rotations of $\phi = 90^{o}, 180^{o}$, and 270^{o}. The calculated lattice constant is again nearly equal between the four scans. Using Equation 3.10 (modified for the (115) scans), an alloy composition can be obtained for each of the eight scans. The average alloy compositions of the (| 1 || 1 | 5) and (004) scans are calculated to be 8.69% and 9.08%, respectively, which agrees well with the attempted alloy concentration of 9%.

The minor discrepancy in the calculation between the two sets of planes is possibly due to the InSb layer being slightly strained, but is likely due to the width of the peaks, which makes determination of the maxima difficult. Since all of the layers are relaxed, one would expect a large number of defects to be present throughout the

structure, which is manifested by a broad HRXRD profile. In addition, extinction effects result in the alloy peak being much less intense than the InSb peak, further hampering the determination of peak location. The alloy peak could be made stronger by growing a thinner InSb layer, but this has resulted in a structure in which the InSb layer was not completely relaxed.

3.2.2 $\omega - 2\theta$ Scan

The $\omega - 2\theta$ scan is defined by the relation:

$$\frac{d(2\theta)}{dt} \equiv 2\frac{d\omega}{dt} \tag{3.12}$$

for all scans. In general,

$$2\theta \neq 2 \times \omega. \tag{3.13}$$

However, for scans using the [00l] planes, $2\theta = 2 \times \omega$.

The $\omega - 2\theta$ scan is used in like fashion to the rocking curve, but is used to scan peaks that are separated by more than $2\theta = 2^o$, and, with the use of a detector entrance slit, can provide resolution of closely spaced peaks. The utility of this, for example, arises from the fact that the knowledge of the separation between an alloy peak and, say, the known substrate peak allows for the calculation of the alloy composition (Sec. 3.2.1). An $\omega - 2\theta$ scan is technically not a rocking curve since the detector is moving, but can be used if the structure is relaxed and the reciprocal lattice points are small compared to $\Delta 2\theta$. The width of the peak obtained from this measurement will provide information about the width of the reciprocal lattice point in a direction radial to the origin in reciprocal space, as opposed to information about the circumferential width obtained from a rocking curve.

An $\omega - 2\theta$ scan can be used with a slit to determine alloy concentration only if the HRXRD apparatus is properly calibrated (Sec. 3.2.3) and all of the reciprocal

lattice point maxima fall on a line that passes through the origin. This alignment of points is generally not the case (Sec. 3.2.4), so a slit should typically be avoided. However, a slit is usually required to resolve peaks in which the spacing of the peak maxima is smaller than half the FWHM of one of the peaks. The smallest available slit for our system allows radiation within a $\Delta 2\theta = 0.14^o$ range, so this technique is effective for peaks separated by less than $\Delta 2\theta = 0.14^o$ only if the FWHM of the individual peaks are less than, in general, (*peak spacing/2*).

The $\omega - 2\theta$ scan using a detector entry slit is useful in performing reciprocal space maps, as discussed in (Sec. 3.2.4).

3.2.3 2θ Scan/Calibration Procedure

As discussed in the previous section, the smallest detector slit in our system is $\Delta 2\theta = 0.14^o$, so every 2θ scan in which the detector intercepts scattered radiation consists of a plateau with FWHM$\geq 0.14^o$, depending on the slit, where the only variation between scans for a given slit is in the measured intensity. As a result, the 2θ scan is not useful insofar as garnering information about the sample, but is useful in our apparatus as a means of calibrating the system.

To calibrate the system, an ω scan is performed on a peak (usually the substrate or a Si wafer provided with the system for the purpose of calibration) whose angle of diffraction is "known" by the solution of Equation 3.1. Following the initial scan, the sample is "parked" at the ω corresponding to the maximum measured intensity. A 2θ scan is then performed without a slit on the detector, and the measured intensity as a function of 2θ is a plateau that is in this case 2^o wide. The detector is then "parked" on the middle of this plateau, and the process is repeated, each time using a smaller slit on the detector. This procedure "nudges" the tip of the $\mathbf{k_s}$ vector onto

the maximum of the reciprocal lattice point. When the smallest slit has been used repeatedly without a necessary change in either ω or 2θ, the system is calibrated.

3.2.4 Area Scan (Reciprocal Space Map)

In the absence of a detector slit, both the ω and the $\omega - 2\theta$ scans discussed above measure the cumulative diffraction intensity originating from a relatively large region in reciprocal space. As discussed in Sec. 3.2, the quality and thickness of the sample have a direct bearing on how "point-like" the reciprocal lattice points appear. Moreover, information can be obtained relating to the type of imperfection occurring in a particular layer. Table 3.2 [61] lists some defects and the direction of the associated reciprocal lattice point broadening. The rocking curve and $\omega - 2\theta$ scan give information on the point size from the determination of the FWHM, but these measurements are only a one-dimensional cross-section of the actual profile. Area scans (reciprocal space maps) allow us to probe the full size and shape of the reciprocal lattice points.

In addition, reciprocal space maps allow for a relatively easy determination of whether a layer is strained, partially strained, or relaxed. A completely strained layer has a lattice constant equivalent to that of the underlying layer in the plane parallel to the substrate[4]. As a result, for growth on a (001) oriented substrate, the reciprocal lattice points of a completely strained layer will be aligned along the [001] direction with the reciprocal lattice points of the underlying layer, as shown in Figure 3.4a.

Conversely, a fully relaxed layer has no distortion of the reciprocal lattice. Since, for our structures, the sub-layer and epilayer have the same Bravais lattice, the

[4]This strain will also cause a deformation of the reciprocal lattice perpendicular to the substrate as the lattice attempts to conserve volume.

Diffraction Planes	$\omega_{meas.AlInSb}$	$\omega_{meas.InSb}$	d	Average x
$(004), \phi = 0^o$	28.56900	28.42182	6.44875	
$(004), \phi = 90^o$	27.44940	27.29175	6.44658	
$(004), \phi = 180^o$	27.38336	27.24580	6.45074	
$(004), \phi = -90^o$	26.23664	26.07900	6.44659	0.0908
$(11\bar{5})$	22.57844	22.36312	4.96411	
$(\bar{1}1\bar{5})$	54.21503	53.98417	4.96241	
$(1\bar{1}\bar{5})$	21.44625	21.22240	4.96318	
$(\bar{1}1\bar{5})$	21.40732	21.19515	4.96445	0.0869

Table 3.1: Parameters for S516 determined from HRXRD

Cause of Broadening	Direction of Broadening
Finite Thickness of Layer	Normal to Interface
Lattice Parameter Change	Radial to Reciprocal Space Origin
Orientation Change (Tilt or Curvature)	Circumferential about Reciprocal Space Origin
Discontinuities Parallel to Interface (Islands or Grain Boundaries)	Parallel to Interface

Table 3.2: Crystal imperfections and associated direction of reciprocal lattice point broadening.

two unit cells in the different materials will have an identical aspect ratio, and the reciprocal lattice points will therefore be aligned radially from the origin in reciprocal space, as shown in Figure 3.4b. Finally, the lattice points of a partially relaxed epilayer will be at a position intermediate between being radially and vertically aligned with the lattice points of the straining layer.

Since the (00l) reciprocal lattice points (i.e. planes parallel to the substrate surface) lie along a line that is parallel to the [001] direction and also passes through the origin, these reflections cannot be used to determine the degree of strain in a layer. However, tilt between layers results in a relative rotation in reciprocal space between the layers, which can be observed unambiguously by obtaining a reciprocal space map of the (00l) reciprocal lattice points of the relevant layers.

An area scan is achieved by a series (usually > 10) of $\omega - 2\theta$ scans (Sec. 3.2.2). In each scan, the range over which 2θ is swept remains the same, but the starting value for ω is adjusted by some small value, $\delta\omega$, for each scan. If a detector slit is used, each scan collects radiation from a "strip" in reciprocal space that is radial to the origin. The shift of ω results in the measured strip being rotated by $\delta\omega$ relative to the previous scan. A scan of the entire point requires that the range of 2θ be greater than the radial width of the reciprocal lattice point(s), and that $\delta\omega \times$ *number of scans* has a greater arc-length than the point(s) being scanned. A contour plot is then obtained of the intensity with axes representing directions in reciprocal space, thus giving a profile of the reciprocal lattice points.

Figure 3.5a shows a plot of an area scan of the ($\overline{1}\overline{1}5$) planes of S516, discussed in Section 3.2.1, showing all the ($\overline{1}\overline{1}5$) reciprocal lattice points for each of the four layers. Figure 3.5b is an enlargement of the InSb and $Al_xIn_{1-x}Sb$ points. The nearly parallel lines on either side of the peaks pass through the origin in reciprocal space.

and are used as a guide to the eye in determining whether the maxima of the points fall on a line that also pass through the origin, as in Figure 3.4a. Since it appears this criterion is met, we conclude that the structure is relaxed[5].

3.3 InSb/$Al_xIn_{1-x}Sb$ Strained Layer Superlattices (SLS) on InSb Substrates

Abrupt interfaces are required for many device structures. To characterize interfacial quality, an $Al_xIn_{1-x}Sb$/InSb superlattice was grown on an InSb substrate with a 3μm-thick InSb buffer. The HRXRD data (solid line) is shown in Figure 3.6a for the superlattice structure shown in Figure 3.6b. The $\omega - 2\theta$ scan reveals a large number of sharp satellite peaks ($m = 1, 2$, etc.) on either side of the central peak ($m = 0$). The prominent peak at $\omega = 28.394^o$ is due to the InSb substrate and buffer layer. From the separation between the satellite peaks and from the location of the central peak, we deduce a period of 364Å and an alloy composition of 12.7%, respectively. A HRXRD reciprocal space map of the $(\bar{1}\ \bar{1}\ 5)$ reciprocal lattice points verifies that the superlattice barriers are strained to the lattice constant of the InSb substrate.

Once the HRXRD scan is obtained, a simulation is performed which gives both quantitative information, such as alloy concentration and individual layer thickness, and qualitative information, such as quality of interfaces and number of defects.

Strain in a layer alters the lattice constant in the planes parallel and perpendicular to the substrate [60]. The $m = 0$ satellite peak is assumed to occur at the angle.

[5]This method of determining the degree of relaxation is largely subjective due to the lack of resolution with our system; increased resolution could be obtained with the addition of a monochrometer on the detector. Further evidence for relaxation comes from the scans discussed in Section 3.2.1. If the alloy concentration deduced from the (004) is the same as that deduced from the (115) data, then the structure is relaxed. Our calculated Al concentration differed slightly between the two types of scans (9.08% vs. 8.69%), but we believe this is due to the difficulty in determining the angular location of the peaks, as discussed in Section 3.2.1.

$\theta_{m=0}$, corresponding to the average lattice constant, a_{ave}, of the superlattice in the [001] direction [51]. This value is obtained experimentally using Equation 3.1:

$$a_{ave} = \frac{\lambda}{(1/4)2\sin\theta_{m=0}}, \tag{3.14}$$

where the factor (1/4) arises from the fact that we're using the (004) reflection planes. In the present case, a_{ave} is the weighted average of the lattice constants in the unstrained InSb and strained $Al_xIn_{1-x}Sb$ layer, respectively, and therefore gives little direct information about the alloy concentration. However, a_{ave} can be related to the unstrained lattice constant of InSb, $a_{0,InSb}$, and the known strained lattice constant in the [001] direction in the alloy, a_{AlInSb},

$$a_{ave} = a_{0,InSb}\left(\frac{d_{InSb}}{d}\right) + a_{AlInSb}\left(\frac{d_{AlInSb}}{d}\right), \tag{3.15}$$

where d_{InSb} and d_{AlInSb} are the actual (average) thicknesses of the InSb and $Al_xIn_{1-x}Sb$ layers, respectively. The superlattice period, d, is then:

$$d = d_{InSb} + d_{AlInSb} \tag{3.16}$$

and can be experimentally obtained from the angular difference in position of the superlattice satellite peaks [51]. From Equation 3.1, we know that $2\sin\theta_m/\lambda = m/d$. where m is an integer and θ_m is the angular position of the satellite peak of order m. If this function is plotted, the slope is given by $1/d$. and:

$$d = \frac{\lambda\Delta m}{2\Delta\sin\theta}. \tag{3.17}$$

For the samples discussed here, each layer was intended to have a thickness of $d/2$. Using $d_{InSb} = d_{AlInSb} = d/2$ in the simulation provides for a good fit of the simulation to the data if the actual deviation from $d/2$ is not large [50]. However, HRXRD

provides sufficient information to input the individual layer thicknesses into the simulation self-consistently, and therefore allows for an independent determination of the growth rate.

The unstrained lattice constant in the alloy, $a_{0,AlInSb}$, rather than a_{AlInSb}, allows for the determination of the Al concentration. These two values are related to each other by [60]:

$$a_{0,AlInSb} = \left(\frac{C_{11,AlInSb}}{C_{11,AlInSb} + 2C_{12,AlInSb}} \right) (a_{AlInSb} - a_{0,InSb}) + a_{0,InSb}, \tag{3.18}$$

where $C_{11,AlInSb}$ and $C_{12,AlInSb}$ are the stiffness coefficients of the alloy parallel to and perpendicular to the substrate plane, respectively, and determine the amount of deformation introduced when the material is strained. These experimentally determined values are listed in Reference [62][6]. For the case of $Al_xIn_{1-x}Sb$:

$$C_{11(12),AlInSb} = C_{11(12),AlSb} \times (x) + C_{11(12),InSb} \times (1 - x), \tag{3.19}$$

which is calculated for a given value of x and substituted into Equation 3.18.

Finally, the average alloy composition, x, can be obtained by the solution of Vegard's law[7]:

$$a_{0,AlInSb} = a_{0,AlSb} \times (x) + a_{0,InSb} \times (1 - x) \tag{3.20}$$

or,

$$x = \left(\frac{a_{0,AlInSb} - a_{0,InSb}}{a_{0,AlSb} - a_{0,InSb}} \right). \tag{3.21}$$

The value of $a_{0,InSb}$ is given in Table 1.1. Equations 3.17 and 3.14 provide the two experimentally known values of d and a_{ave}, respectively, leaving the five unknown variables of a_{AlInSb}, $a_{0,AlInSb}$, d_{InSb}, d_{AlInSb}, and x, and four Equations:

[6]Since a range of values is listed for the constants, intermediate values in the cited range were chosen: $C_{11,InSb} = .6592$, $C_{12,InSb} = .3563$, and $C_{11,AlSb} = .8769$, $C_{12,AlSb} = .4341$.

[7]Vegard's law is obeyed fairly closely for most alloy systems [51].

3.15, 3.16, 3.18, and 3.21, leaving one unknown as a parameter. Therefore, a simple computer program can be written that will self-consistently provide four of the unknowns when the fifth, say x, is assumed. The "guessed" value of x is then entered into the simulation software along with the calculated values of d_{InSb} and d_{AlInSb}. After the simulation is run, a new x is "guessed" until the best simulated fit is observed.

The simulation is shown in Figure 3.6a (dashed line), and shows very good agreement with our data. The narrow peak widths indicate that the superlattice has interfaces of very high quality.

In conclusion, HRXRD of SLS structures and the associated simulation provides not only Al alloy concentration, x, but also an independent measure of the growth rate under actual sample conditions as opposed to the growth rate procedure outlined in Section 2.3.2.

3.4 InSb/$Al_xIn_{1-x}Sb$ SLS on GaAs Substrates

Growth on semi-insulating GaAs substrates is desirable in order to minimize parallel conduction paths at room temperature, as well as to allow for potential integration with GaAs devices. Figure 3.7a shows the results of a HRXRD $\omega - 2\theta$ scan (solid line) of an $Al_xIn_{1-x}Sb$/InSb superlattice grown on a GaAs substrate, which is shown in Figure 3.7b. GaSb, AlSb, and $Al_{2x}In_{1-2x}Sb$ buffer layers were inserted to help alleviate the effects of the 14.6% lattice mismatch between InSb and GaAs. The series of peaks between $\omega = 27.5^o - 29^o$ arise from the superlattice and adjacent $Al_xIn_{1-x}Sb$ buffer layer. From the location of the central peak ($m = 0$), we calculate the average lattice parameter of the superlattice and thereby determine an aluminum alloy composition of 14.5%. We observe several satellite peaks ($m = -2, -1, 0, 1, 2,$

etc.); the $m = +1$ satellite peak is obscured by the dominant peak at $\omega = 28.549°$, which is attributed to the $Al_xIn_{1-x}Sb$ buffer layer. From the spacing between satellite peaks, we deduce a superlattice period of 340Å. A HRXRD reciprocal space map of the reflections indicates that the superlattice structure is strained to the lattice constant of the $Al_xIn_{1-x}Sb$ buffer layer.

The equations in Section 3.3 used to determine the values that are input into the PC-HRS Simulation Software can be used, with slight modification, for a SLS grown on a relaxed $Al_xIn_{1-x}Sb$ "virtual substrate" epilayer which is grown on a GaAs substrate, as shown in Figure 3.7. However, as x is changed in the simulation, the lattice constant of the virtual substrate also changes, leaving four parameters that must be adjusted in the simulation instead of three.

In this case, it is the InSb layer that is strained instead of the $Al_xIn_{1-x}Sb$ layer. Therefore, all of the "AlInSb" subscripts in Equations 3.15–3.18 should be changed to "InSb", and vice versa. The stiffness coefficients in Equation 3.18 are now simply the stiffness coefficients of InSb, and Equation 3.19 is no longer needed. Equation 3.21 remains the same, and the experimentally determined values of a_{ave} and d are still given by Equations 3.14 and 3.17. The five unknown variables are now a_{InSb}, $a_{0.AlInSb}$, d_{InSb}, d_{AlInSb}, and x, where a_{InSb} is the strained lattice constant of the InSb layer in the [001] direction.

The dashed line in Figure 3.7a shows the simulated data. As discussed above, the simulation software only allows for strained layers, so we performed the simulation defining the 3μm $Al_xIn_{1-x}Sb$ layer as the substrate. As a result, the broad peak, which arises from the 1μm $Al_{2x}In_{1-2x}Sb$ layer and which washes out the $m = +5$ and $+7$ satellite peaks, is not modeled. The widths of the satellite peaks we observe here are larger than for the superlattice grown on InSb, indicating lower interface

and/or crystalline quality. A large defect density is expected from the large lattice mismatch between the substrate and the superlattice. We hope to reduce the defect density through ongoing attempts to optimize buffer layer composition and growth procedures.

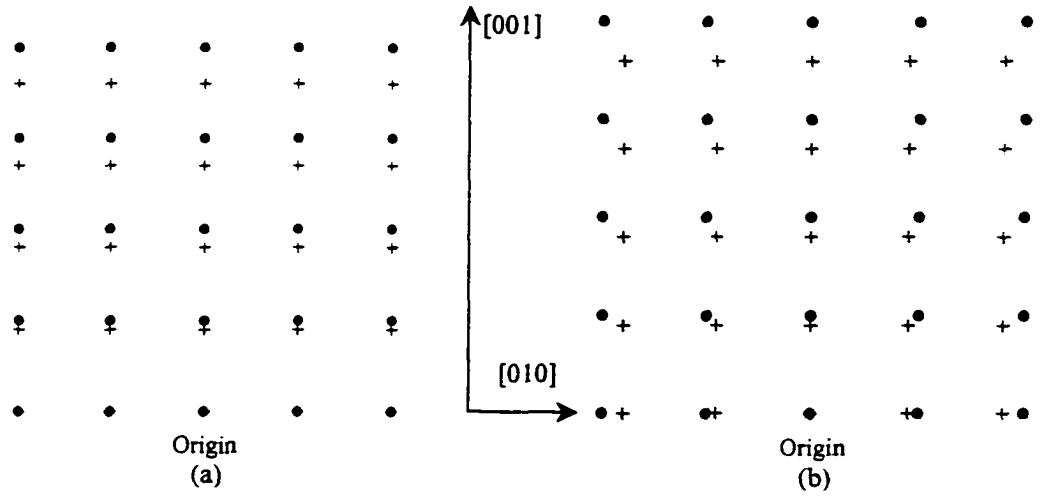

Figure 3.4: Representation of reciprocal lattice points for an underlying layer (solid, small lattice constant) and epilayer (crosshair, large lattice constant) for the case where the epilayer is (a) strained and (b) totally relaxed.

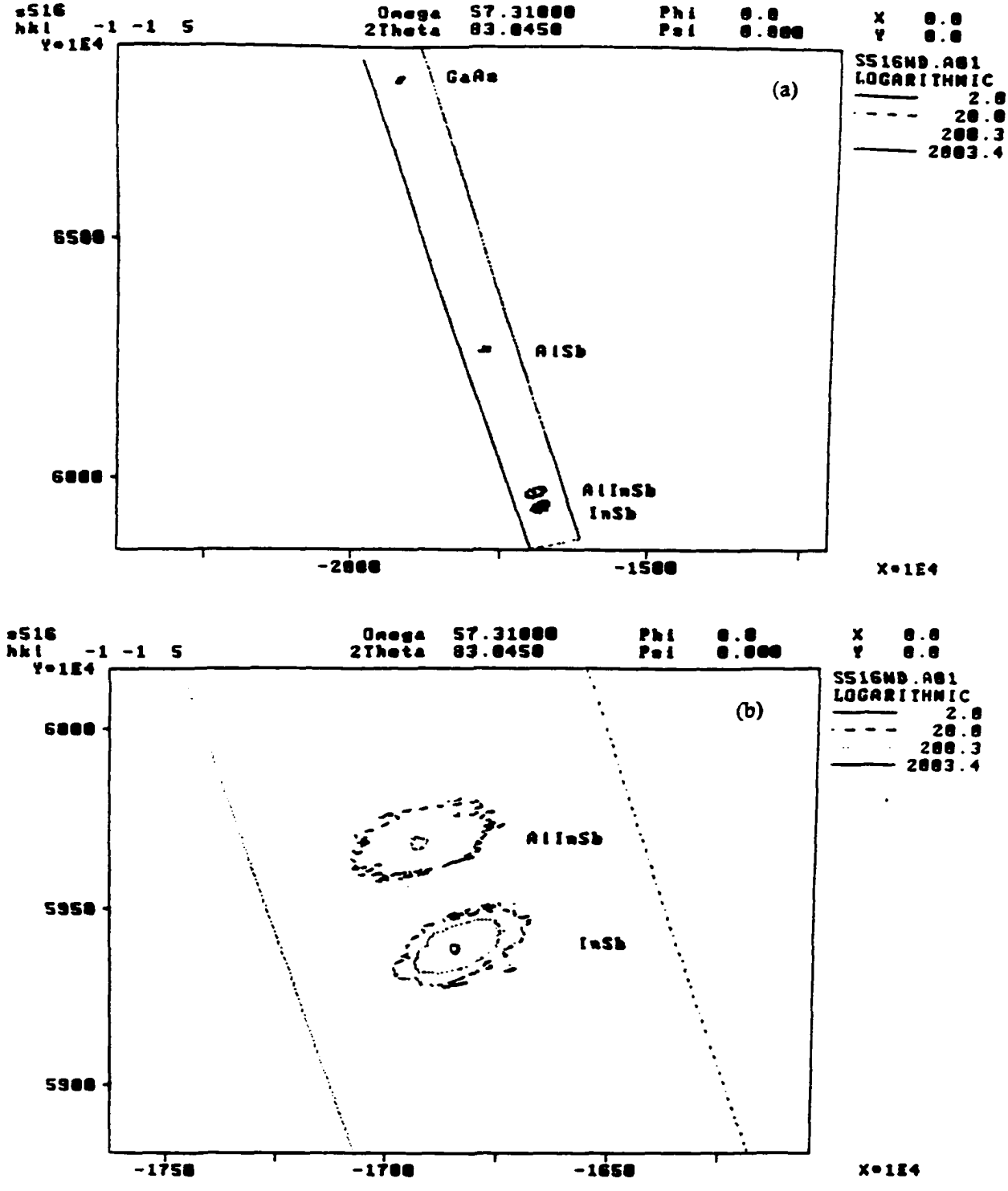

Figure 3.5: (a) HRXRD reciprocal space map of S516 shown schematically in Figure 3.3. (b) Enlargement of the $Al_xIn_{1-x}Sb$ and InSb points. The peak maxima appear to fall on a line that passes through the origin, indicating all layers are relaxed.

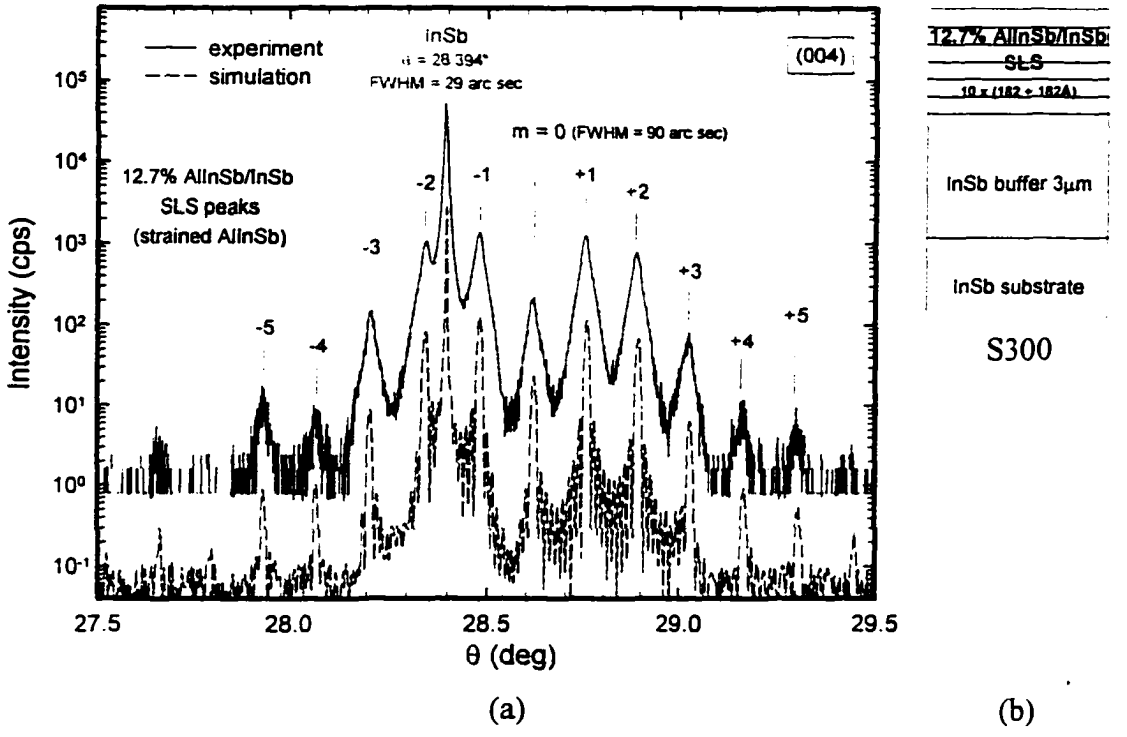

Figure 3.6: (a) (004) HRXRD $\omega - 2\theta$ scan (solid) and simulation (dashed) for a 10 Period $Al_xIn_{1-x}Sb$/InSb SLS grown on an InSb substrate. An Al alloy concentration of 12.7% was obtained from the simulation. FWHM=90arcsec for the $m = 0$ peak. and FWHM=27arcsec for the InSb peak. (b) Structure of the $Al_xIn_{1-x}Sb$/InSb SLS sample.

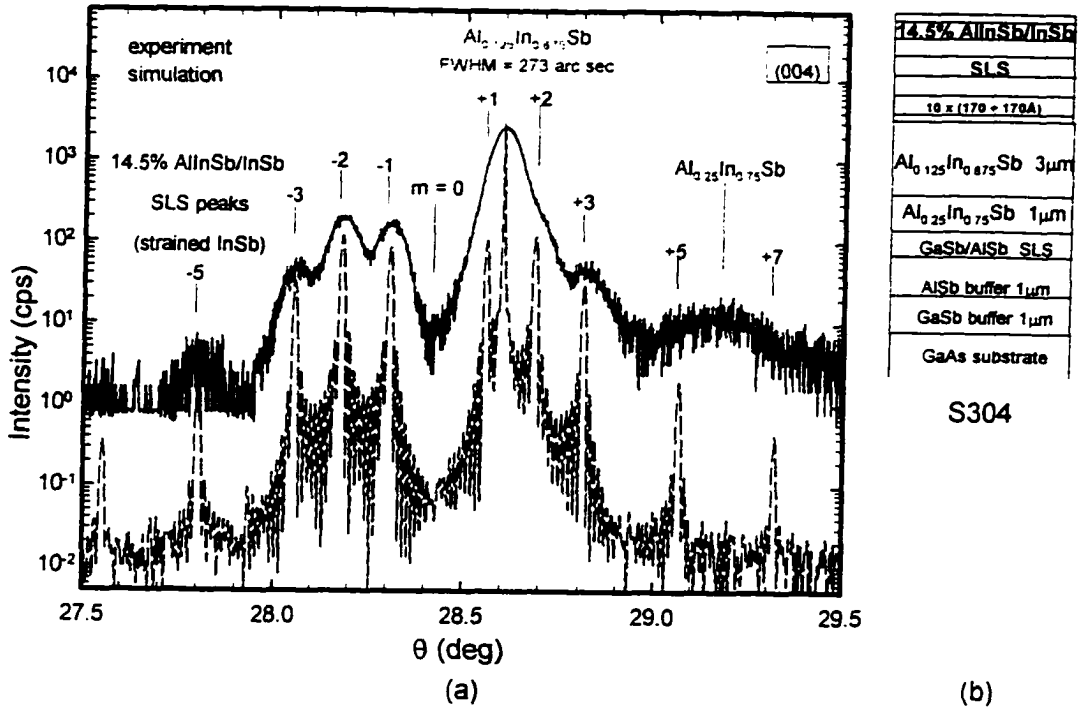

Figure 3.7: (a) (004) HRXRD $\omega - 2\theta$ scan (solid) and simulation (dashed) for a 10 Period $Al_xIn_{1-x}Sb$/InSb SLS grown on a GaAs substrate. An Al alloy concentration of 14.5% was obtained from the simulation. FWHM=274arcsec for the $Al_{0.125}In_{0.875}Sb$ peak. The broad peak obscuring the $m = +5$ and $+7$ satellite peaks was not modeled. (b) Structure of the $Al_xIn_{1-x}Sb$/InSb SLS sample

Chapter 4

Si δ-Doping of InSb and $Al_xIn_{1-x}Sb$

4.1 Introduction

InSb has the narrowest bandgap, the smallest effective mass, and the highest intrinsic electron mobility of all binary III-V semiconductors. These characteristics make InSb an attractive material for industrial applications, such as infrared devices [1, 2, 3], high-speed field-effect transistors [4], and magnetoresistive sensors [5], as well as for the study of electrons in semiconductors. Moreover, the incorporation of a barrier material, such as $Al_xIn_{1-x}Sb$, in heterostructures fabricated by MBE, can lead to improved device performance [1] and allows for the fabrication of InSb quantum wells [63, 11, 64]. The study of n-type doping in InSb is therefore motivated by the potential for producing high-mobility electrons for device applications (Chap. 5) as well as for the basic research of quantum transport in this material (Sec. 6.2).

An important step towards achieving such structures is to characterize dopant behavior. As discussed in Section 4.3.4, the dopant profile leading to the least amount of scattering for a remotely doped structure consists of the highest practical dopant density in the plane of growth [65]. Therefore, the ideal configuration for remotely

doped structures is to confine all of the dopant to a single atomic plane parallel to the conduction channel. If a dopant concentration profile as a function of depth into the sample were made for such a structure, it would resemble the delta-function: a spike at the dopant plane and zero everywhere else. From this, the name δ-doping was derived. In practice, however, it is difficult to confine the dopant atoms to a single plane due to such effects as (a) surface segregation/migration, (b) exceeding the solid solubility limit, (c) diffusion, and, (d) mutual Coulomb repulsion between ionized dopants [66]. Mechanisms (b) and (d) contribute to limit the density of dopant in a plane, and (a) and (c) become more significant at higher temperatures. Surface segregation/migration occurs in one of two ways. First, if an accumulation layer exists on the surface that is opposite in charge to the ionized dopant, a potential gradient exists, and the random diffusion process now has an extra component directed toward the surface. Second, if the dopant atoms have a lower energy on the solid surface than in the bulk, the atoms will "ride" along on the growth front.

Compared to group-VI [67, 68] and rare-earth [69, 70] atoms, the use of Si [71, 72, 73, 8, 74] as a donor in InSb is attractive due to its low vapor pressure and its successful use as a donor in GaAs [36, 66]. However, Si atoms (column-IV in the periodic table) can be either donors or acceptors in III-V materials, depending on whether they occupy group-III or group-V atomic sites. Uniform doping of InSb grown by MBE results in n-type conduction across a range of growth conditions [71]. However, for a given Si concentration, the electron concentration decreases with increasing growth temperature. Increased autocompensation at higher substrate temperatures is thought to be responsible for this behavior [71].

In this chapter, I discuss the results of secondary ion mass spectrometry (SIMS) and Hall effect experiments that demonstrate the effect of substrate temperature on

Si compensation in δ-doped InSb and $Al_xIn_{1-x}Sb$ [75]. These experiments indicate that the substrate temperature and surface reconstruction during growth of the cap layer, rather than at the time of doping, are primarily responsible for the observed carrier-density dependence on substrate temperature.

Additional parameters for the samples discussed in this chapter are presented in Appendix D, along with data for additional δ-doped samples.

4.2 Experiment

Substrate temperatures were calibrated through observation of the change in the static (Sb flux only) RHEED pattern upon crossing the transition temperature, T_{tr}. Below T_{tr} (≈ 380°C for InSb [76]), a c(4×4) surface reconstruction is observed from RHEED patterns. Above T_{tr}, an InSb surface has a pseudo-(1×3), hereafter denoted as '1×3' (Sec. 2.2.2), reconstruction while an $Al_xIn_{1-x}Sb$ surface has a (1×3) reconstruction. The surface reconstruction in $Al_{0.09}In_{0.91}Sb$ samples changes to '1×3' for a substrate temperature of $\approx T_{tr} + 20$°C. InSb (Sec. 4.3) and $Al_{0.09}In_{0.91}Sb$ (Sec. 4.4) buffer layers were grown on SI GaAs(001) substrates at a temperature of $T_{tr}+30\pm5$°C, and all InSb and $Al_{0.09}In_{0.91}Sb$ layers were grown with an Sb/group-III flux ratio slightly larger than unity and a nominal growth rate of 0.8ML/s. Doping was performed with an Sb overpressure to encourage Si incorporation in In sites and a Si effusion cell temperature of 1305°C. All samples except those discussed in Section 4.3.4 had a doping time of 50s. All the δ-doped samples were grown on GaAs substrates in order to minimize parallel conduction paths.

Hall effect measurements at magnetic fields up to 0.5T were performed on square samples with 4mm edges to determine carrier density using the van der Pauw geometry (Sec. 1.2.2). Electrical contact was made at each corner of a sample (See

Fig. 1.2), as discussed in Appendix A. Ohmic contact was checked through observation of linear current-voltage characteristics in four-point measurements. 77K measurements were obtained with liquid N_2, and variable temperature experiments were carried out using an APD Cryogenics HC-2D-1 Helium Compressor with a DE-202A Two-Stage Expander. Data were obtained via software originally written by the author and J. Winesett using LabWindows, version 2.1, and improvements to the software were made by the author, F. W. McKenna, N. M. Cunningham, and R. C. Meyer using LabView, version 4.0.1.

SIMS measurements were performed at Evans East using a 2 keV Cs+ bombardment of a Si-implanted GaSb standard at 60° incidence. Because a Si-implanted GaSb standard was used (since an InSb standard sample was not available), only relative areal densities of Si atoms will be discussed.

4.3 Si δ-Doping of InSb

4.3.1 Transport

Three series of δ-doped samples were grown to study Si compensation in InSb. Each sample consists of a 3μm InSb buffer layer followed by a Si δ-doped layer and a 3100Å InSb cap layer. A simple electrostatic model[1] predicts that surface pinning of the Fermi Energy removes a small density of electrons (about $7\times10^{10}cm^{-2}$ when pinned at the valance band edge) from the δ-doped layer. Due to the thick InSb buffer layer, an even smaller density would be removed by possible pinning at the substrate interface. Since the unintentional background doping is *p*-type and the intrinsic carrier density is very small at 77K [77], the measured carrier density at 77K is assumed to be entirely due to the δ-doped layer; variable temperature Hall

[1] See, for example, Section 5.4.1.

effect measurements on these samples indicate that the carrier density below about 100K is constant.

The first series of samples demonstrates the effect of substrate temperature on carrier density. For each of the samples, the substrate temperature during growth of the 3100Å InSb cap layer, T_{cap}, was the same as the substrate temperature during δ-doping, T_δ. However, $T_\delta (= T_{cap})$ was varied for each of the nine samples that comprise this series. The filled circles in Figure 4.1 show the 77K electron mobility, μ, which will be discussed in Section 4.3.3, and density, n, as a function of T_δ for eight of the nine samples. For T_δ well below T_{tr} , the carrier density maintains a roughly constant value of $4\times10^{12}\text{cm}^{-2}$. The doping efficiency in this temperature regime is the same when $T_\delta = T_{tr} - 90°\text{C}$ (not shown, different growth run)[2], independent of growth rate at least from 0.8 to 1.6 ML/s (not shown, different growth run)[3], and equal to that observed in our uniformly Si-doped InSb layers grown at similarly low temperature. However, for temperatures above T_{tr}, the carrier density decreases strongly with increasing T_δ and eventually becomes p-type for the ninth sample in the series, which was doped at $T_\delta + 40°\text{C}$ (not shown)[4]. Preliminarily, this transition from n- to p-type suggests that desorption of Si at the time of doping and/or dopant compensation is occurring for growth at substrate temperatures in excess of T_{tr}.

In GaAs uniformly doped with Se [78], a reduction in carrier density is due to increasing Se desorption from the GaAs surface with increasing substrate temperature. To explore the possibility of Si desorption and to edify the relative importance of T_δ and T_{cap}, a second series of samples was grown. All three samples in this series were grown with the same low $T_{cap} = T_{tr} - 20°\text{C}$ but with different values of T_δ. The open

[2]See S439 in App. D.
[3]See S485 in App. D.
[4]See S313 in App. D.

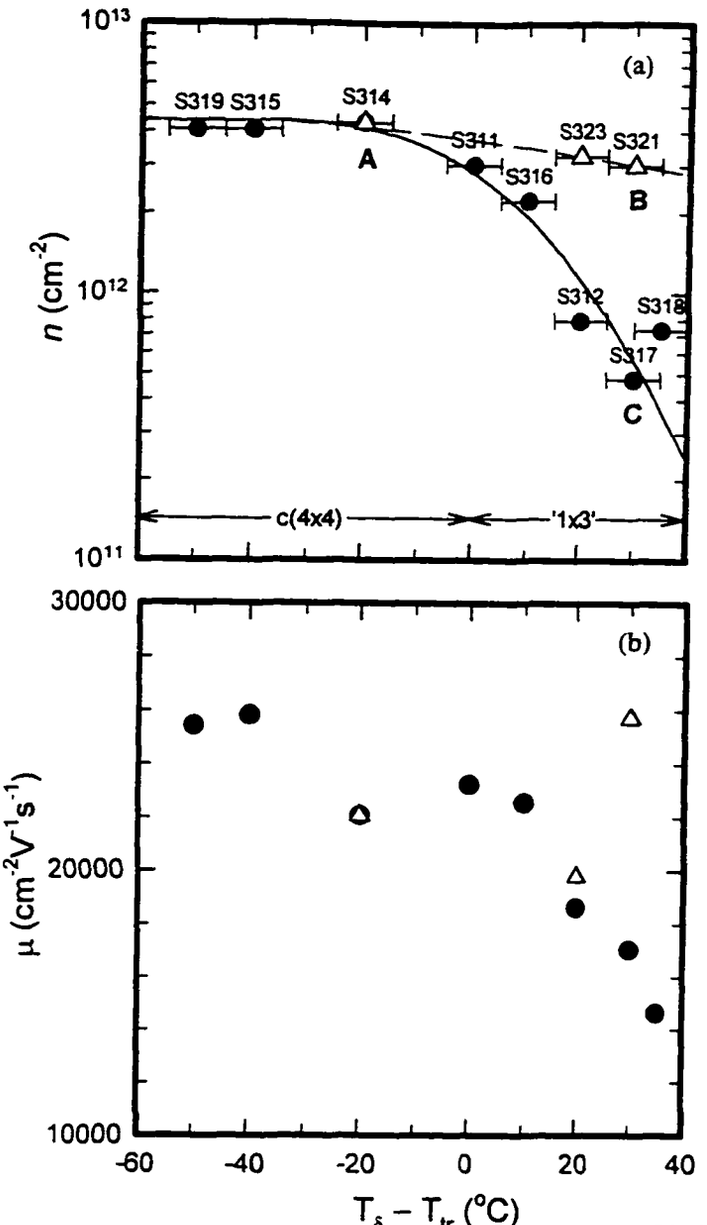

Figure 4.1: (a) Carrier density and (b) mobility at 77K for Si δ-doped InSb as a function of sample temperature at the time of δ-doping. Solid circles represent samples grown with $T_\delta = T_{cap}$. A sample grown at T_{tr} + 40°C (not shown) had a p-type carrier density of 4×10^{11}cm^{-2}. Open triangles represent samples grown with $T_{cap} = T_{tr} - 20$°C. The solid and dashed lines are fits to the data. The decrease in mobility as carrier density decreases is evidence for autocompensation (Sec. 4.3.3).

triangles in Figure 4.1 show the measured electron density as a function of T_δ. Note that the measured electron densities in these are several times higher than in samples where both T_δ and T_{cap} are high (solid circles directly below open triangles) but are not much lower than when both temperatures were low (Sample A). The ability to achieve a relatively high electron concentration by lowering the substrate temperature prior to growth of the cap layer indicates that Si desorption is not primarily responsible for the T_δ dependence. It is also evident that T_δ and the surface reconstruction at the time of doping is of minor importance while T_{cap} has the dominant influence on carrier density. To test this hypothesis even further, another sample was grown with $T_\delta = T_{tr} - 20°C$ and $T_{cap} = T_{tr} + 30°C$ (not shown)[5]. This sample was p-type, and we therefore conclude that temperature-dependent compensation occurs primarily during growth of the cap layer and not at the time of doping.

To determine whether compensation occurs due to simple diffusion, a sample identical to Sample A ($T_\delta = T_{cap} = T_{tr} - 20°C$) was grown but with an *in situ* anneal performed after growth while leaving the Sb shutter open[6]. The sample was annealed at $T_{tr} + 40°C$ for a time equal to that needed to grow the δ-doped and cap layers, which is about 18.5 minutes. The measured carrier density of $3.70 \times 10^{12} cm^{-2}$ is only slightly lower than what was obtained for Sample A. Hence, simple diffusion is not the dominant mechanism for compensation.

A third series of samples was grown to confirm that compensation occurs during growth of the cap layer and to determine the number of InSb monolayers following doping required to saturate the compensation. Each sample was grown at $T_{\delta-N} = T_{tr} + 30°C$ and $T_{cap-N} = T_{tr} - 20°C$, where N is the number of additional monolayers of InSb grown at high substrate temperature on top of the δ-layer. Figure 4.2 shows

[5]See S320 in App. D.
[6]See S338 in App. D.

the dependence of the measured carrier density on N. Samples B and C, shown in both Figures 4.1 and 4.2, have $N = 0$ and $N = 957$, respectively. We observe that "covering" the dopant with 5 MLs of InSb results in only a 2% lower carrier density than in Sample B, while 20MLs and 50MLs of coverage result in a reduction in electron concentration of about 20% and 66%, respectively, from that of Sample B. Since Si desorption and diffusion play, at most, only minor roles, these data indicate that the observed compensation occurs during surface segregation of the Si atoms during growth of the cap layer.

4.3.2 SIMS

To verify that surface segregation occurs for high T_{cap}, a sample containing several δ-doped layers was grown for SIMS measurements. For the two δ-doped layers closest to the surface, a plot of Si concentration in relative units is shown in Figure 4.3a as a function of depth. The first δ-doped layer, labeled I in Figure 4.3a, was deposited at $T_{tr} + 40°C$. The InSb layer that immediately followed this δ-doped layer was also grown at $T_{tr} + 40°C$. The second δ-doped layer, labeled II in Figure 4.3a, and the InSb layer that followed were deposited at $T_{tr} - 20°C$. The similar areas under both peaks confirm that Si desorption is not primarily responsible for the temperature dependence of the carrier density.

Peak I, corresponding to the higher temperature layer, is wider and less intense than peak II. Systematic profile broadening for SIMS is dominated by a combination of a symmetrical broadening about the maximum (which worsens with depth) due to surface roughening and an asymmetrical broadening toward the substrate (which is independent of depth) due to atomic-mixing effects [36]. Perhaps due to the softness of InSb, SIMS depth resolution is worse for InSb[7] [79] than for other III-V materials.

[7] See Ref. [67] for another example of SIMS of InSb.

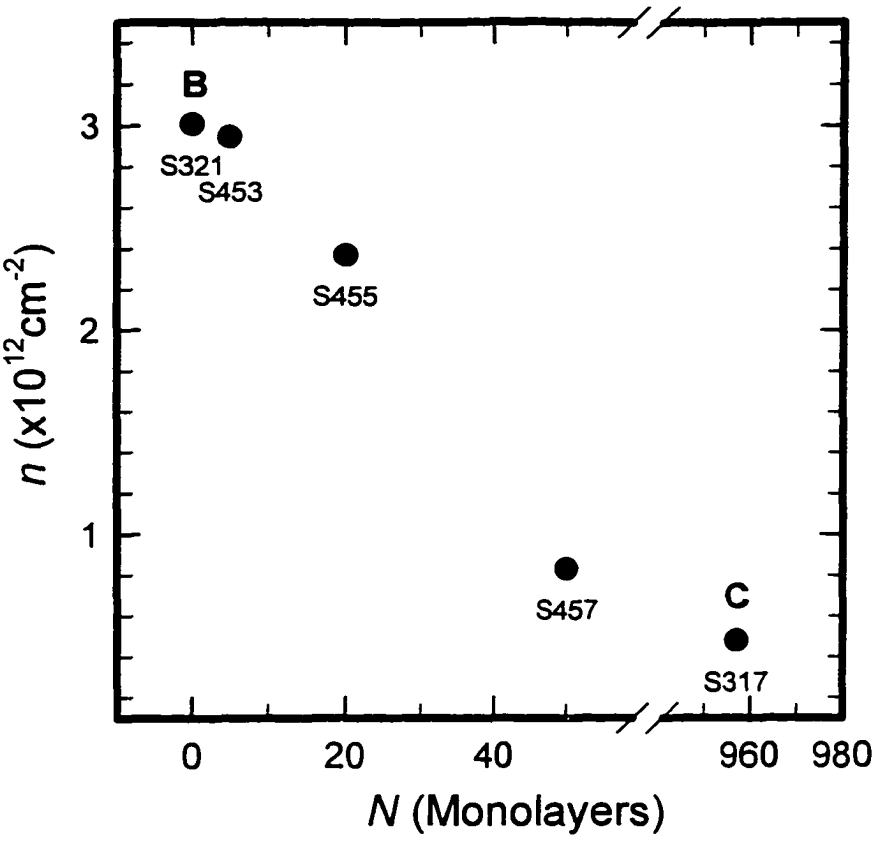

Figure 4.2: Carrier density in InSb as a function of number of monolayers, N, grown on top of the δ-doped layer at $T_{tr} + 30°C$ before reducing the substrate temperature to $T_{tr} - 20°C$ for the remainder of the cap-layer growth.

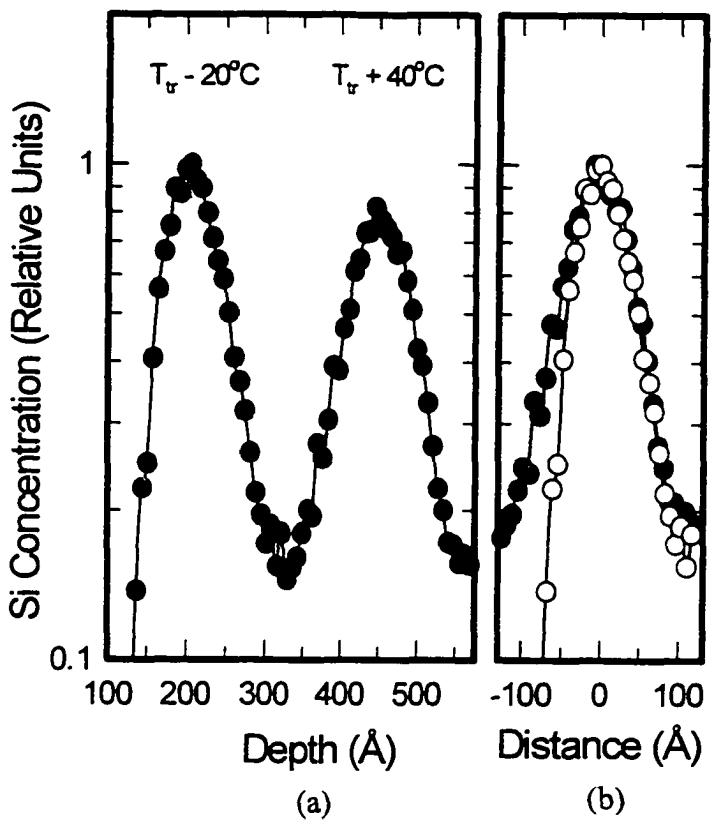

Figure 4.3: (a) SIMS profile of Si concentration as a function of depth for two δ-doped layers near the InSb Surface (S351). (b) Peaks I (solid) and II (open) are normalized to the same height and plotted with their peaks aligned. The relative broadening of peak I toward the surface suggests Si surface segregation.

To better visualize the data, peaks I and II were normalized to the same height and plotted with their peaks aligned, as shown in Figure 4.3b. The broadening of peaks I and II toward the substrate appears similar but peak I is noticeably more broadened toward the surface than peak II. This is consistent with Si segregation toward the surface for layers grown at high temperature. However, the width of peak I could also be due, at least in part, to increased surface roughening.

4.3.3 Possible Compensation Mechanisms

A mechanism leading to the observed temperature dependence of the carrier density could depend on the number of In sites available to Si atoms on the surface. Recent scanning tunneling microscope images indicate that the InSb c(4×4) surface reconstruction is completely Sb terminated, while the '1×3' reconstruction contains 1/3 Sb sites and 2/3 In sites [35]. This suggests that the observed carrier dependence may be due primarily to autocompensation arising from site competition during surface segregation, which is a phenomenon that becomes more significant at higher temperatures [36].

Further evidence for the existence of autocompensation comes from a plot of the 77K mobility as a function of substrate temperature at the time of doping for the first series of samples shown in Figure 4.1. A trend toward an increase in mobility as density increases is consistent with autocompensation. Since all of the samples contain the same concentration of Si atoms, autocompensation would result in the same number of ionized Si atoms (i.e. scattering centers) in each sample, but a net decrease in the number of electrons. This results in decreased electron screening and a corresponding increase in scattering, which results in a lower mobility. However, additional experiments are required to distinguish between this mechanism and other

possibilities, such as electrically inactive Si complexes and Si pairs. that have been observed in δ-doped GaAs with Si densities above about $1\times10^{13}cm^{-2}$ [80].

4.3.4 Maximum δ-Doping Density

As mentioned above, and demonstrated in Chapter 5, high mobility quantum wells can be realized by remote doping. Frank Stern calculated, for the case of 2-D confinement in a remotely doped GaAs/$Ga_{1-x}Al_xAs$ heterojunction, the remote doping configuration leading to the least amount of remote ionized scattering is realized by the highest practical doping density in the barrier [65]. As mentioned at the end of Section 4.3.3, the highest practical Si doping density for GaAs is less than $1 \times 10^{13}cm^{-2}$; structures requiring more than $1 \times 10^{13}cm^{-2}$ can no longer employ δ-doping.

To determine the 2-D density limit for InSb, a final series of δ-doped InSb structures was grown to characterize carrier density, n, as a function of time that the Si shutter remained open, t_δ, as shown in Figure 4.4. All of the samples were doped at $T_\delta = T_{tr} - 20°C$ with a Si cell temperature of 1305°C. The line is a linear fit of the points S452-S487 and is forced to pass through zero. We observe that the measured density is a linear function of the doping time up to a density of at least $8\times10^{12}cm^{-2}$, which, if all of the electrons were "transferred" to a 220Å well (Chap. 5), would correspond to a high[8] well concentration of $3.6 \times 10^{18}cm^{-3}$. However, S497, doped for 257s, falls well below the line fitted to the other points. This is most likely due to factors such as autocompensation, Si complexes, and inactive Si pairs, as discussed in the previous section.

The linear behavior below $8 \times 10^{12}cm^{-2}$ in Figure 4.4, combined with a constant

[8] Undoped InSb has an intrinsic room temperature density of about $2 \times 10^{16}cm^{-3}$, as discussed in Chapter 5.

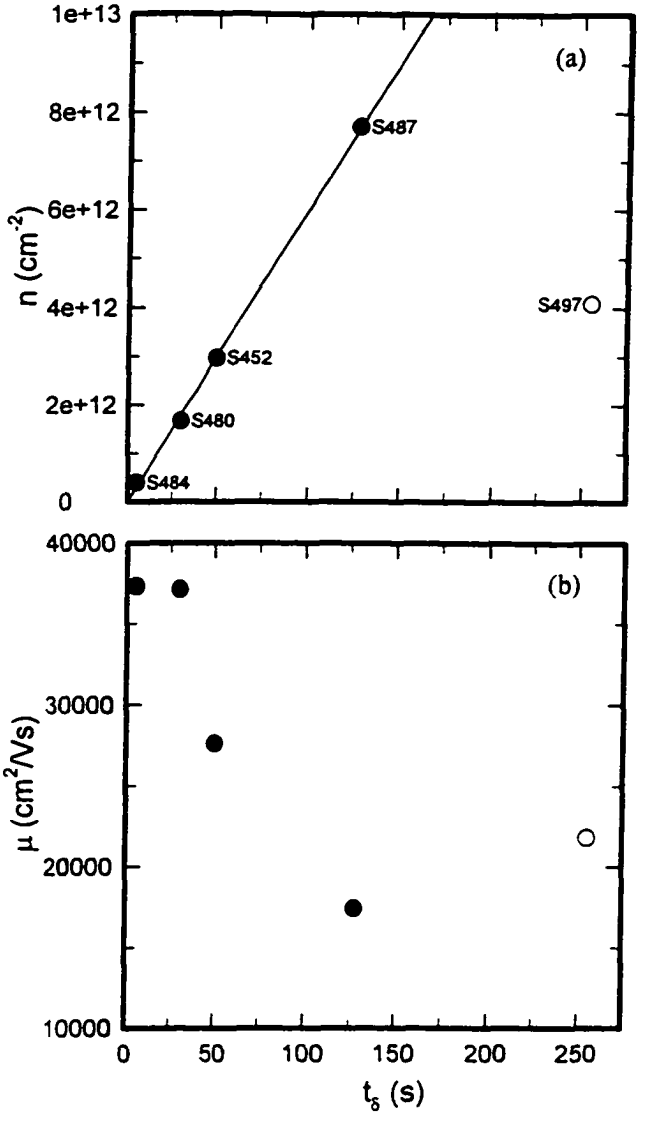

Figure 4.4: 77K (a) carrier density and (b) mobility as a function of doping time for δ-doped InSb samples grown at $T_\delta = T_{cap} = T_{tr} - 20°C$ and a Si cell temperature of 1305°C. The line is a linear fit for the points S452-S487 and is forced to pass through zero. We observe a linear carrier density as a function of doping time up to at least $8 \times 10^{12}cm^{-2}$. We attribute the deviation from linearity in sample S497 to compensation occurring at high Si densities.

measured density for dopant layers grown at $-90^oC \leq T_{cap} \leq T_{tr}$ (Fig. 4.1), implies a 100% (Donor:Si) ratio when doped below T_{tr}. However, this contradicts SIMS results using a GaSb standard that indicate the ratio is closer to 15%. This discrepancy is under investigation.

4.4 Si δ-Doping of AlInSb

Dopants in InSb quantum-well heterostructures are often placed in the barrier material [63, 64]. To explore compensation in Si δ-doped $Al_xIn_{1-x}Sb$, a fourth series of samples was grown. Each sample consists of a 3μm $Al_{0.09}In_{0.91}Sb$ buffer layer followed by a Si δ-layer and a 3100Å $Al_{0.09}In_{0.91}Sb$ cap layer. The 77K electron density and mobility as a function of T_δ is shown in Figure 4.5 with samples grown with $T_\delta = T_{cap}$ represented by filled circles. A distinct decrease in the measured mobility and carrier density is observed as T_δ is increased above T_{tr}, in like fashion with the InSb samples. The two samples shown as open triangles were grown with the same low $T_{cap}(= T_{tr} - 20^oC)$ but with different values of T_δ. Again, the behavior is qualitatively similar to that which is seen for the δ-doped InSb samples.

4.5 Conclusions

Dopant compensation was studied for Si δ-doped InSb samples grown on GaAs(001) substrates. Hall-effect measurements indicate a sharp decline in electron density with increased substrate temperature when doping and cap-layer growth occur on the '1×3' surface reconstruction, while little temperature dependence is observed for doping and growth on the c(4×4) surface reconstruction. Hall-effect measurements on samples grown with the substrate temperature differing between the dopant and cap layers rule out simple diffusion and desorption of Si atoms, and, along with SIMS

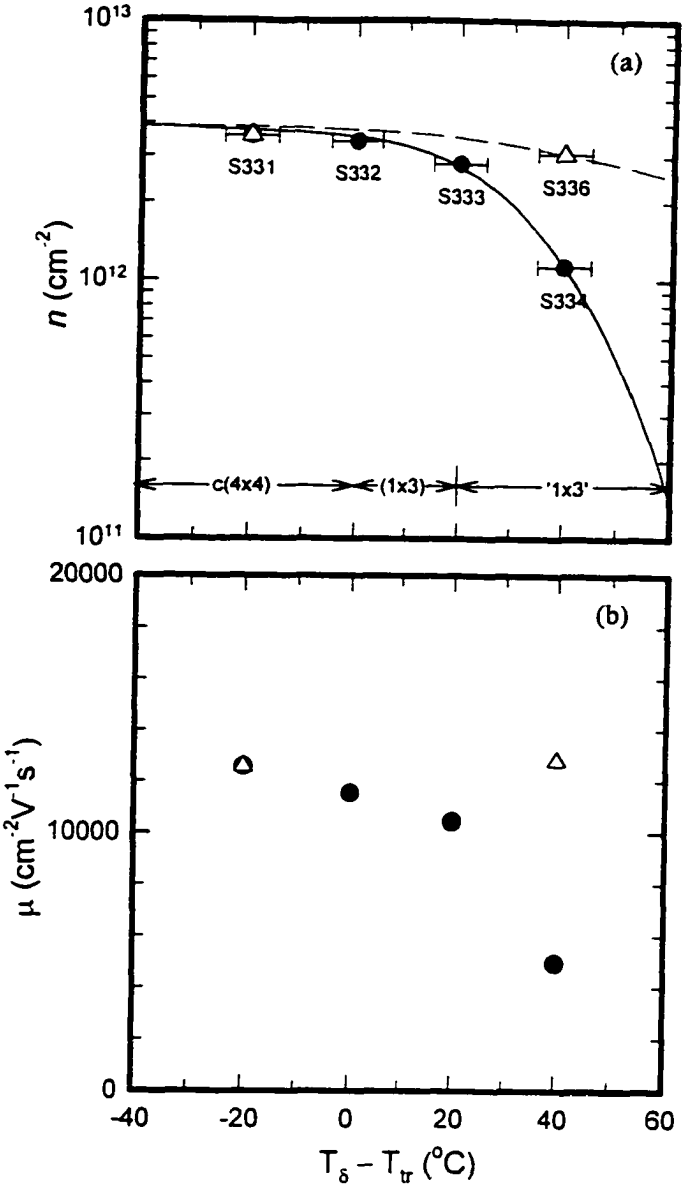

Figure 4.5: 77K (a) carrier density and (b) mobility in $Al_{0.09}In_{0.91}Sb$ as a function of sample temperature at the time of δ-doping. Solid circles represent samples grown with $T_\delta = T_{cap}$. Open triangles represent samples grown with $T_{cap} = T_{tr} - 20°C$. The solid and dashed lines are fits to the data. The decrease in mobility as carrier density decreases is evidence for autocompensation (Sec. 4.3.3.

measurements, suggest that the temperature dependence of the carrier density results from compensation occurring primarily during growth of the cap layer. Autocompensation is the most probable mechanism, but other experiments are required to distinguish between this and other mechanisms. Similar behavior was observed in $Al_{0.09}In_{0.91}Sb$ samples δ-doped with Si.

Chapter 5

High Mobility InSb Quantum Wells

5.1 Introduction

The intrinsically high mobility of electrons in narrow-gap semiconductors makes InSb thin films attractive for the basic research of quantum transport in this material, as discussed in Section 6.2, as well as for industrial applications, such as magnetic-field sensors. At present, Te-doped InSb epilayers are paired with rare-earth metal magnets in automotive position-sensing applications where accuracy and repeatability are critical [6, 7]. These devices exploit a geometrical magnetoresistance where sensitivity is proportional to mobility squared [8], hence, InSb is a natural candidate since its room temperature mobility in thin films is $\mu \approx 60,000 \mathrm{cm}^2/\mathrm{Vs}$. However, InSb also has a very small bandgap, which makes the carrier density ($\approx 2 \times 10^{16} \mathrm{cm}^{-3}$ at 300K), and therefore the sensitivity of the device, largely dependent on temperature. To minimize this dependence, the layers must be doped. The Te doped sensors consist of a 1.5μm-thick InSb layer grown on a GaAs substrate and have an electron concentration of $8 \times 10^{16} \mathrm{cm}^{-3}$ and a room temperature mobility of μ=40,000cm^2/Vs. Unfortunately, the accompanying increase in ionized impurity scattering reduces the

electron mobility and, consequently, the device sensitivity.

Remotely-doped InSb quantum-well structures are potentially better suited for magnetoresistance applications than uniformly-doped InSb epilayers. Increased sensitivity is possible since a high mobility can be maintained (since the carriers are spatially separated from the dopant) while achieving a high extrinsic electron concentration. Also, the temperature dependence of the electron concentration can be reduced since only very thin layers of InSb are required, resulting in a low ratio of intrinsic to extrinsic carriers in the well.

The achievement of an InSb quantum well was difficult due to the lack of a suitable barrier material. An initial attempt was made using CdTe as a barrier [9]. As shown in Figure 1.4, CdTe has a nearly identical lattice constant to that of InSb. However, CdTe is a II-VI material, and cross-doping with the III-V InSb at the interfaces limited the electron mobility in the well to less than 30,000cm^2/Vs [10] at 4.2K. Recent experiments have shown that quantum confinement in InSb wells can be achieved using $Al_xIn_{1-x}Sb$ barrier layers [11], and that remote doping can be accomplished with Si δ-doped layers [50, 64].

In this chapter, I discuss the electrical properties of InSb quantum-well structures with $Al_xIn_{1-x}Sb$ barriers grown by MBE on GaAs(001) substrates. Mobilities up to 41,000cm^2/Vs at room temperature and 380,000cm^2/Vs at 6.5K are observed in Hall-effect measurements. Although the room-temperature mobility is the same as in the uniformly-doped InSb mentioned above, the electron concentration in the quantum wells, 2.4×10^{17}cm^{-3}, is several times larger. Morphological characterization by atomic force microscopy indicates that defects propagating through the wells and the corresponding roughness at the well/barrier interfaces may be a factor limiting the electron mobility. Increases in both the mobility and the electron

concentration are anticipated from modifications to the layer structure.

5.2 Experiment

All InSb/$Al_xIn_{1-x}Sb$ growths were performed in an Intevac Modular Gen II molecular beam epitaxy system that has been described in Section 2.3. Growth rates for InSb and AlSb were calibrated and $Al_xIn_{1-x}Sb$ composition was deduced from temporal oscillations in the intensity of reflection high energy electron diffraction (RHEED) pattern (Sec. 2.3.2) and verified through high resolution x-ray diffraction (Chap. 3). An $Al_xIn_{1-x}Sb$ alloy composition with x=0.09 was maintained to keep the lattice mismatch to InSb below about 0.5% while allowing for a sufficiently large barrier for the electrons in the quantum wells [11]. Delta-doping (Chap. 4) was performed under an Sb flux and at a Si cell temperature of 1273°C (approximately 5.3×10^{11} net donor atoms $cm^{-2}s^{-1}$). Substrate temperatures were calibrated through changes in the static (Sb flux only) RHEED pattern upon crossing the transition temperature, T_{tr} ≈390°C [76], at which the $Al_xIn_{1-x}Sb$ surface reconstruction changes between c(4×4) and pseudo-(1×3).

The nominal layer structure used for all of our quantum wells is shown in Figure 5.1, where N denotes the number of quantum wells. The samples discussed herein differed in the number of quantum wells and the inclusion or omission of δ-doped layers (a), (b), and (c). Growth was performed on semi-insulating GaAs substrates, rather than InSb substrates, to prevent parallel conduction through the substrate. Because the equilibrium lattice constant of GaAs is about 15% smaller than that of the $Al_{0.09}In_{0.91}Sb$ barrier material, a 1μm buffer layer of AlSb, which has an intermediate lattice constant, was grown directly on the GaAs substrate[1] [81]. A 1μm-thick

[1] A 1μm GaSb layer, which has approximately the same lattice constant as AlSb, was grown between the GaAs and AlSb layers for several samples without a significant difference in carrier

$Al_xIn_{1-x}Sb$ layer was grown next, followed by a 10-period 25Å-$Al_xIn_{1-x}Sb$/25Å-InSb strained layer superlattice for dislocation filtering and surface smoothing [82, 83]. A 3μm $Al_xIn_{1-x}Sb$ buffer layer was grown to promote full lattice relaxation as well as to isolate the carriers in the well from scattering centers associated with this relaxation[2]. High resolution x-ray diffraction measurements have demonstrated the effectiveness of GaSb, AlSb, and $Al_xIn_{1-x}Sb$ buffer layers [50]. The $Al_xIn_{1-x}Sb$ buffer layer was grown at $T_{tr} + 50 \pm 5$°C, since growth on a pseudo-(1x3), as opposed to c(4x4), surface reconstruction results in better pseudomorphic growth.

Electrons are supplied to each strained InSb quantum well by Si δ-doped layers in the adjacent $Al_xIn_{1-x}Sb$ barrier(s). Each of the N quantum wells is nominally 220Å thick. All layers following and including the last 0.1μm of the $Al_xIn_{1-x}Sb$ buffer layer were grown at a substrate temperature of $T_{tr} - 30 \pm 5$°C in order to minimize Si compensation (Chap. 4) [50, 75]. Additional Si atoms were included in the δ-doped layer nearest to the surface in order to provide electrons for surface states. An InSb cap was added to prevent possible oxidation of an $Al_xIn_{1-x}Sb$ surface.

Hall effect measurements at magnetic fields up to 0.5T were performed on square samples whose edges are about 4mm long to determine carrier density and mobility. Electrical contact was made at each corner of a sample (See Fig. 1.2), as discussed in Appendix A. Ohmic contact was checked through observation of linear current-voltage characteristics in four-point measurements. Resistivity was determined from van der Pauw measurements (Sec. 1.2.2) [14], and variable temperature experiments were carried out using an APD Cryogenics HC-2D-1 Helium Compressor with a DE-202A Two-Stage Expander. Data were obtained via software originally written by

density or mobility.

[2]Samples grown with only a 1μm buffer layer exhibited mobilities at least 50% less than those structures with a 3μm buffer layer.

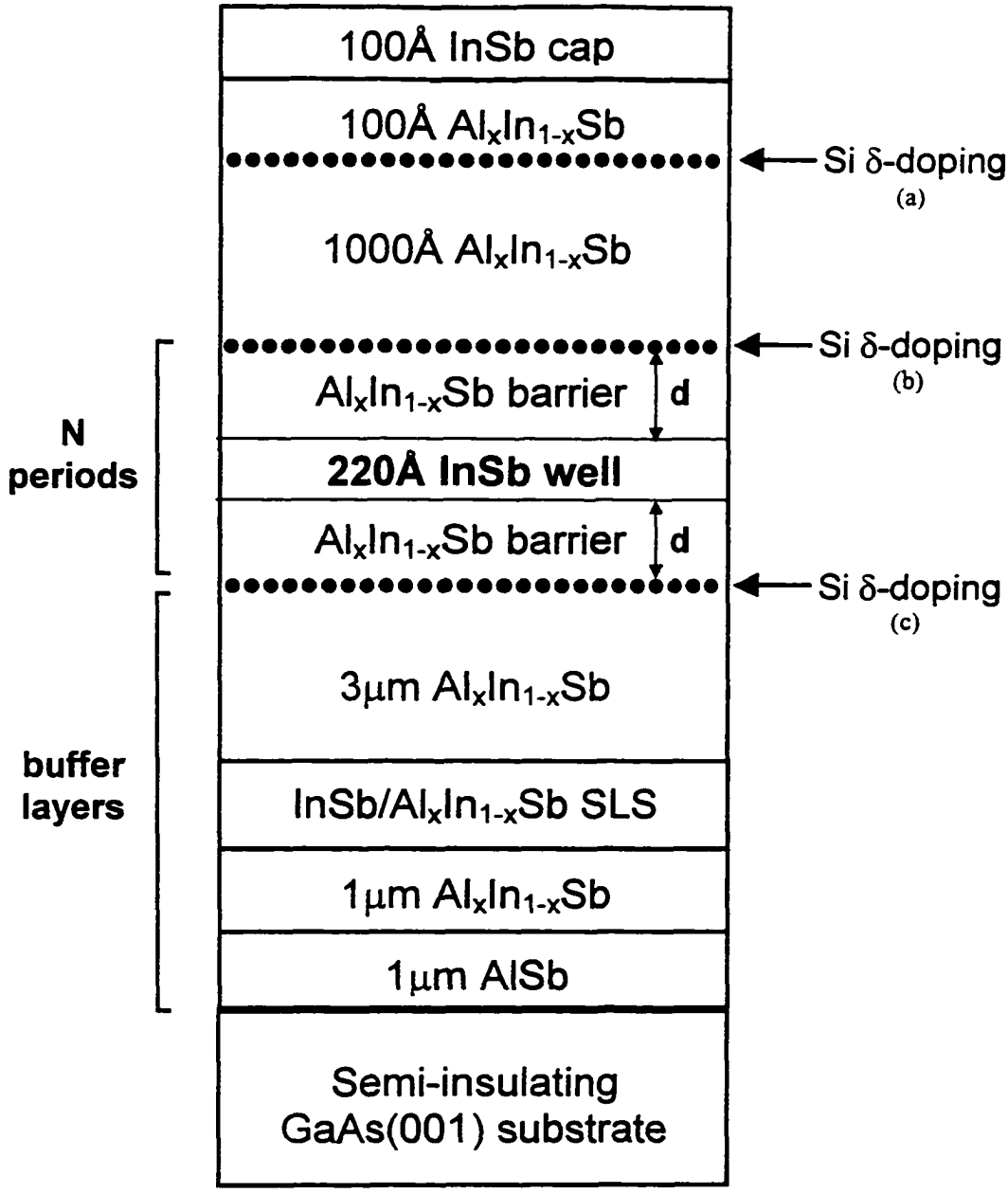

Figure 5.1: Nominal layer sequence for the remotely-doped quantum well structures. N denotes the number of quantum wells, and $x = 0.09$ was used in all samples. The samples discussed herein differed in the number of quantum wells and the inclusion or omission of δ-doped layers (a), (b), and (c).

the author and J. Winesett using LabWindows, ver. 2.1, and improvements to the software were made by the author, F. W. McKenna, N. M. Cunningham, and R. C. Meyer using LabView, ver. 4.0.1.

Samples for which atomic force microscopy was performed were scanned in air using a Topometrix atomic force microscope (AFM) running in non-contact phase mode. The high-resonant- frequency silicon tip had an aspect ratio of approximately 3:1 and a radius of curvature less than 200Å.

5.3 Limitations on Well Width

To determine the appropriate thickness for the quantum wells, a series of samples with $N = 1$ was grown. These samples were nominally grown as shown in Figure 5.1 with δ-layers (a) and (c) omitted, along with the 1000Å $Al_{0.09}In_{0.91}$ Sb shown between δ-layers (a) and (b). In this series, $d = 400$Å was used for each of the samples. δ-layer (b) had a net donor density of 1.6×10^{12}cm^2, and the only parameter that was changed was the thickness of the well, d_{well}. The Matthews and Blakesly critical thickness [84], t_c, which determines how thick an epilayer can be grown before relaxation begins, is given by the solution of:

$$\varepsilon = \frac{a(1 - \upsilon/4[\ln(t_c\sqrt{2}/a) + 1]}{2\sqrt{2}\pi t_c(1 + \upsilon)}, \qquad (5.1)$$

where a is the lattice constant of the sub-layer, υ is Poisson's ratio[3], and $\varepsilon = \Delta a / a$ is the strain in the layer, where Δa is the difference in lattice constant between the two layers. The calculated critical thickness for InSb grown on $Al_{0.09}In_{0.91}Sb$, using $\upsilon = 0.33$, is slightly greater than 600Å. A more detailed model was developed by Houghton, *et al.* [85]. They followed Matthews and Blakesly but incorporated more terms relating to the energy of relaxation in a calculation of the critical thickness of

[3]Poisson's ratio is approximately 1/3 for most semiconductors.

Ge_xSi_{1-x}/Si heterostructures. Using this treatment, Barnett, *et al.* [86] performed relaxation studies of the InSb/$Al_xIn_{1-x}Sb$ system, which showed good agreement with the Houghton model, and predicts $t_c \approx 400$Å for InSb/$Al_{0.09}In_{0.91}Sb$.

Figure 5.2a shows a plot of the measured 77K mobility as a function of d_{well}. We see that for 200Å$\leq d_{well} \leq$400Å, the mobility is roughly constant. However, for $d_{well} = 500$Å, a significant drop in carrier mobility is observed. Relaxation occurring in the quantum well would result in a lower mobility due to misfit dislocations as t_c is exceeded. If this is the dominant mechanism leading to the large drop in mobility, the apparent critical thickness, 400Å$\leq t_c \leq$500Å, agrees well with the value predicted by Barnett, *et al.* These data are qualitatively similar to that reported by Bolognesi, *et al.* [87] for InAs/AlSb quantum wells.

A wider well could also increase the number of populated subbands. Calculations by Bolognesi, *et al.* predicted only a single occupied subband in their quantum wells, and they therefore attributed their drop in mobility for wide wells to relaxation occurring in the well. To calculate the existence of additional populated subbands requires knowledge of the band offset in the conduction band, which is currently being investigated at The University of Oklahoma (Sec. 6.1) [88, 89]. However, the results of a self-consistent calculation in the Hartree approximation [90], assuming a band offset of 75%, indicate a second subband would be about half filled for $d_{well} = 500$Å with our measured well density of 2.92×10^{11}cm^{-2}; the second subband for $d_{well} = 400$Å is not filled or only partially filled for our measured well density of 2.67×10^{11}cm^{-2}. As a result, increased intersubband scattering could account, at least in part, for the drop in mobility for $d_{well} > 400$Å.

We also observe a low carrier mobility for the sample with $d_{well} = 150$Å. At low temperature, the dominant scattering mechanisms [91, 92, 93, 94, 95, 96] for remotely

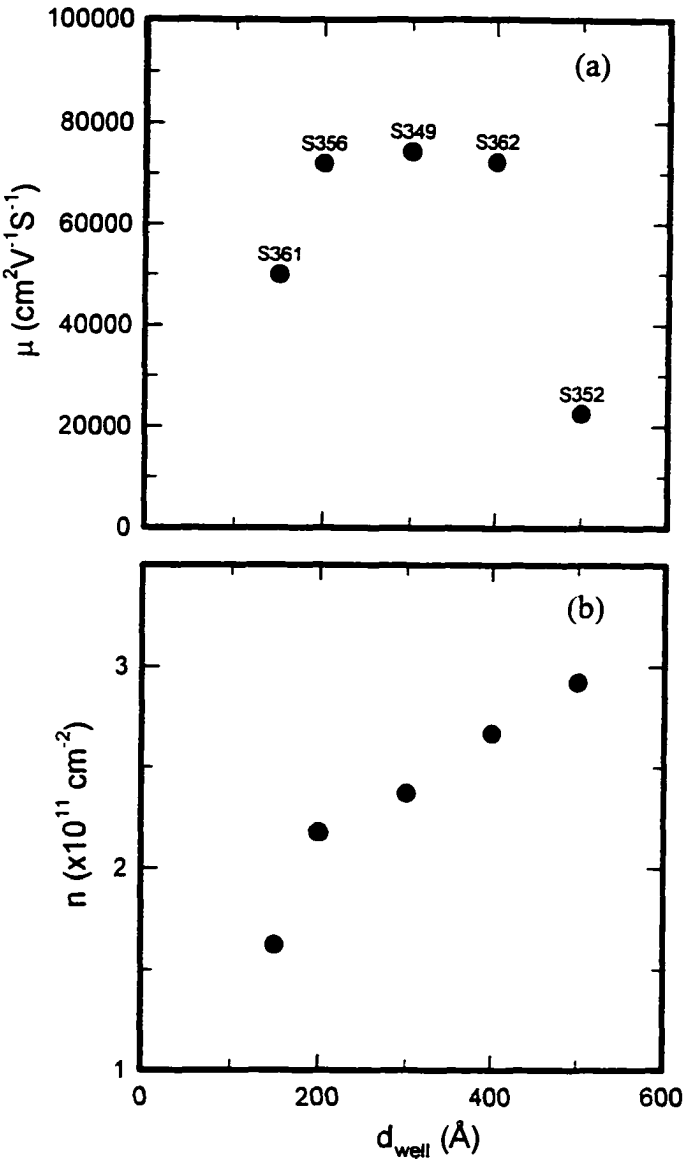

Figure 5.2: 77K (a) mobility and (b) carrier density as a function of well thickness. Low mobility below 200Å is attributed to interface roughness, and low mobility above 400Å is attributed primarily to relaxation of the well, and also possibly to intersubband scattering.

doped quantum wells are from unintentional background impurities, remote ionized dopants, and the roughness of the quantum well/barrier interface(s). All the samples in this series presumably have the same unintentional impurity density since they were all grown within a two-week period, and all of the samples have the same value of d. Therefore, we attribute the decrease in mobility for the $d_{well} = 150$Å sample to roughness of the well/barrier interface, which is a scattering phenomenon that has been shown to decrease in strength for Si/Si_xGe_{1-x} [93], InAs/AlSb [87], and GaAs/AlAs [97, 98] quantum wells roughly according to $(d_{well})^6$.

It is therefore important for our structures to have $200\text{Å} \leq d_{well} \leq 400\text{Å}$. Since we desire only one populated subband in our structures[4], a narrow well is appropriate (Sec. 1.4), and a value of $d_{well} = 220$Å was chosen.

Equation 1.39 indicates that the quantized energy level is inversely proportional to $1/(d_{well})^2$ for an infinite square well. Assuming the Fermi level is pinned at the conduction band edge for all samples, Equation 1.43 is integrated over a wider interval, resulting in a larger carrier density, as d_{well} is increased. We would expect to see an analogous dependence for our finite square wells. Figure 5.2b shows a plot of the measured carrier density as a function of d_{well}, and, as expected, shows a monotonic increase in n as d_{well} is increased.

[4] Electrons in the ground state have a wavefunction that is more confined to the center of the well, compared to higher energy wavefunctions, resulting in less scattering from both the well/barrier interface and the ionized dopant. In addition, the ground state wavefunction penetrates into the barrier less than higher energy wavefunctions, where the electron mobility is intrinsically much lower. The lower mobility of the high energy level electrons is equivalent to a parallel conduction path; the existence of parallel conduction paths makes the interpretation of transport data more difficult (Sec. 6.2).

5.4 Transport Data

5.4.1 Single Quantum Wells

"Single-Doped" Single Quantum Wells (SDSQW)

Initially, a series of six "single-doped" single quantum well (SDSQW) samples (i.e. $N = 1$) was grown with $Al_{0.09}In_{0.91}Sb$ barrier layers sandwiching a 220Å-thick InSb quantum well. Again, these samples were nominally as shown Figure 5.1 with δ-layers (a) and (c) omitted, along with the 1000Å $Al_{0.09}In_{0.91}$ Sb shown between δ-layers (a) and (b). To provide electrons for the quantum well and surface states, δ-layer (b) (net donor density of $\approx 1.6\times10^{12}cm^{-2}$) was placed in the upper $Al_xIn_{1-x}Sb$ barrier a distance of 100Å$\leq$d$\leq$500Å above the InSb quantum well. All samples in the series had the same growth parameters (substrate temperature, Sb/In flux ratio, growth rates, etc.) and identical layer structures except for the spacer layer thickness, d. Figure 5.3 shows the measured electron density n and mobility μ as a function of d at 77 K.

A simple electrostatic model can be used to explain the observed dependence of electron density on spacer layer thickness. Figure 5.4 defines several parameters used in Equations 5.2 and 5.3:

$$\frac{qn}{\epsilon} = \frac{E_b - E_F}{qd}, \tag{5.2}$$

$$n = \int_{E_o}^{E_F} D(E)dE. \tag{5.3}$$

Equation 5.2 describes the electric field in the spacer layer. In the right hand side, background ionized impurities are ignored and the Fermi level at the δ-doped layer is assumed pinned at the conduction band edge. The left hand side is obtained by integrating Poisson's equation, where ϵ is the permitivity. The well density at zero temperature is calculated in Equation 5.3, assuming only a single subband is

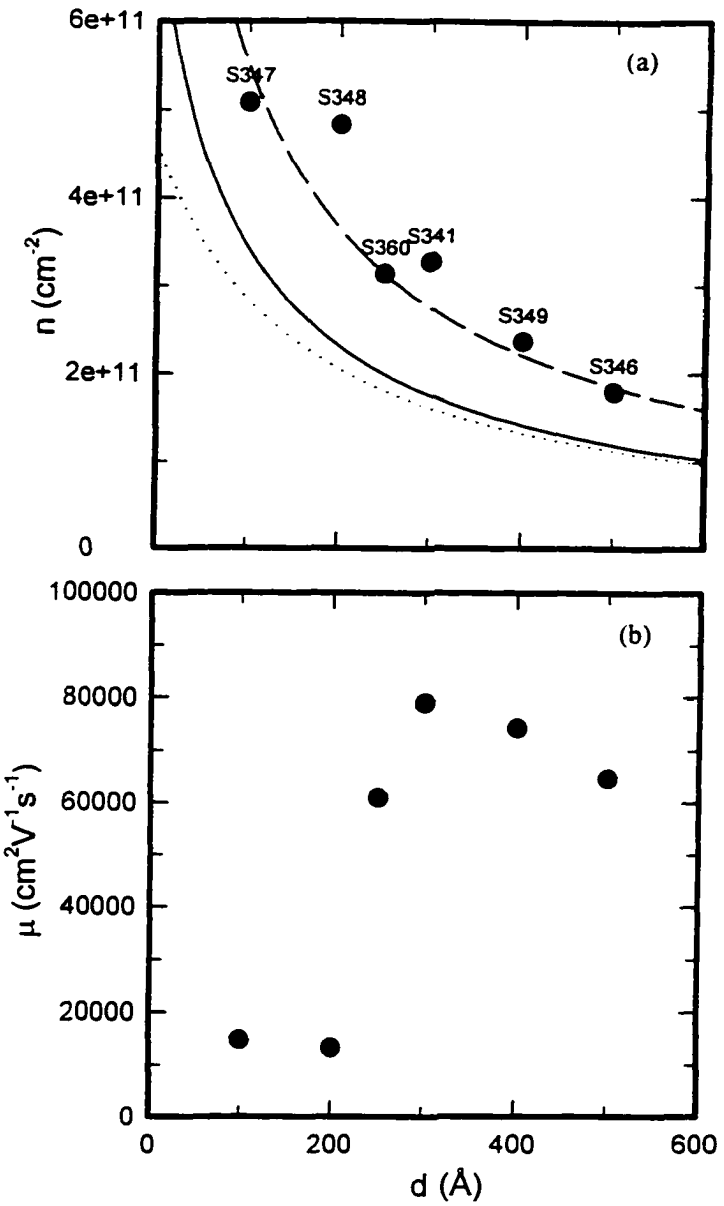

Figure 5.3: Measured electron (a) density and (b) mobility at 77K in "single-doped" single quantum-well structures. The dashed line in (a) shows the prediction of a simple electrostatic model assuming a non-parabolic dispersion relation and an 85% band offset. The solid line shows the non-parabolic prediction assuming a 60% band offset. The dotted line shows the prediction assuming a parabolic dispersion relation and a 60% band offset.

occupied.

For a parabolic dispersion relation, the density of states is a constant $D(E) = m_\Gamma^*/\pi\hbar^2$. An analytic expression for n as a function of d is obtained by simultaneously solving Equations 5.2 and 5.3:

$$n = \frac{(E_b - E_o)}{1/D + q^2 d/\epsilon}. \tag{5.4}$$

This dependence is shown as a dotted line in Fig. 5.2a, using values of $m_\Gamma^* = 0.0145 m_e$ and $\epsilon = 17.7\epsilon_o$. The barrier height $E_b = 100.2$meV was deduced by assuming that 60% of the InSb/$Al_xIn_{1-x}Sb$ band edge discontinuity appears in the conduction band. In calculating the subband energy $E_o = 24$meV, strain and the non-parabolic dispersion relation were taken into account but the effects of band bending were ignored.

This simple model can be made more accurate by using a density of states expression that accurately reflects the non-parabolic dispersion relation. Using a two-band model (Sec. 1.3.3), the density of states is expressed by Equation 5.5, where E_g (≈ 230meV at 77K) is the bandgap of InSb:

$$D(E) = \frac{m_\Gamma^*}{\pi\hbar^2}\left(1 + \frac{2E}{E_g}\right) \tag{5.5}$$

Equations 5.2, 5.3, and 5.5 can be combined to express n as a function of d. The results of this non-parabolic calculation are shown as solid and dashed lines for a band offset of 60% and 85%, respectively, in Figure 5.3a. The dashed line is in better agreement with the data, but recent studies at The University of Oklahoma suggest that the band offset is less than 77% (Sec. 6.1) [88], so the better fit assuming an 85% offset is likely coincidental. We believe the error is possibly due to uncertainties in E_F at the δ-doped layer, E_b (due to the unknown value of the conduction band offset) and E_o (due to neglecting band bending). However, the qualitative agreement

serves as evidence that the structure is a remotely-doped quantum well.

"Triple-Doped" Single Quantum Wells (TDSQW)

The dependence of μ on d in Figure 5.3 reveals the strong effect of remote ionized dopant scattering. Since n is much less than the net donor density provided by the single δ-doped layer, and parallel conduction was not evident from Hall effect measurements, the majority of donor electrons must reside in surface states. These donors providing surface electrons remain near the well and are a source of remote ionized scattering.

To achieve an increase in mobility, this "extra" dopant was placed a distance $d + 1000$Å from the well (layer (a)). The cumulative amount of Si was kept the same as for the single-doped quantum wells, and the remaining dopant was divided evenly into two δ-layers and placed a distance d on either side of the quantum well (layers (b) and (c)), as shown in Figure 5.1 for $N = 1$. A quantum well that is remotely doped on only one side has a non-zero electric field acting on the electrons, which moves the center of the electron probability density toward the positive ions (and therefore the edge of the well). This has the dual effect of increasing remote ionized scattering as well as scattering due to interface roughness[5].

When a quantum well is remotely-doped on both sides, the electrons in the well feel no external electric field if we treat the surface, ionized dopant, and confined charge as infinite sheets of charge[6]. As a result, the electron probability density will remain in the middle of the well, reducing both remote ionized and interface

[5]This is based on the assumption that the roughness of the top interface is the same as the roughness of the bottom interface. This is not the case in the InAs/AlSb quantum well system in which the bottom interface is more rough than the top [95]. Experiments to determine whether this occurs in our system have not yet been performed.

[6]The electric field associated with an infinite sheet of charge does not have a spatial dependence [99], and all of the fields in this case would cancel.

roughness scattering. In addition, if we now assume the Fermi energy is pinned on both sides of the quantum well, and taking the same assumptions as in the previous section, doping on both sides of the quantum well mandates that the left-hand side of Equation 5.2 be divided by 2. Solving the modified Equation 5.2 and Equation 5.3 again for n predicts that, for a given d, the density in our "triple-doped" structures is greater than in our "single-doped" structures. Figure 5.5 shows n and μ, along with the predicted behavior, at 6.5K for a series of TDSQW samples for which the only parameter intentionally varied was d. While the density is higher for a given value of d, we observe that the qualitative fit to our model is not as convincing as for the SDSQWs; this deviation is currently under investigation.

The increase in density given the same number of Si donors should have a positive effect on our mobility, as follows. We assume that the scattering occurring at low temperature is predominantly due to remote ionized dopants, interface roughness, and unintentional background scattering, with partial scattering times of τ_{remote}, τ_{rough}, and τ_{back}, respectfully. The total scattering time, τ_{tot}, is given by:

$$\frac{1}{\tau_{tot}} = \left(\frac{1}{\tau_{remote}} + \frac{1}{\tau_{back}} + \frac{1}{\tau_{rough}} \right), \tag{5.6}$$

where $\tau_{tot} \propto \mu$ (Eq. 1.9) in the approximation of static conductivity[7].

Taking electron interactions into account (i.e. screening), and considering a remotely doped quantum well with infinite barriers and one populated subband at zero temperature, Gold [93] and Gold *et al.* [100] calculate that the scattering time, τ_{remote}, is related to the well electron density, n, and the remote ionized dopant density, n_i, by:

$$\frac{1}{\tau_{remote}} \propto \frac{n_i}{n}, \tag{5.7}$$

[7] Treatment of dynamic conductivity includes such variables as imaginary currents and plasmons [93].

and τ_{back} is related to the unintentional background dopant density, N_{back}, and n by:

$$\frac{1}{\tau_{back}} \propto \frac{N_{back}}{n}. \tag{5.8}$$

Scattering due to interface roughness is not a Coulomb event, and therefore τ_{rough} does not have an n (i.e. screening) dependence[8]. Due to the shift in the electron probability density toward the interface for the SDSQWs, the final term in Equation 5.6 should greater for the SDSQW design[9]. In the other two terms, n_i is a constant, and N_{back} is assumed to be constant in the two types of structures. Therefore, Equations 5.7 and 5.8 should both be less for the TDSQW structure, leading to a smaller value for τ_{tot} and a corresponding higher mobility for a given spacer thickness.

From Figure 5.5b, we observe that the mobility increases up to a value of d = 600Å and then drops off dramatically. It is not clear what would cause the large drop in mobility between S523 and S517 and S520 since the densities are approximately the same and the surfaces of each sample appear to have the same density of defects when viewed under a Nomarski Microscope; this feature is also under investigation. However, as predicted, Figure 5.6a indicates the mobilities in this series at 77K are higher than the mobilities for our SDSQWs at 77K, shown in Figure 5.3b, for the same value of d.

Figure 5.6 shows μ and n as functions of temperature for the samples shown in Figure 5.5. In qualitative agreement with our model, we observe that the carrier density decreases monotonically with d at low temperature. We also observe that the mobility of the quantum wells monotonically increases as the temperature

[8] τ_{rough} is related to the average deviation in height perpendicular to the substrate and the density of these deviations parallel to the substrate in the interfaces [93].

[9] However, as discussed in Section 5.3, we are not in the regime where interface roughness scattering is the dominant scattering mechanism.

decreases down to about 50K, due to the decrease in temperature dependent scattering mechanisms, such as phonon scattering, after which the mobility approaches a roughly constant value below about 50K; the temperature at which the mobility plateaus is a figure of merit reflecting the quality of the structure. The behavior of μ as a function of temperature observed here is qualitatively the same as that seen for other remotely doped quantum well systems, such as GaAs/AlGaAs [101], in which the highest low-temperature mobilities have been reported. GaAs/AlGaAs is a nearly homoepitaxial system, allowing for a high degree of crystallinity. As a result, the electron mobility in these systems does not become constant as a function of temperature until below 2K.

5.4.2 Multiple Quantum Wells (MQWs)

A series of multiple-quantum-well (MQW) structures ($1 \leq N \leq 14$) was grown in which the only parameter intentionally varied was the number of quantum wells [63]. These structures were as shown in Figure 5.1 without layer (a). The topmost δ-layer was doped four times heavier ($3.2 \times 10^{12}\text{cm}^{-2}$ net donor density) than the rest of the dopant layers ($8 \times 10^{11}\text{cm}^{-2}$ net donor density), and no δ-layer was placed on the substrate side of the bottom quantum well, except in the $N = 1$ structure. The distance from each dopant layer to the nearest quantum well was $d = 600$A. The room-temperature and 77K values for n and μ are shown in Figure 5.7. The dependencies on N result from the increasing importance of conduction through the quantum wells with increasing N. The filled circles in Figure 5.7a show that n at 77K is linearly proportional to the number of filled quantum wells. When a quantum well is remotely-doped on both sides, the left-hand side of Equation 5.2 must be divided by 2, as discussed in the previous section. Consequently the electron

density in the well closest to the substrate will be as predicted in Figure 5.2, while our model predicts the other $N-1$ wells will have densities that are 1.7 times greater. Therefore, the number of filled quantum wells is defined as $N - 0.4$. As before, we make the approximation that n at 77K is due entirely to extrinsic electrons $N \times e_{well}$ that reside in the quantum wells but originate from Si dopants in the barrier layers. Hence, a value for e_{well} can be deduced from a line of best fit that also passes through the origin. The slope of such a line, shown in Figure 5.7a, gives $e_{well} = 3.5 \times 10^{11}\text{cm}^{-2}$.

The density at room temperature is the sum of $N \times e_{well}$ plus the intrinsic densities in the quantum wells $N \times i_{well}$, the barrier layers $N \times i_{bar}$, and the buffer layers i_{buffer}. From the slope of a line fit to the room temperature points and forced through i_{buffer} at the ordinate axis, a value of $e_{well} + i_{well} + i_{bar} = 4.5 \times 10^{11}\text{cm}^{-2}$ is determined. A value for i_{buffer} of $2.6 \times 10^{11}\text{cm}^{-2}$ is determined from a Hall measurement on a structure with the quantum wells and barriers etched off[10]. Since the bandgap of AlSb is very large, i_{buffer} is assumed to be due entirely to electrons in the 4μm $Al_xIn_{1-x}Sb$ layer with the quantum wells etched off. Multiplying i_{buffer} by a ratio of thicknesses (1200Å/4μm) yields an estimate of $i_{bar} = 0.8 \times 10^{10}\text{cm}^{-2}$. A value for $i_{well} = 4.5 \times 10^{11}\text{cm}^{-2} - 3.5 \times 10^{11}\text{cm}^{-2} - 0.8 \times 10^{10}\text{cm}^{-2} = 0.9 \times 10^{11}\text{cm}^{-2}$ can then be deduced. Dividing i_{well} by the well thickness of 220Å yields a concentration of $4.2 \times 10^{16}\text{cm}^{-3}$, a value comparable to that measured in intrinsic InSb layers (about $2 \times 10^{16}\text{cm}^{-3}$). The consistency of the deduced values of i_{buffer}, i_{bar}, and i_{well} with measured values of $Al_xIn_{1-x}Sb$ and InSb layers is evidence for the validity of our model.

The density values deduced above can be used to model the N-dependence of

[10]The etch used was that discussed in Appendix B. The etch rate was determined by etching part of the sample that was partially covered with black wax. The black wax was removed by TCE, and the step height was characterized using a Tencor P-1 Long Scan Profiler (Tencor Instruments) in the ECE Department.

the room-temperature mobility. As shown in Figure 5.7b, a trend toward higher mobility is evident with increasing N. As discussed above, an appreciable density of intrinsic carriers is present in the $Al_xIn_{1-x}Sb$ buffer and barrier layers at room temperature. As a result, the room temperature transport behavior is expected to be a combination of both intrinsic electrons in the buffer, barrier and wells, and extrinsic electrons in the wells.

For the structure with $N = 1$, the percentage of electrons that are extrinsic is about 53%, which is the ratio between n at 77K and n at room temperature. Growing structures with more periods can increase this percentage. Each additional period adds a 220Å-thick quantum well, a Si δ-doped layer, and an additional $2 \times d = 1200$Å of $Al_xIn_{1-x}Sb$ barrier material. As deduced above, the density of resulting intrinsic carriers in the additional barrier material ($i_{bar} = 0.8 \times 10^{10}\text{cm}^{-2}$) is much less than the density of additional electrons in the well ($e_{well} + i_{well} = 4.4 \times 10^{11}\text{cm}^{-2}$). Because μ in InSb is higher than in $Al_xIn_{1-x}Sb$, the ratio of high-μ carriers to low-μ carriers, and consequently the measured μ, should be enhanced. As the number of quantum wells is increased, the percentage of extrinsic carriers increases to about 78% and the mobility increases to $41,000\text{cm}^2/\text{Vs}$ when $N = 14$.

The mobility in an N-period multiple-quantum-well structure can be approximated as:

$$\mu = (n_{alloy}\mu_{alloy} + n_{well}\mu_{well})/(n_{alloy} + n_{well}), \tag{5.9}$$

where

$$n_{alloy} = i_{buffer} + N \times i_{bar} \tag{5.10}$$

is the density of electrons in the alloy layers, and

$$n_{well} = N \times (e_{well} + i_{well}) \tag{5.11}$$

is the density of electrons in the quantum wells. All the density values in Equations 5.10 and 5.11 were determined as discussed above and a value of $\mu_{alloy} = 8,000\text{cm}^2/\text{Vs}$ was measured in the etched 4μm sample of $Al_{0.09}In_{0.91}Sb$. Since all other necessary quantities in Equation 5.9 are known, a value for μ_{well} can be deduced by a single-parameter curve fit to the data in Figure 5.7b. The data are bracketed between curves with μ_{well} set at $39,000\text{cm}^2/\text{Vs}$ and $43,000\text{cm}^2/\text{Vs}$. We see from these curves that over 90% of the well mobility is obtained for an $N = 10$ structure, so more wells are not necessary.

Our measured value of $41,000\text{cm}^2/\text{Vs}$ is the highest room-temperature mobility reported in a quantum well made of any semiconductor, including InAs [102] and GaAs. However, it is still significantly lower than the $\approx$60,000cm^2/Vs that we and others [103, 16, 104] observe in undoped InSb layers on GaAs substrates. Higher quality structures are required to increase the mobility to 60,000cm^2/Vs, which requires the improvement of the buffer layers. Morphology studies are ongoing using AFM (Sec. 5.5) and should accelerate with the acquisition of a Scanning Tunneling Microscope, arriving in the Fall of 1998, that will be attached to the MBE system and will allow for *in situ* studies.

The measured mobilities at 77K are shown in Figure 5.7c. A dramatic jump in μ occurs from 126,000cm^2/Vs for $N = 1$ to 175,500cm^2/Vs for $N = 2$. Increasing N results in only a slightly higher μ, with a maximum of 209,500cm^2/Vs for $N = 10$. This is in contrast to the gradual increase in mobility observed at room temperature. Since virtually all of the carriers at this temperature are extrinsic electrons in the wells, one would expect the mobility to be independent of N. Although the causes of the anomalous low μ for $N = 1$ are still under investigation, we believe that remote ionized dopant scattering plays a major role. The very high density of the δ-doped

layer closest to the surface would make the $N = 1$ structure more limited by such scattering than structures with larger N.

Finally, Figure 5.8a shows a plot of μ as a function of temperature for our highest mobility MQW ($N = 10$) and TDSQW, where $\mu_{MQW} = 380,000\text{cm}^2/\text{Vs}$ and μ_{TDSQW}=300,000cm^2/Vs at 6.5K. As discussed above, the room temperature mobility of the MQW is larger than the TDSQW. Each has $d = 600$Å, so we expect each structure to have roughly the same number of carriers per well at low temperature. We also expect the carrier density to depend on temperature more for the TDSQW than the MQW at high temperatures. These predictions are verified in Figure 5.8b, which is a plot of n vs. T. The low temperature densities are $2.8 \times 10^{12}\text{cm}^{-2}$ and $2.3 \times 10^{11}\text{cm}^{-2}$ for the MQW and the TDSQW, respectively. We also observe that the slope of the density for the MQW is much less than the TDSQW near 300K.

5.5 Atomic Force Microscopy (AFM)

Atomic force microscopy was performed on many of the quantum-well structures [63]. Figure 5.9 shows an atomic force micrograph of the $N = 1$ structure with $d = 600$Å. The large scale image reveals pyramidal features as well as abrupt steps oriented in the [1 1 0] and [1 $\bar{1}$ 0] directions. The inset to Figure 5.9 shows that these pyramidal features are actually spiral-like structures that grow around threading (screw) dislocations. Similar spiral growth mechanisms have been observed in other III-V systems, such as GaSb [105, 106, 107], InAs [107], InP [108], and GaAs [109]. The step heights on the pyramids correspond to two monolayers and the pyramid heights range from about 100Å to 500Å with a characteristic separation of about 3μm. The size and density of these features is similar in all of the quantum well structures studied. However, the oriented abrupt steps are typically about 100Å in

height, 5-10μm long, separated by about 5μm, and, unlike the pyramidal features, are less numerous in the structures with $N > 1$. This may be due to dislocation filtering occurring at the well/barrier interfaces of our $N > 1$ structures.

These studies indicate that the penetration of defects through and morphology of the active layers may play a role in limiting the mobility of the electrons in the wells. Both the pyramidal and oriented abrupt steps cause thickness variations comparable to the well width (220Å). Moreover, the spacing of these defects is on the same scale as the mean free path of the electrons in the wells [$l = (\hbar/e)m_{well}(2\pi n_{well})^{1/2} \approx 0.4\mu$m at room temperature] and will therefore adversely affect the mobility, particularly at low temperature. Therefore, the large variation in the number of oriented abrupt steps between the $N = 1$ and $N > 1$ structures may account in part for the anomalously low mobility in the $N = 1$ sample at 77K. Further microscopy studies continue to test this conjecture and to optimize buffer layer design.

5.6 Conclusions

In InSb quantum wells with $Al_xIn_{1-x}Sb$ barrier layers δ-doped with Si, room temperature electron mobilities as high as 41,000cm^2/Vs, which is the highest reported value for a semiconductor quantum well, and 380,000cm^2/Vs at 6.5K were observed for electron concentrations of 2.4×10^{17}cm^{-3}. Even higher mobility should be possible with improved surface morphology and higher electron concentrations should result from decreasing the quantum well to dopant distance.

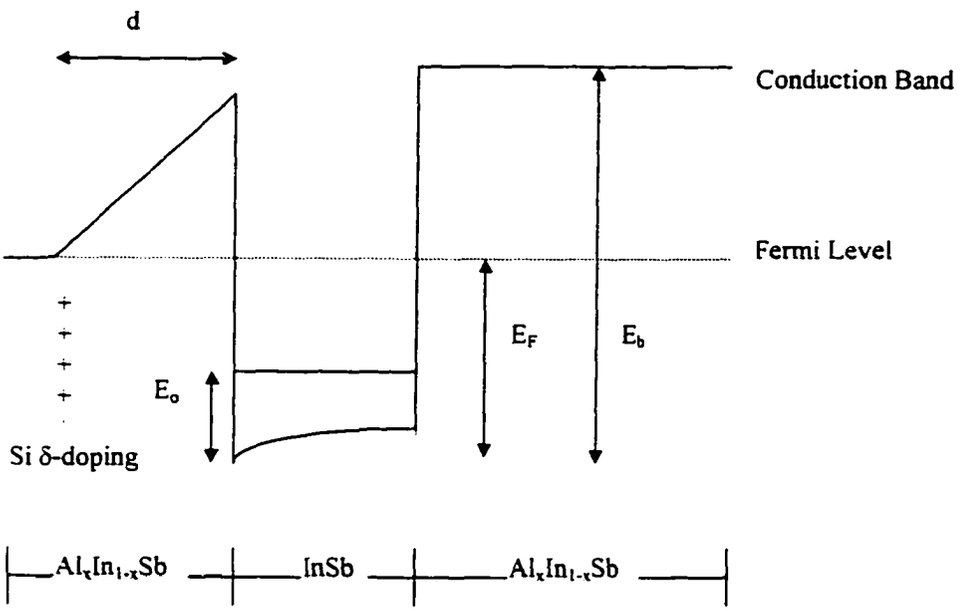

Figure 5.4: Schematic diagram showing parameters used in a simple model for the dependence of electron density on spacer layer thickness.

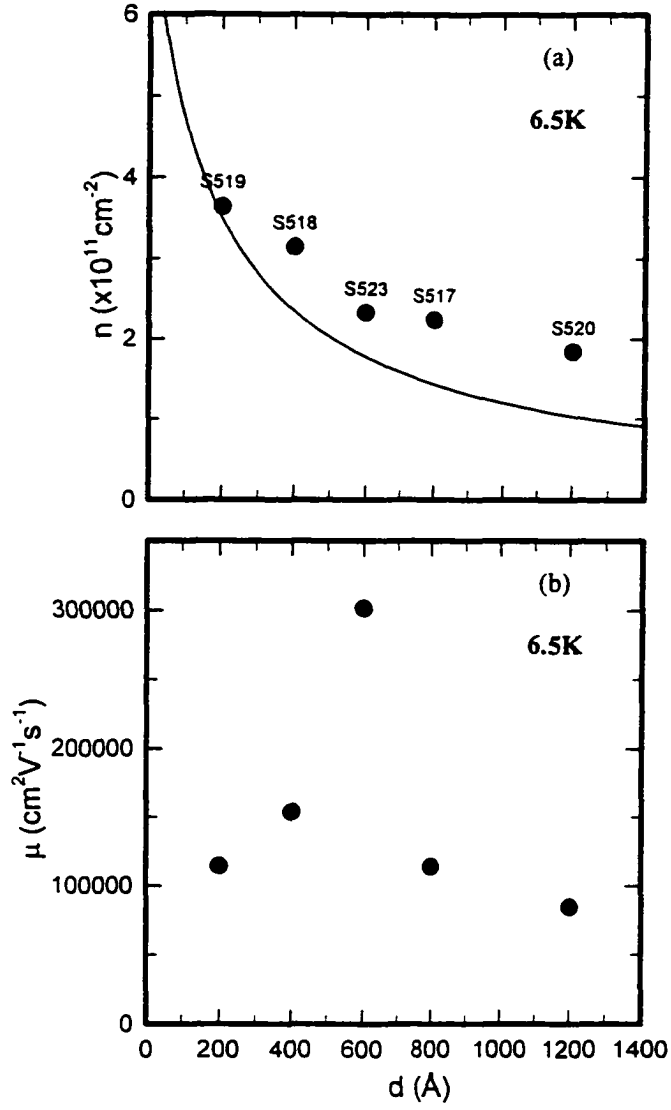

Figure 5.5: 6.5K (a) density and (b) mobility for our triple-doped single quantum wells. The line in (a) corresponds to a prediction based on a simple model assuming a non-parabolic dispersion relation and a 60% band offset.

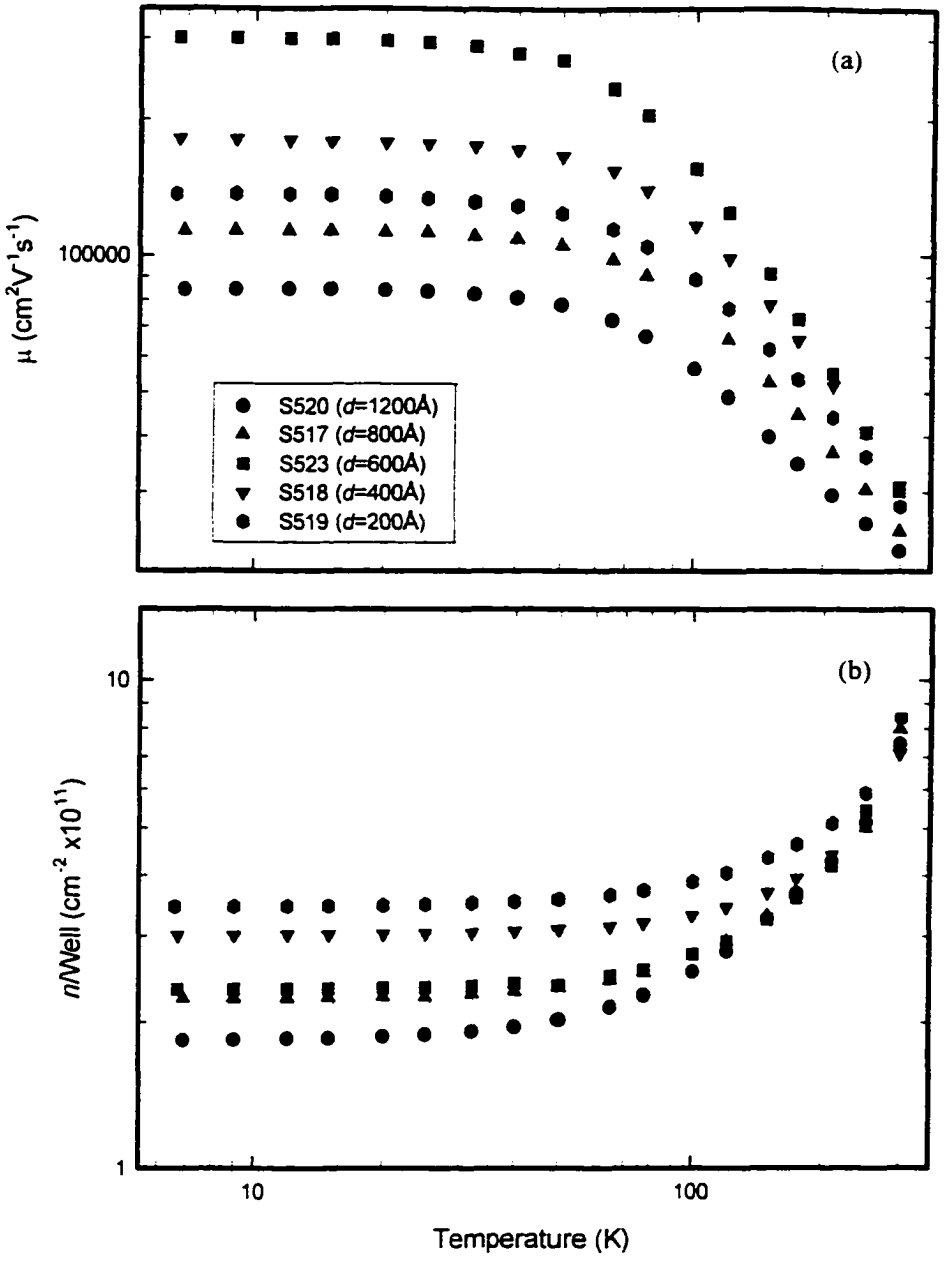

Figure 5.6: (a) Mobility and (b) density as a function of temperature for the triple doped single quantum wells.

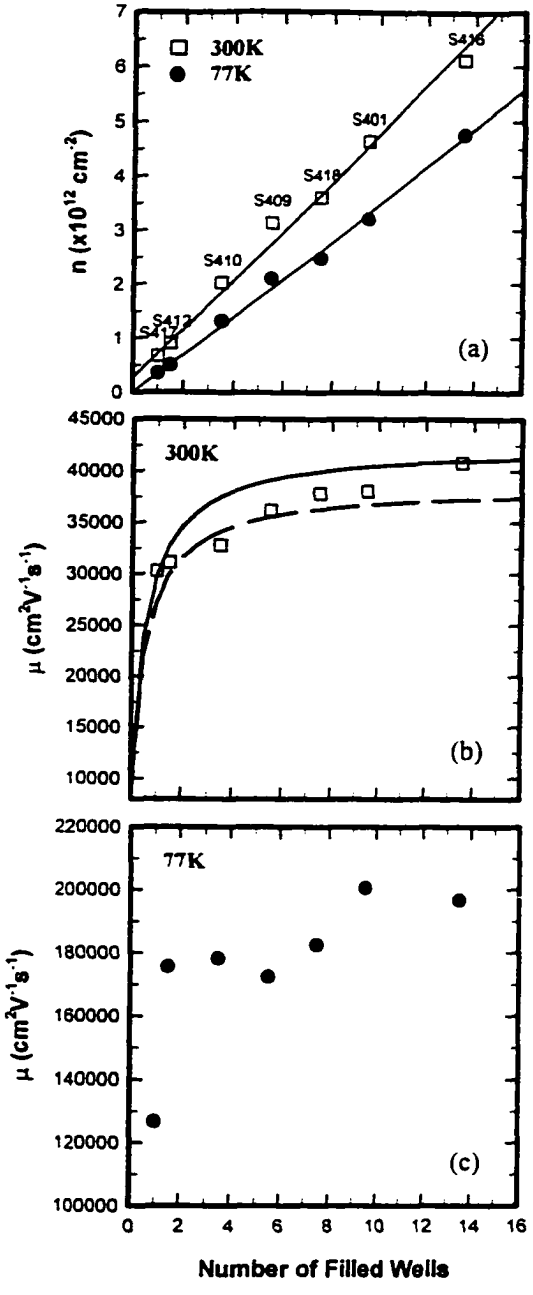

Figure 5.7: Measured electron (a) density at room temperature and 77K, (b) mobility at room temperature, and (c) mobility at 77K vs. number of filled wells. The solid lines in (a) are fits to the data with forced ordinate-axis intercepts. Lines in (b) are from a model where the only parameter is the mobility in the well. The solid and dashed lines correspond to well mobilities of 43,000cm^2/Vs and 39,000cm^2/Vs, respectively.

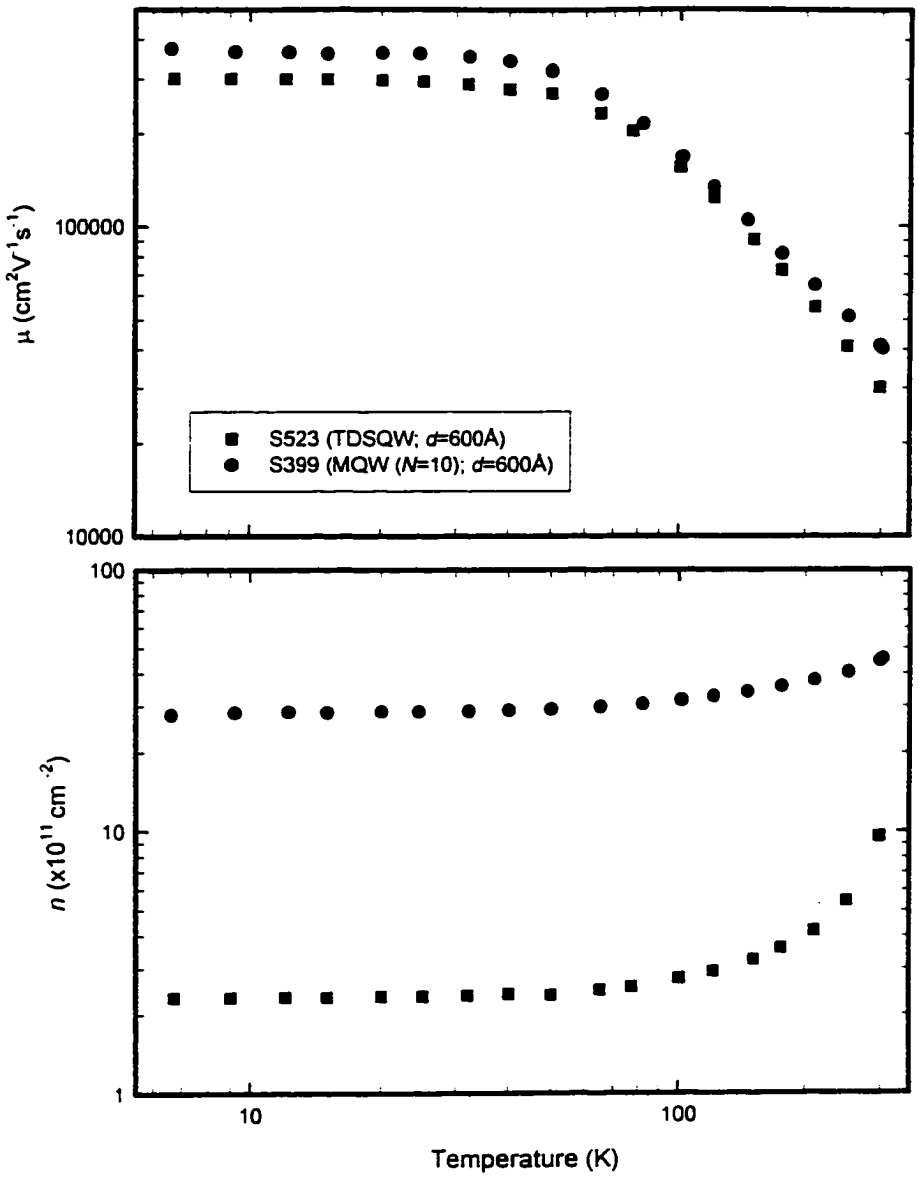

Figure 5.8: (a) Mobility and (b) density for a MQW (circles) and TDSQW (squares).

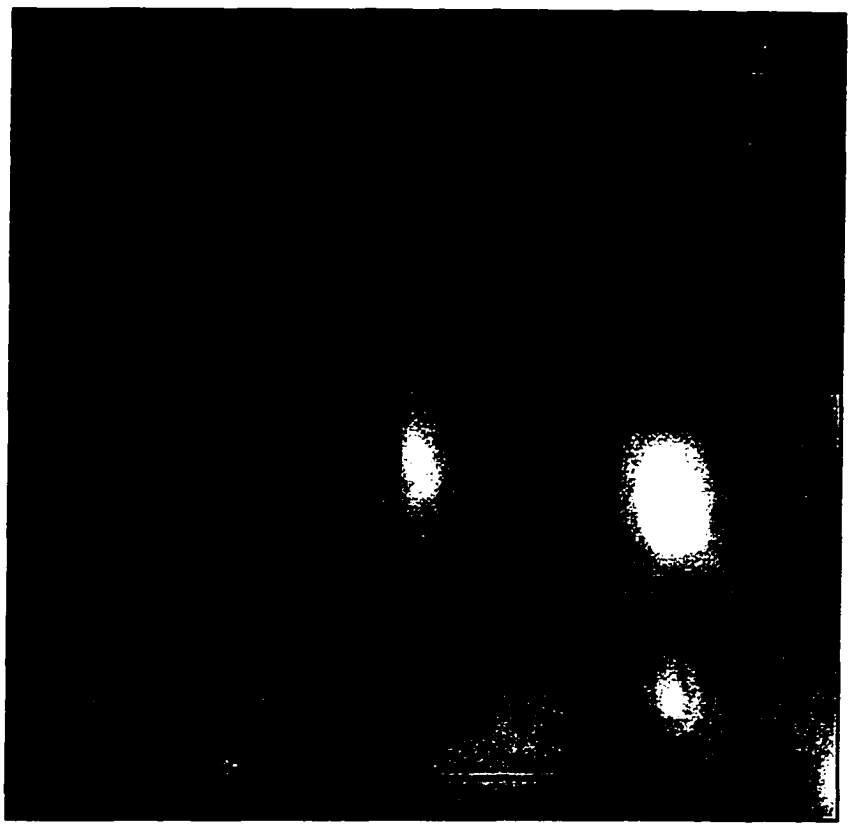

Figure 5.9: Noncontact atomic force microscope images of the surface of a single quantum well sample. The large image is a 50μm square region with the gray scale representing a height variation of 1000Å. The small image (inset) is a 2.6μm square region with the gray scale representing a height variation of 100Å, demonstrating the presence of screw dislocations. Steps of monolayer height can be seen.

Chapter 6

Optical and Transport Studies

The recent achievement of high quality quantum wells now allows for optical and low temperature experiments that can be used for the characterization of materials and to study unique features in the InSb/$Al_xIn_{1-x}Sb$ system. In this chapter, I present some initial results from ongoing Fourier Transform Infrared Spectrometry (FTIR) [88, 89] and low temperature magnetotransport experiments.

6.1 Fourier Transform Infrared Spectrometry

In the simple quantum well model presented in Section 5.4.1, a number of parameters were assumed, including the barrier height. This value is affected by the band offset, which is the percent of the bandgap difference appearing in the conduction band discontinuity at the well/barrier interface. Little research has been done on this topic in the InSb/$Al_xIn_{1-x}Sb$ system.

Fourier Transform Infrared Spectrometry (FTIR) can be used to measure the energy of electronic transitions from valance to conduction band states [88, 89]. Figure 6.1 shows transmission as a function of photon energy, $h\nu$, for a 25 period multiple quantum well sample[1]. We observe that the transmission decreases roughly

[1]The sample is as shown in Figure 5.1 for $N = 25$ except dopant layers (a), (b) and (c) and the 1000Å layer between dopant layers (a) and (b) are omitted, the well is 250Å wide, and the wells

in steps, which is expected from the 2-D density of states.

The peaks at the onset of each "step" are due to excitons. Linewidths of these peaks are a measure of crystalline and interface quality. Wider linewidths are observed when thinner buffer layers are used, indicating a structure of lower quality, as predicted in Chapter 5.

We can predict transition energies from the well width and barrier height, the latter of which is proportional to the band offset. The bandgap for quantum wells also differs from that of bulk InSb due, in part, to strain. The difference in energy between the conduction and light hole bands, E_+, and conduction band and heavy hole bands, E_-, is given by:

$$E_\pm = E_g + \left[\alpha\left(2 - 2\frac{C_{12}}{C_{11}}\right) \pm \beta\left(1 + 2\frac{C_{12}}{C_{11}}\right)\right]\varepsilon, \tag{6.1}$$

where α is the sum of the deformation potentials in the conduction and valance bands, C_{11} and C_{12} are elastic constants [62], and β is the shear deformation potential. ε is the strain, given by:

$$\varepsilon = \frac{a_{o,InSb} - a_{o,AlInSb}}{a_{o,AlInSb}}. \tag{6.2}$$

To model the transitions, a parameter, Q, is introduced, which is the percent of the smallest bandgap discontinuity (E_- in this case) appearing in the conduction band at the well/barrier interface. Also, a correction term of order ε^2 has been added to Equation 6.1, and the conduction and LH bands were calculated in the 2-band approximation (Sec. 1.3.3). Assuming $Q = 0.70$, Figure 6.1 shows the predicted transitions (arrows), which consist of three heavy-hole to conduction band (HHi-CBi) and one light-hole to conduction band (LHi-CBi). The selection rule $\Delta i = 0$, where

are separated by 500Å.

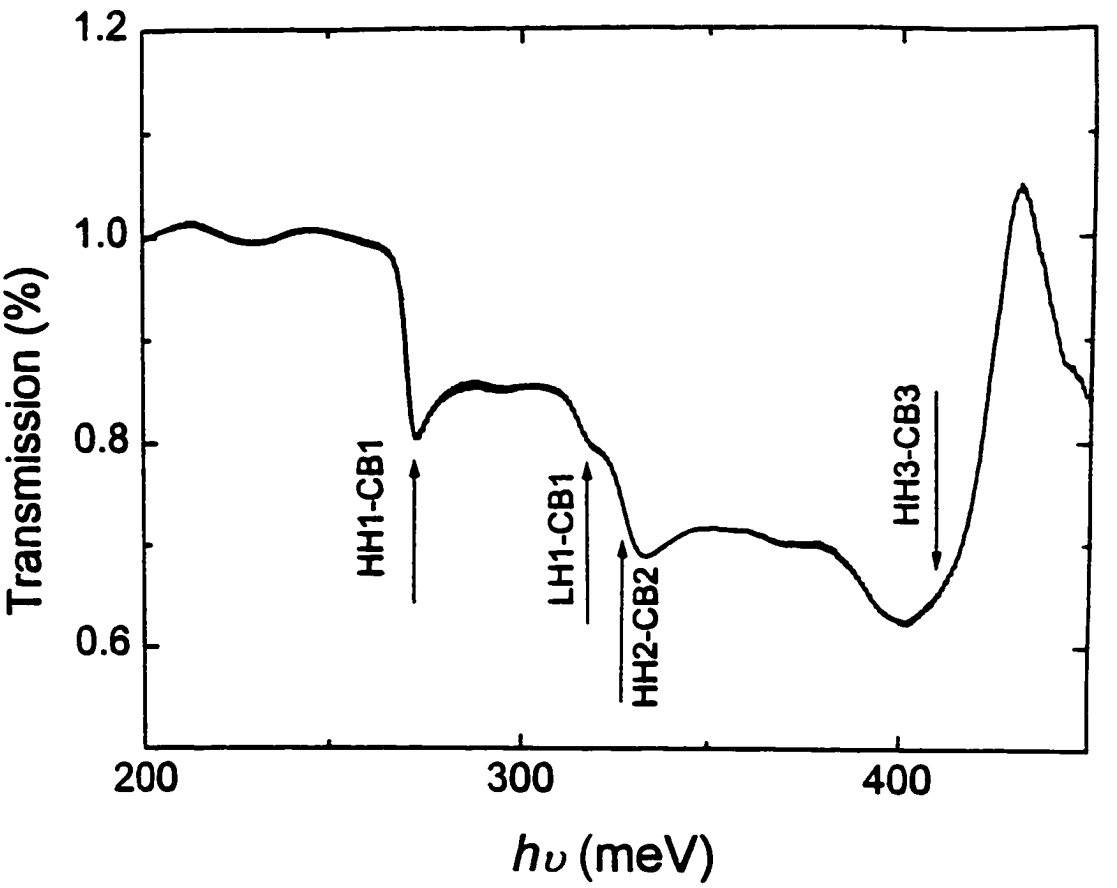

Figure 6.1: FTIR spectrum of an InSb multiple quantum well [88].

i is the subband index, has been implemented in the model. The close proximity of the predicted values to the peaks indicates that the correct transitions were modeled.

The model predicts that this quantum well system will become type-II if the band offset is greater than 0.77, which is therefore the upper limit predicted by this work. Preliminary work using the more detailed 4-band model suggests that the offset is actually less than 0.70, and may be as low as 0.55. A more precise number will be possible from the present study of parabolic wells, where all of the subband energies are sensitive to band offset (curvature), and $\Delta i = 2$ transitions are allowed in these structures, allowing for the observation of more transitions.

6.2 Integer Quantum Hall Effect (IQHE)

By extending the transport measurements to lower temperatures and higher magnetic fields, quantum mechanical effects can be probed in our quantum wells. In the quantum regime, the density of states becomes:

$$D^{2D}_{quantum} = \frac{eB}{hc}, \tag{6.3}$$

and the energies are given by:

$$E_j = \hbar\omega_c \left(j + \frac{1}{2}\right) \pm \frac{1}{2} g \mu_b B, \tag{6.4}$$

where $j = 0, 1, 2...$,

$$\mu_b = \frac{e\hbar}{2m^*} \tag{6.5}$$

is the Bohr magneton, and g is the *spin g factor*. The first term is due to the interaction of the moving electron charge and the second term is due to the interaction of the electron spin with the applied magnetic field.

Evidence for high quality two-dimensional structures can be obtained by the observation of the integer quantum Hall effect (IQHE). Recently, the IQHE has been

observed in a number of our quantum wells. Figure 6.2 shows data from a TDSQW, as shown in Figure 5.4.1 with d = 300Å and a well width of 300Å, at 1.4K and 33mK. Minima in resistivity are expected when an integer number of Landau levels are occupied since electrons in Landau levels completely below the Fermi energy have no nearby empty states in which to scatter. We begin to see these Shubnikov de-Haas (SdH) oscillations at B_{onset}=0.5T.[2] A measure of disorder can be deduced from B_{onset} since $\mu B > 1$ is required to see SdH oscillations; an electron must complete at least one orbit of the Fermi surface before scattering. Setting $\mu B_{onset} = 1$ provides a value for the "quantum mobility" of 20,000cm^2/Vs, which is about an order of magnitude smaller than the "transport mobility" discussed in Chapter 5. This is qualitatively expected since quantum mobility is sensitive to all scattering events, while transport mobility is sensitive predominantly to large angle scattering.

Landau level filling factors (number of filled Landau levels) are labeled in Figures 6.2 and 6.3. Spin splitting is not resolved until 0.92T (ν = 9), whereafter, plateaus in the Hall resistance are evident for $B > 1$. The precise quantization of these plateaus at h/ie^2, where i is an integer, is the signature of the IQHE. As shown in Figures 6.2 and 6.3, the IQHE is observed from ν = 8 (1.06T) to ν = 1 (8.48T). The explanation for the plateaus relies on the density of states being Gaussian Landau levels (as opposed to spikes in the case of a pure crystal) composed of extended states at the centers and localized states in the tails. A plateau occurs when the Fermi level lies in the localized states. The IQHE will be resolved when there is sufficiently little overlap between the center of a Landau level with the tails of neighboring Landau levels. Hence, for samples with less disorder, the IQHE will be observed down to lower B. The onset of the IQHE in our samples is similar to

[2]Since the position and number of minima are unchanged when the temperature is further lowered to 33mK, B_{onset} is not limited by temperature at 1.4K.

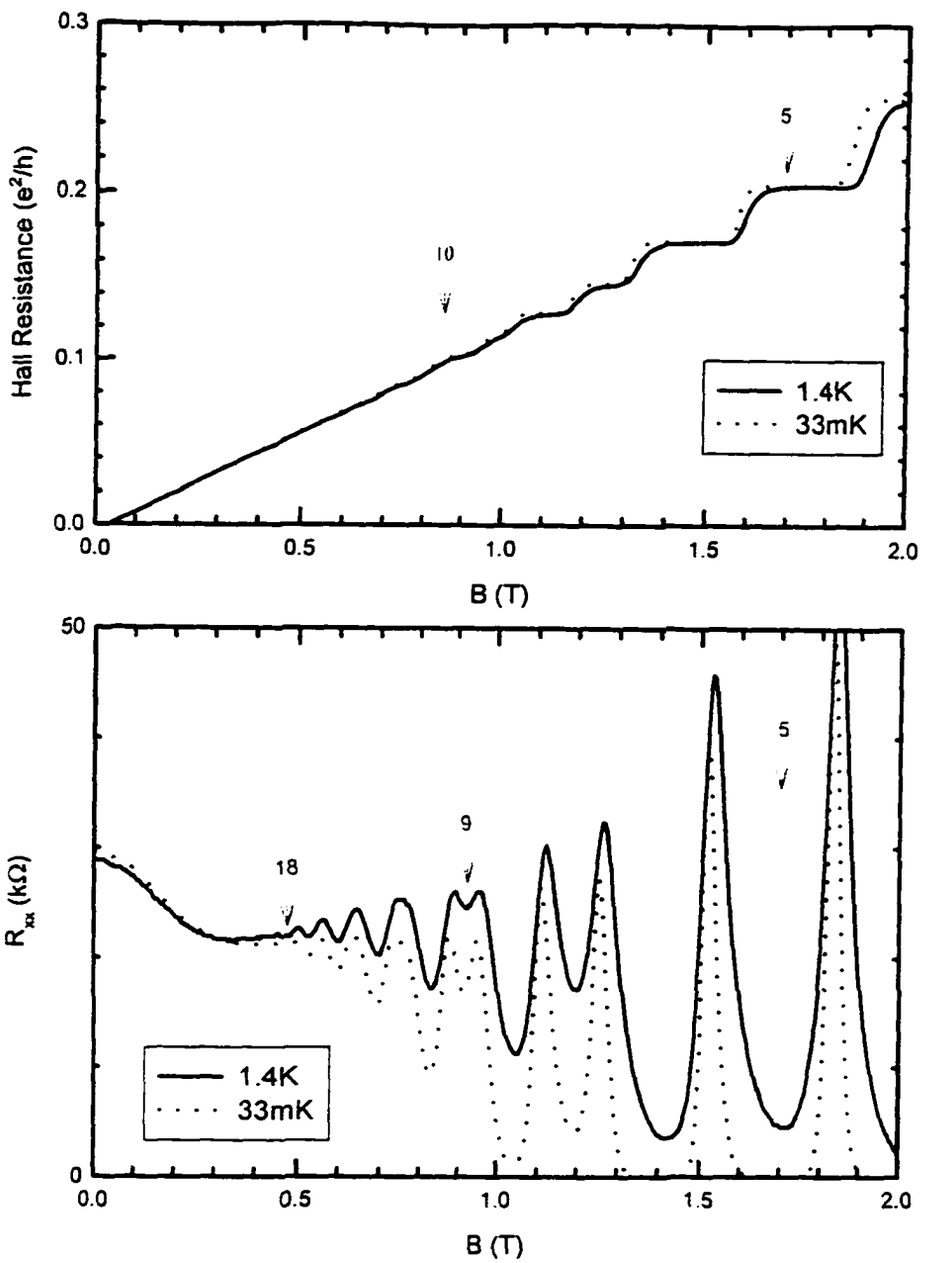

Figure 6.2: Low-B plot of the Hall resistance and resistivity as a function of B at 1.4K (solid) and 33mK (dotted) demonstrating the integer quantum Hall effect in an InSb quantum well with $Al_{0.09}In_{0.91}Sb$ barriers (S499). [Data taken at the NHMFL by J. Hicks, S.Q. Murphy, and M.B. Santos.]

that observed in InAs wells [110].

Since the discovery of the fractional quantum Hall effect (FQHE) in 1982, many studies have focused on the behavior of 2DEGs in the extreme quantum limit ($\nu < 1$). The experimental signature of the FQHE resembles that of the IQHE except that i is an odd denominator fraction rather than an integer. The explanation for the FQHE, however, is quite different. The FQHE is a manifestation of electron correlations. At odd denominator filling factors, the electrons condense into a quasi-particle liquid. This liquid state can be destroyed by weakening the importance of electron-electron interactions by, for example, increasing disorder.

As shown in Figure 6.3, S499 shows no evidence for the FQHE at $\nu = 2/3$. One possible explanation is that high disorder has destroyed the FQHE. However, it has been calculated [111] and observed [112][3] that 2DEGs in the extreme quantum limit ($\nu < 1$) should either exhibit the FQHE at $\nu = 2/3$ or, if the disorder is sufficiently high, enter an insulating phase. Measurements on S499 at 33mK reveal similar resistance values at $\nu < 1$, indicating that our 2DEG has not entered an insulating phase. The anomalous behavior of S499 suggests that destruction of the FQHE is not due solely to disorder. Because InSb has a small electron mass, parameters that predict the strength of electron correlation effects (effective Rydberg $\propto m/\epsilon^2$ and effective diluteness $\propto m/\epsilon$) are several times smaller than in GaAs or Si. Therefore, electron correlation effects are expected to be weaker in InSb than in other materials where the FQHE has been observed. More experiments are required to test whether disorder or an intrinsic property of InSb is responsible for our observations at $\nu < 1$. If the effects of disorder are sufficiently low, InSb quantum wells may provide a unique setting for studying single particle behavior in the extreme quantum limit.

[3] And references therein.

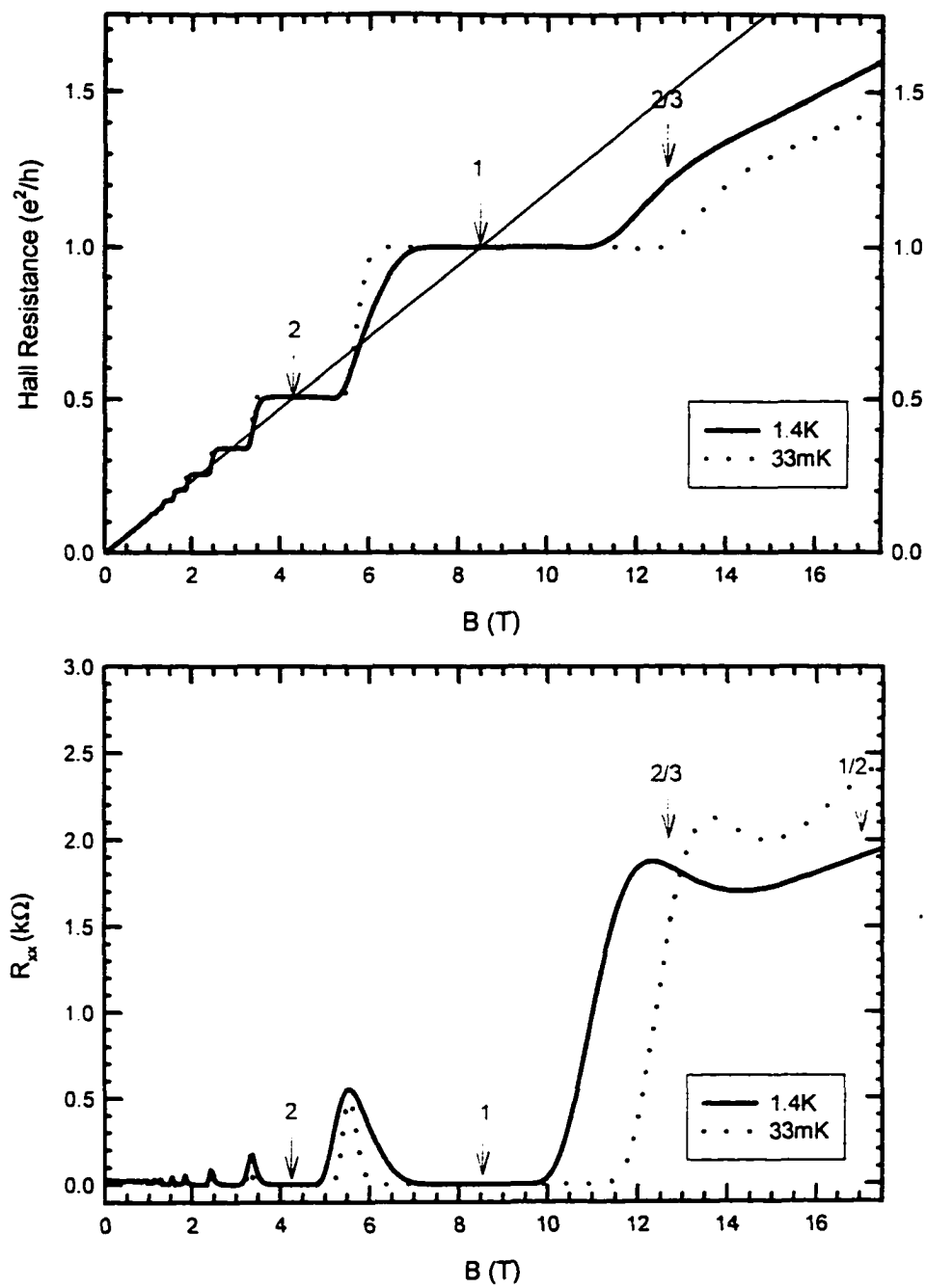

Figure 6.3: Plot of the Hall resistance and resistivity from Figure 6.2 as a function of B at 1.4K (solid) and 33mK (dotted) demonstrating the integer quantum Hall effect in an InSb quantum well with $Al_{0.09}In_{0.91}Sb$ barriers (S499). [Data taken at the NHMFL by J. Hicks, S.Q. Murphy, and M.B. Santos.]

Bibliography

[1] T. Ashley et al., Appl. Phys. Lett. **64**, 2433 (1994).

[2] T. Ashley et al., Appl. Phys. Lett. **70**, 931 (1997).

[3] R. A. Stradling, Semicond. Sci. Technol. **6**, C52 (1991).

[4] T. Ashley et al., Appl. Phys. Lett. **66**, 481 (1995).

[5] J. Heremans, D. L. Partin, C. M. Thrush, and L. Green. Semicond. Sci. Technol. **8**, S424 (1993).

[6] J. Heremans, Semicond. Sci. Technol. **8**, 1149 (1993).

[7] J. Heremans, Mat. Res. Soc. Symp. Proc. **475**, 63 (1997).

[8] J. Heremans et al., J. Appl. Phys. **74**, 1793 (1993).

[9] G. Williams, C. Whitehouse, N. G. Chew, G. W. Blackmore, and A. G. Cullis, J. Vac. Sci. Technol. **B3**, 704 (1985).

[10] T. D. Golding et al., Semicond. Sci. Technol. **5**, 311 (1990).

[11] M. K. Saker et al., Appl Phys. Lett. **65**, 1118 (1994).

[12] N. W. Ashcroft and N. D. Mermin, *Solid State Physics*, Saunders College, 1976.

[13] D. K. Schroder, editor, *Semiconductor Material and Device Characterization*. Wiley, 1976.

[14] L. J. van der Pauw, Philips Res. Rep. **13**, 1 (1958).

[15] D. K. de Vries and A. D. Wieck, Am. J. Phys. **63**, 12 (1995).

[16] J. R. Soderstrom, M. M. Cumming, J.-Y. Yao, and T. G. Anderson, Semicond. Sci. Technol. **7**, 337 (1992).

[17] W. I. Wang, E. E. Mendez, T. S. Kuan, and L. Esaki, Appl. Phys. Lett. **47**, 826 (1985).

[18] W. I. Wang et al., J. Appl. Phys. **60**, 1834 (1986).

[19] J. Heremans, D. L. Partin, D. T. Morelli, B. K. Fuller, and C. M. Thrush, Appl. Phys. Lett. **57**, 291 (1990).

[20] R. L. Petritz, Phys. Rev. **110**, 1254 (1958).

[21] J. R. Christman, *Fundamentals of Solid State Physics*, Wiley, 1988.

[22] C. Kittel, *Introduction to Solid State Physics*, Wiley, sixth edition, 1986.

[23] J. T. Verdeyen, *Laser Electronics*, Prentice-Hall, third edition, 1995.

[24] E. O. Kane, J. Phys. Chem. Solids **1**, 249 (1957).

[25] E. D. Haidemenakis, editor, *Optical Properties of Solids*, Gordon and Breach, 1980.

[26] J. Scriba et al., Solid State Commun. **86**, 633 (1993).

[27] M. A. Morrison, *Understanding Quantum Physics*, Prentice-Hall, 1990.

[28] T. Ando, A. B. Fowler, and F. Stern, Rev. Mod. Phys. **54**, 463 (1982).

[29] M. A. Herman and H. Sitter, *Molecular Beam Epitaxy*, Springer, 1996.

[30] E. H. C. Parker, editor, *The Technology and Physics of Molecular Beam Epitaxy*, Plenum, 1985.

[31] A. Cho, editor, *Molecular Beam Epitaxy*, Key Papers in Applied Physics, AIP Press, 1994.

[32] P. J. Dobson, B. A. Joyce, J. H. Neave, and J. Zhang, J. Cryst. Growth **81**, 1 (1987).

[33] A. G. de Oliveira, S. D. Parker, R. Droopad, and B. A. Joyce, Surf. Sci. **227**, 150 (1990).

[34] B. V. Shanabrook, J. R. Waterman, J. L. Davis, R. J. Wagner, and D. S. Katzer, J. Vac. Sci. Technol. **B11**, 994 (1993).

[35] C. F. McConville et al., Phys. Rev. **B50**, 14965 (1994).

[36] E. F. Schubert, *Doping in III-V Semiconductors*, Cambridge University Press, 1993.

[37] W. K. Liu and M. B. Santos, Surf. Sci. **319**, 172 (1994).

[38] J. F. O'Hanlon, *A User's Guide to Vacuum Technology*, Wiley, second edition, 1989.

[39] J. H. Neave and B. A. Joyce, Appl. Phys. **A31**, 1 (1983).

[40] Y. Rouillard, B. Lambert, Y. Toudic, M. Baudet, and M. Gauneau, J. Cryst. Growth **156**, 30 (1995).

[41] R. H. Miles et al., Appl. Phys. Lett. **6**, 1921 (1995).

[42] H. Remy, editor, *Treatise on Inorganic Chemistry*, volume 1, Elsevier, New York, 1956.

[43] W. K. Liu and M. B. Santos, J. Vac. Sci. Technol. **B14**, 647 (1996).

[44] J. W. Allen, Phil. Mag. **2**, 1475 (1957).

[45] W. K. Liu, W. T. Yuen, and R. A. Stradling, J. Vac. Sci. Technol. **B13**, 1539 (1995).

[46] F. D. Auret, J. Electrochem. Soc. **131**, 2115 (1984).

[47] R. P. Vasquez, F. F. Lewis, and F. J. Grunthaner, J. Appl. Phys. **54**, 1365 (1983).

[48] J. C. Bean, G. E. Becker, P. M. Petroff, and T. E. Seidel, J. Appl. Phys. **48**, 907 (1977).

[49] A. D. Johnson et al., "Low Temperature, Damage-Free Surface Cleaning of InSb(001) Prior to MBE Growth", in *Proc. 7th Int. Conf. Narrow Gap Semi., Santa Fe, New Mexico, 8-12 Jan. 1995*, edited by J. L. Reno, page 204. IOP, Bristol, 1995.

[50] K. J. Goldammer et al., Mat. Res. Soc. Symp. Proc. **450**, 97 (1997).

[51] P. F. Fewster, Semicond. Sci. Technol. **8**, 1915 (1993).

[52] P. F. Fewster and C. J. Curling, J. Appl. Phys. **62**, 4154 (1987).

[53] M. Schuster et al., J. Phys. D, Appl. Phys. (UK) **4A**, A206 (1995).

[54] L. Hart, P. F. Fewster, M. H. Ashwin, M. R. Fahy, and R. C. Newman, J. Phys. D, Appl. Phys. (UK) **4A**, A154 (1995).

[55] Buyer's Guide, Phys. Today **8**, BG11 (1997).

[56] C. G. Darwin, Phil. Mag. **27**, 315 (1914).

[57] P. P. Ewald, Ann. Physic **54**, 519 (1917).

[58] M. von Laue, Ergebnisse d. exakt. Natrurwiss. **10**, 133 (1931).

[59] W. J. Bartels, J. Vac. Sci. Technol. **B1**, 338 (1983).

[60] G. Bauer and W. Richter, editors, *Optical Characterization of Epitaxial Semiconductor Layers*, Springer, 1996.

[61] *PC-MRD User's Guide*, first edition, 1993, Published by Philips for use with version 1.0 of the PC-MRD Software.

[62] O. Madelung, editor, *Numerical Data and Functional Relationships in Science and Technology*, volume 17 of *Landolt-Börnstein*, Springer-Verlag, 1982.

[63] K. J. Goldammer et al., J. Vac. Sci. Technol **B16**, 1367 (1998).

[64] W. K. Liu, X. Zhang, W. Ma, J. Winesett, and M. B. Santos, J. Vac. Sci. Technol. **B14**, 2239 (1996).

[65] F. Stern, Appl. Phys. Lett. **43**, 974 (1983).

[66] E. F. Schubert, *Delta-Doping of Semiconductors*, Cambridge University Press, 1996.

[67] D. L. Partin, J. Heremans, and C. M. Thrush, J. Appl. Phys. **71**, 2328 (1992).

[68] L. R. Dawson, J. Cryst. Growth **98**, 220 (1989).

[69] J. Heremans, D. L. Partin, D. T. Morelli, and C. M. Thrush, J. Vac. Sci. Technol. **B10**, 659 (1992).

[70] D. L. Partin, J. Heremans, C. M. Thrush, and D. T. Morelli, J. Vac. Sci. Technol. **B10**, 873 (1992).

[71] S. Parker et al., Semicond. Sci. Technol. **4**, 663 (1989).

[72] R. Williams et al., Semicond. Sci. Technol. **5**, S338 (1990).

[73] M. Yang et al., J. Appl. Phys. **72**, 671 (1992).

[74] I. A. Panaev et al., Semicond. Sci. Technol. **11**, 1857 (1996).

[75] W. K. Liu, K. J. Goldammer, and M. B. Santos, J. Appl. Phys. **84**, 205 (1998).

[76] G. Williams, C. Whitehouse, A. Cullis, N. Chew, and G. Blackmore. Appl. Phys. Lett. **53**, 1847 (1988).

[77] K. Chen and J. Furdyna, J. Appl. Phys. **43**, 1825 (1972).

[78] C. E. C. Wood, Appl. Phys. Lett. **33**, 770 (1978).

[79] A. D. Johnson, Private Communication.

[80] R. Beall et al., *Gallium Arsenide and Related Compounds*, IOP Publishing Ltd., Bristol, 1988, edited by J. S. Harris.

[81] L. K. Li, Y. Hsu, and W. I. Wang, J. Vac. Sci. Technol. **B11**, 872 (1993).

[82] J. W. Matthews and A. E. Blakeslee, J. Vac. Sci. Technol. **14**, 989 (1977).

[83] M. A. Tischler, T. Katsuyama, M. A. El-Masry, and S. M. Bedair, Appl. Phys. Lett **46**, 294 (1985).

[84] J. W. Matthews and A. E. Blakeslee, J. Cryst. Growth **27**, 118 (1974).

[85] D. C. Houghton, D. D. Perovic, J.-M. Baribeau, and G. C. Weatherly, J. Appl. Phys. **67**, 1850 (1990).

[86] S. J. Barnett, C. F. McConville, R. H. Harrell, A. D. Pitt, and C. R. Whitehouse, "An Investigation of Structural Perfection and Lattice Relaxation in MBE Grown InSb/$In_{1-x}Al_xSb$ Strained Layer Structures", Unpublished (Pre-Print).

[87] C. R. Bolognesi, H. Kroemer, and J. H. English, J. Vac. Sci. Technol. **B10**. 877 (1992).

[88] N. Dai et al., Appl. Phys. Lett. **73**, 1101 (1998).

[89] N. Dai et al., "Determination of the Concentration and Temperature Dependence of the Fundamental Energy Gap in $Al_xIn_{1-x}Sb$", Appl. Phys. Lett., in press.

[90] G. A. Khodaparast, Private Communication.

[91] T. Ando, J. Phys. Soc. Japan **51**, 3900 (1982).

[92] T. J. Drummond et al., J. Appl. Phys. **52**, 5690 (1981).

[93] A. Gold, Phys. Rev. **B35**, 723 (1987).

[94] S. K. Paul and P. K. Basu, J. Appl. Phys. **10**, 3977 (1991).

[95] C. R. Bolognesi, H. Kroemer, and J. H. English, Appl. Phys. Lett. **61**. 214 (1992).

[96] V. Umansky, R. de-Picciotto, and M. Heiblum, Appl. Phys. Lett. **71**. 683 (1997).

[97] H. Sakaki, T. Noda, K. Hirakawa, M. Tanaka, and T. Matsusue, Appl. Phys. Lett **51**, 1934 (1987).

[98] T. Noda, M. Tanaka, and H. Sakaki, J. Cryst. Growth **111**, 348 (1991).

[99] D. J. Griffiths, *Introduction to Electrodynamics*, Prentice-Hall, second edition, 1989.

[100] A. Gold and V. T. Dolgopolov, Phys. Rev. **B33**, 1076 (1986).

[101] L. Pfeiffer, K. W. West, H. L. Stormer, and K. W. Baldwin, Appl. Phys. Lett. **55**, 1888 (1989).

[102] N. Kuze et al., J. Cryst. Growth **150**, 1307 (1995).

[103] P. Thompson et al., J. Appl. Phys. **69**, 7166 (1991).

[104] G. Singh et al., J. Vac. Sci. Technol. **B13**, 782 (1995).

[105] B. Brar and D. Leonard, Appl. Phys. Lett. **66**, 463 (1995).

[106] P. M. Thibado, B. R. Bennett, M. E. Twigg, B. V. Shanabrook, and L. J. Whitman, J. Vac. Sci. Technol. **A14**, 885 (1996).

[107] S. P. Watkins et al., Am. J. Phys. **63**, 12 (1995).

[108] C. C. Hsu, J. B. Xu, and I. H. Wilson, Appl. Phys. Lett. **65**, 1394 (1994).

[109] C. C. Hsu, Y. C. Lu, J. B. Xu, and I. H. Wilson, Appl. Phys. Lett. **64**, 1959 (1994).

[110] P. F. Hopkins, A. J. Rimberg, R. M. Westervelt, G. Tuttle, and H. Kroemer, Appl. Phys. Lett. **58**, 1428 (1991).

[111] S. Kivelson, D.-H. Lee, and S.-C. Zhang, Phys. Rev. **B46**, 2223 (1992).

[112] S. V. Kravchenko, W. Mason, J. E. Furneaux, and V. M. Pudalov, Phys. Rev. Lett. **75**, 910 (1995).

Appendix A

Contacts

Ohmic contact to our samples is obtained by the following procedure.

1. **Cleave from the sample a piece $\approx$ 5mm square.**

2. **With a clean razor blade, slice off a piece of relatively pure In.** We use 7N In.

3. **With a clean soldering iron, apply a small amount of In to the corners of the sample.** The contacts need to be small for the Van der Pauw technique to apply (Sec. 1.2.2).

4. **Anneal the sample at 230°C for five minutes in a reducing atmosphere of H_2 and N_2.** Since O_2 will combine with In to form an insulating oxide, we require H_2 to combine with existing O_2 to form water, which is innocuous. However, H_2 is extremely volatile, so the bulk of the reducing atmosphere is composed of inert N_2. We use a mixture of $\approx H_2(20\%)/N_2(80\%)$.

5. **Compress the annealed In with a clean piece of metal.**

6. **Press the 99.99% Au wire into the flattened In contact, and apply a small amount of In solder on top.**

7. **Again, compress the contact with a clean piece of metal.** We have found that the "compression" steps are necessary to consistently obtain Ohmic contact at low temperatures.

Appendix B

Pre-Growth Etch for GaAs Substrates

The following is the pre-growth etch procedure used for GaAs substrates, as discussed in Section 2.3.4. *Keep exposure to air at a minimum following the wet chemical etch to keep re-contamination of the substrate to a minimum.*

1. **Prepare Etchant**: H_2SO_4:H_2O_2:De-Ionized (DI) H_2O at 5:1:1
2. **Degrease**
   a) Boil in Trichloroethylene for 5 minutes
   b) Boil in Acetone for 5 minutes
   c) Boil in Methanol for 5 minutes
3. **Rinse** in DI H_2O for 2 minutes.
4. **Etch** for 2 minutes, keeping substrate in motion
5. **Rinse** in DI H_2O for 3 minutes
6. **Boil** in Methanol for 3 minutes
7. **Blow dry** with filtered N_2
8. **Load Substrates** quickly to reduce re-contamination

Appendix C

Modified CP4A Pre-Growth Etch for InSb Substrates

The following is a variation of the CP4A etchant [44] used for pre-growth etching of InSb substrates, and produces a mirror like surface with a passivated oxide layer that is low in carbon contaminants [45], as discussed in Section 2.3.5. *Keep exposure to air at a minimum following the wet chemical etch to keep re-contamination of the substrate to a minimum.*

1. **Prepare Etchant**: HNO_3:HF:CH_3COOH:De-Ionized (DI) H_2O at 2:1:1:10
2. **Degrease**
   a) Boil in Trichloroethylene for 5 minutes
   b) Boil in Acetone for 5 minutes
   c) Boil in Methanol for 5 minutes
3. **Etch** for 2 minutes, keeping substrate in motion
4. **Rinse** in DI H_2O for 3 minutes
5. **Boil** in Methanol for 3 minutes
6. **Blow dry** with filtered N_2
7. **Load Substrates** quickly to reduce re-contamination

Appendix D

Additional Delta Doped Sample Parameters and Additional Samples

The following table lists a number of extra parameters for the InSb and $Al_{0.09}In_{0.91}Sb$ δ-doped samples discussed in Chapter 4 as well as some additional samples not mentioned. All samples are δ-doped InSb, unless an "AlInSb" appears in the "comments" column. The notation is the same as that used in Chapter 4. The notation "Δ T+30/5" is interpreted as a 5 minute anneal occurring between doping and growth of the cap later at T_{tr} + 30°C. However, S338 had a post growth anneal performed for about 18.5 minutes.

sample	Tδ (°C)	Tcap (°C)	Si (°C/s)	Doping	nRT(cm-2)	μRT(cm2/Vs)	n77K(cm-2)	μ77K (cm2/Vs)	Comments
S311	Ttr	Ttr	1305/50	c(4x4)	9.00E+12	45174	3.03E+12	23234	**Growth Run 11**
S312	Ttr+20	Ttr+20	1305/50	'1x3'	6.80E+12	52920	7.90E+11	18639	
S313	Ttr+40	Ttr+40	1305/50	'1x3'	6.97E+12	52414	-1.65E+11	-206	
S314	Ttr-20	Ttr-20	1305/50	c(4x4)	1.04E+13	31849	4.32E+12	22075	N=957
S315	Ttr-40	Ttr-40	1305/50	c(4x4)	1.04E+13	42311	4.08E+12	25818	
S316	Ttr+10	Ttr+10	1305/50	'1x3'	9.03E+12	45696	2.23E+12	22567	
S317	Ttr+30	Ttr+30	1305/50	'1x3'	7.17E+12	51529	4.78E+11	17048	
S318	Ttr+35	Ttr+35	1305/50	'1x3'	7.25E+12	52279	7.32E+11	14625	
S319	Ttr-50	Ttr-50	1305/50	c(4x4)	1.12E+13	41502	4.08E+12	25424	
S320	Ttr-20	Ttr+30	1305/50	'1x3'	7.42E+12	51763	-1.68E+11	-164	
S321	Ttr+30	Ttr-20	1305/50	c(4x4)	8.78E+12	48679	3.01E+12	25728	
S322	Ttr+30	Ttr+30	1305/50	'1x3'	6.42E+12	53959	-1.94E+11	-1293	Δ Ttr+30/11
S323	Ttr+20	Ttr-20	1305/50	c(4x4)	9.38E+12	43613	3.26E+12	19815	
S327	Ttr-20	Ttr-20	1305/50	c(4x4)	8.26E+12	47913	2.46E+12	25779	Δ Ttr+20/5
S328	Ttr-20	Ttr-20	1305/10	c(4x4)	6.65E+12	53605	8.26E+11	39123	
S338	Ttr-20	Ttr-20	1305/50	c(4x4)	8.39E+12	47273	3.70E+12	26996	Δ Ttr+40/PG
S350	Ttr-20	Ttr-20	1305/50	c(8x2)/(4x2)	6.90E+12	46987	2.51E+12	22395	w/o Sb flux for δ
S374	Ttr-20	Ttr-20	1305/50	c(4x4)	6.85E+12	47463	2.95E+12	25652	
S434	Ttr-20	Ttr-20	1305/50	c(4x4)	8.67E+12	46765	3.13E+12	27262	**Growth Run 12**
S439	Ttr-20	Ttr-90	1305/50	c(4x4)	7.92E+12	49477	2.93E+12	30031	
S452	Ttr-20	Ttr-20	1305/50	c(4x4)	N/A	N/A	2.97E+12	27614	**Growth Run 13**
S453	Ttr+30	Ttr-20	1305/64	'1x3'	8.59E+12	49584	2.58E+12	25964	N=5
S455	Ttr+30	Ttr-20	1305/64	'1x3'	7.53E+12	49319	2.08E+12	23876	N=20
S457	Ttr+30	Ttr-20	1305/64	'1x3'	5.95E+12	57377	7.28E+12	3514	N=50
S463	Ttr+30	Ttr-20	1305/64	(4x2)/'1x3'	6.44E+12	54371	7.59E+12	1700	N=100
S464	Ttr+30	Ttr-20	1305/64	(4x2)	6.34E+12	54826	6.22E+12	13387	N=100
S480	Ttr+30	Ttr+30	1305/30	c(4x4)	N/A	N/A	1.67E+12	37138	tδ=30s
S484	Ttr+30	Ttr-20	1305/5	c(4x4)	N/A	N/A	1.71E+12	37333	tδ=5s
S485	Ttr-20	Ttr-20	1305/64	c(4x4)	7.81E+12	45965	3.12E+12	28871	GR = 1.6 ML/s
S487	Ttr-20	Ttr-20	1305/128	c(4x4)	1.21E+12	44610	7.71E+12	17463	tδ=128s
S497	Ttr-20	Ttr-20	1305/255	c(4x4)	8.61E+12	46505	4.10E+12	21832	tδ=255s
S331	Ttr-20	Ttr-20	1305/50	c(4x4)	4.70E+12	27246	3.60E+12	12561	**AlInSb**
S332	Ttr	Ttr	1305/50	c(4x4)/(1x3)	4.45E+12	29605	3.43E+12	11525	**AlInSb**
S333	Ttr+20	Ttr+20	1305/50	(1x3)	3.96E+12	31522	2.80E+12	10440	**AlInSb**
S334	Ttr+40	Ttr+40	1305/50	'1x3'	3.11E+12	33390	1.13E+12	4947	**AlInSb**
S336	Ttr+40	Ttr-20	1305/50	'1x3'	4.43E+12	32744	3.08E+12	12795	**AlInSb**

Table D.1: Additional δ-doped sample information.

IMAGE EVALUATION
TEST TARGET (QA-3)

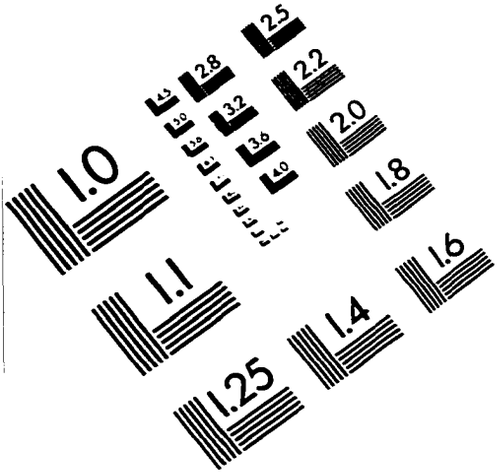

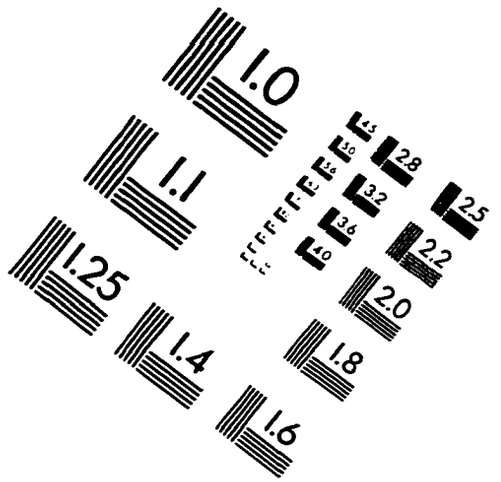

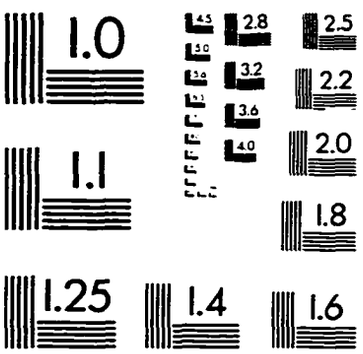

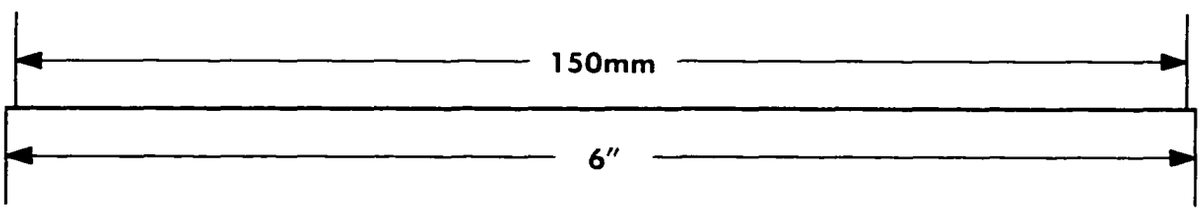

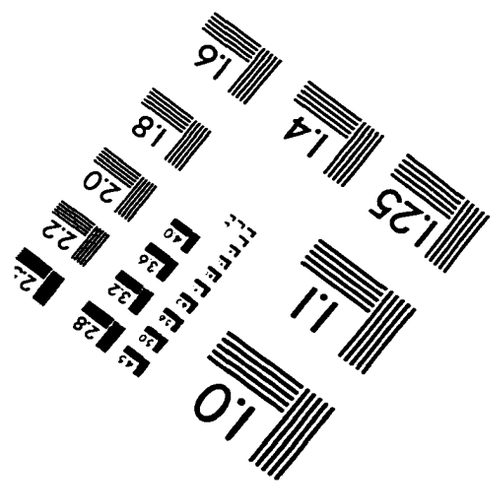

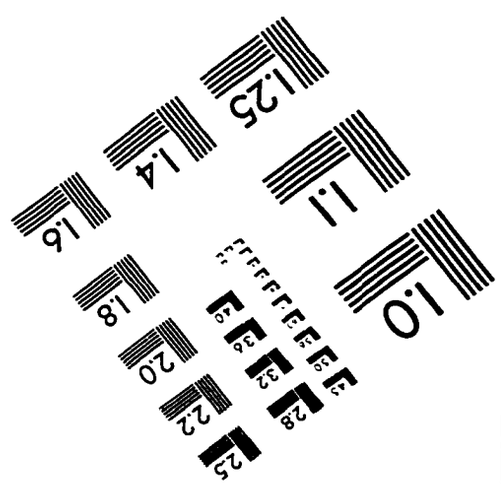

APPLIED IMAGE, Inc
1653 East Main Street
Rochester, NY 14609 USA
Phone: 716/482-0300
Fax: 716/288-5989